

# Microbiome association diversity reflects proximity to the edge of instability

Rubén Calvo,<sup>1,2</sup> Adrián Roig,<sup>1,2</sup> Roberto Corral López,<sup>1,2</sup> José Camacho-Mateu,<sup>3</sup> José A. Cuesta,<sup>4,5</sup> and Miguel A. Muñoz<sup>1,2,\*</sup>

<sup>1</sup>*Instituto Carlos I de Física Teórica y Computacional, Universidad de Granada, Granada, Spain*

<sup>2</sup>*Departamento de Electromagnetismo y Física de la Materia, Universidad de Granada, Granada, Spain*

<sup>3</sup>*Institute of Functional Biology & Genomics, CSIC - Universidad de Salamanca, Salamanca, Spain*

<sup>4</sup>*Universidad Carlos III de Madrid, Departamento de Matemáticas,*

*Grupo Interdisciplinar de Sistemas Complejos (GISC), Leganés, Spain*

<sup>5</sup>*Instituto de Biocomputación y Física de Sistemas Complejos (BIFI), Universidad de Zaragoza, Zaragoza, Spain*

(Dated: February 2, 2026)

Recent advances in metagenomics have revealed macroecological patterns or "laws" describing robust statistical regularities across microbial communities. Stochastic logistic models (SLMs), which treat species as independent—akin to ideal gases in physics—and incorporate environmental noise, reproduce many single-species patterns but cannot account for the pairwise covariation observed in microbiome data. Here we introduce an interacting stochastic logistic model (ISLM) that minimally extends the SLM by sampling an ensemble of random interaction networks chosen to preserve these single-species laws. Using dynamical mean-field theory, we map the model's phase diagram—stable, chaotic, and unbounded-growth regimes—where the transition from stable fixed-point to chaos is controlled by network sparsity and interaction heterogeneity via a May-like instability line. Going beyond mean-field theory to account for finite communities, we derive an estimator of an effective stability parameter that quantifies distance to the edge of instability and can be inferred from the width of the distribution of pairwise covariances in empirical species-abundance data. Applying this framework to synthetic data, environmental microbiomes, and human gut cohorts indicates that these communities tend to operate near the edge of instability. Moreover, gut communities from healthy individuals cluster closer to this edge and exhibit broader, more heterogeneous associations, whereas dysbiosis-associated states shift toward more stable regimes—enabling discrimination across conditions such as Crohn's disease, inflammatory bowel syndrome, and colorectal cancer. Together, our results connect macroecological laws, interaction-network ensembles, and May's stability theory, suggesting that complex communities may benefit from operating near a dynamical phase transition.

From the seventeenth to nineteenth centuries, cumulative work by physicists and chemists culminated in the ideal-gas law, capturing the universal behavior of dilute gases under simple conditions [1]. In the mid-nineteenth century, Maxwell, Boltzmann, and others provided a microscopic basis via kinetic theory: neglecting intermolecular forces, they derived macroscopic observables from microscopic dynamics, establishing the ideal-gas law. Later experiments showed that gases and liquids form a single continuum separated by a phase transition, revealing the limits of the non-interacting ideal-gas description. Van der Waals then introduced minimal corrections—effective cohesive attractions between particles and an impenetrable particle core—yielding an equation of state that accounts for different phases, phase coexistence, and criticality [2, 3]. An analogous progression is now emerging in ecology. High-throughput metagenomics have generated a wealth of data that has revealed robust macroecological regularities in the composition and variability of microbiomes across taxonomic scales [4–8]. In particular, Grilli [5] identified three empirical "laws" that appear universal across different microbiomes (Fig. 1B): (i) for each species, temporal abundance fluctuations follow a Gamma distribution (the abundance-fluctuation distribution, AFD); (ii) across species, mean abundances are log-normally distributed (the mean-abundance dis-

tribution, MAD); and (iii) abundance variance scales as a power of the mean (Taylor's law with exponent close to 2). These laws probe single-species statistics and thus do not address interspecific couplings. Theoretically, they are successfully captured by a stochastic logistic model (SLM)—the ecological analogue of an ideal gas (Fig. 1A)—that reproduces marginal abundance statistics in the absence of interactions.

Yet species abundances are not independent. A simple way to quantify interdependence, or "association," is through pairwise correlations (Fig. 1C): the relative abundance of a given species can be positively, negatively, or negligibly associated with that of another, reflecting shared external drivers, direct interactions, or both [9–12]. The width of the distribution of pairwise correlations (denoted  $\Delta$  in Fig. 1C) measures the heterogeneity of these associations, and in empirical microbiomes it is much broader than predicted for uncoupled species [5, 12, 13]. By construction, the SLM does not account for the breadth of correlations, as it ignores "ecological forces" or interactions that shape species associations. Thus, much as Van der Waals introduced minimal interaction terms to extend the ideal-gas law, ecology calls for an extension of the uncoupled SLM that preserves its success at the single-species level while explaining the emergence of rich correlation patterns across communi-

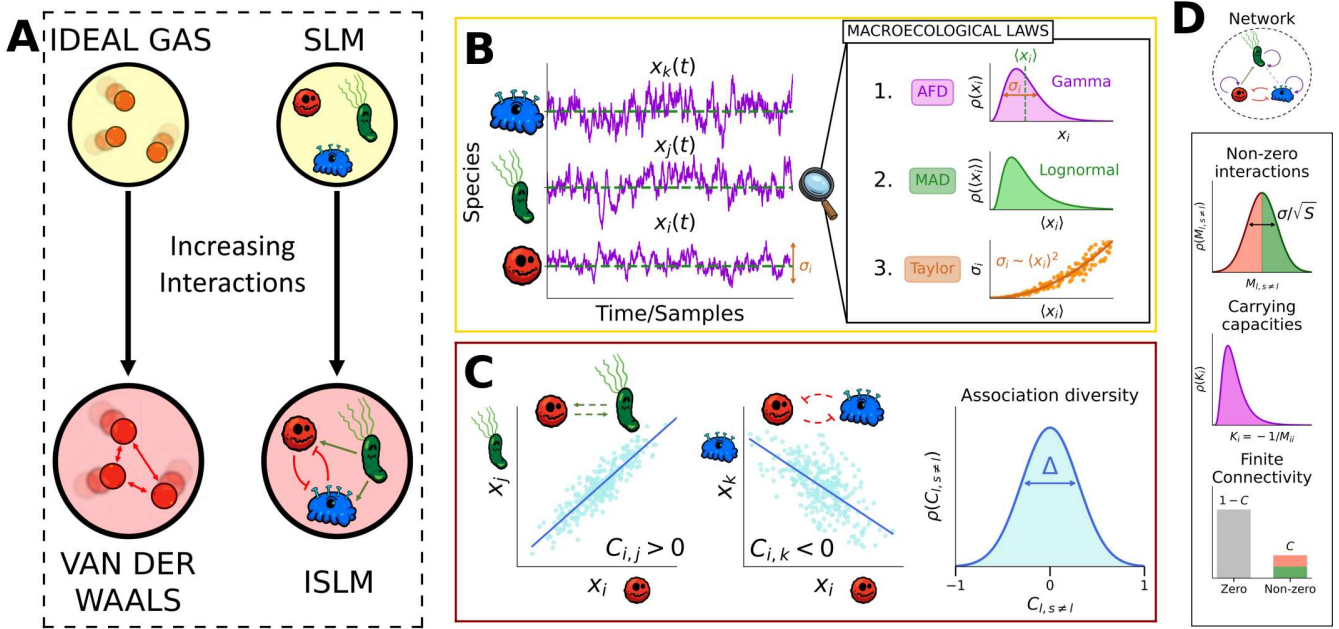


**Figure 1. From ideal-gas-like descriptions to interacting ensembles.** Non-interacting models such as the SLM capture marginal statistical patterns of empirical data (Grilli's laws) but fail to reproduce interspecific associations, while Bayesian inference can fit both at the cost of losing interpretability. **A.** Analogy between physics and ecology: the ideal gas corresponds to the uncoupled SLM, whereas the Van der Waals gas plays the role of the interacting SLM (ISLM) that explicitly includes interactions among species. **B.** Three macroecological laws observed in empirical microbiomes: (i) for each species, temporal abundances follow a Gamma distribution (abundance-fluctuation distribution, AFD); (ii) across species, mean abundances are approximately lognormally distributed (mean-abundance distribution, MAD); and (iii) variance scales as the square of the mean (Taylor's law with exponent  $\approx 2$ ). These patterns concern marginal statistics and ignore correlations between species' relative abundances. **C.** Pairwise associations: two species can be positively correlated ( $i$  and  $j$ ) or negatively correlated ( $i$  and  $k$ ). Empirical microbiomes display a broad histogram of pairwise correlations, whose width we denote by  $\Delta$ , much wider than predicted by uncoupled models. **D.** Statistics of the synthetic ISLM. First row: schematic visualization of the interaction network. Second row: histogram of the non-zero entries of  $G_{ij}$  (see Materials and Methods). Third row: distribution of carrying capacities, set as in (5). Fourth row: link sparsity; a fraction  $1 - C$  of links is zero, while a fraction  $C$  is non-zero.

ties [13–15].

From a broader perspective, recent work has sought to reconstruct the underlying networks of species interactions from time-series and cross-sectional microbiome data [9, 16–19]. However, such inverse problems are notoriously ill-posed: high-dimensional ecological models (such as the GLV) are over-parameterized, inference is strongly affected by noise and limited sampling, and even Bayesian approaches can yield broad posteriors compatible with quantitatively different interaction networks [12, 20–22]. These difficulties have motivated—following the strategy of statistical physics—a shift toward “ensemble descriptions” that focus on families of interaction networks able to reproduce empirically constrained macroecological patterns—such as diversity, abundance distributions, and correlation structures—rather than attempting to infer a unique, fully specified network of microscopic interactions and ascribe it a literal mechanistic meaning [14] (see also [23]). However, while this ensemble framework can successfully reproduce the richness of empirical associations [14], it often does so at the cost of interpretability: posteriors may concentrate

on networks that are hard to parse mechanistically, and inference may start from simple Gaussian-matrix perturbations of the SLM yet converge to highly non-Gaussian interaction structures, hampering further analyses and conceptual advances.

In parallel with this network-inference program, a complementary line of theoretical work on complex microbiomes focuses directly on mapping the possible collective dynamical regimes that may emerge from large random-interaction networks [24]. May's pioneering analysis of the stability of large, complex ecological communities [25] opened the door to a body of work showing that generic models with random, typically non-reciprocal interactions can exhibit both stable coexistence and regimes of persistent, intrinsically chaotic fluctuations, especially when spatial structure, migration, and resource dynamics are included [24, 26–35]. These regimes are separated by a sharp transition line—an “edge of instability” (or “edge of chaos”) [36]. By analogy with other biological and artificial information-processing systems [37–43], one might hypothesize that real microbiomes are naturally poised near this edge. If so, operating close to the transi-

tion could have important consequences for stability, resilience, and responses to perturbations [23, 35, 44, 45], a hypothesis that deserves deeper, systematic scrutiny.

In this work, we connect these two perspectives: ensemble-based inference and dynamical-phase structure. We adopt the ensemble framework [14, 21, 23] and ask which generic classes of random interaction networks are both compatible with observed macroecological patterns and sufficiently constrained to retain mechanistic interpretability while keeping analytical tractability. We show that empirical microbiome data can be reproduced by a minimal interacting-SLM built from Gaussian ensembles of random interactions. The only relevant parameter is the distance to instability,  $g = \sigma\sqrt{C}$ , which controls how broadly species covary (i.e., the spread of association strengths). Knowing  $g$  —and thus where a community sits in the phase diagram— directly constrains the implied interaction architecture, the dynamical phase consistent with the data, and the community’s proximity to a critical transition. As we show in what follows, in human gut microbiomes,  $g$  clearly discriminates healthy individuals —whose communities appear closer to instability, with wider associations— from patients with dysbiosis-associated conditions. Our results suggest that a minimal “Van der Waals-like” correction to the ecological ideal gas not only reproduces observed correlation patterns, but also yields a biologically interpretable order parameter that places real microbiomes in parameter space and quantifies the deterioration of ecosystem function as they move away from a “healthy” state toward a “diseased” one.

## MODEL BUILDING AND ANALYSES

We consider an interacting stochastic logistic model (ISLM), i.e. a generalized Lotka-Volterra (gLV) system with multiplicative environmental noise, representing species-dependent stochastic growth rates. The abundance of species  $i = 1, \dots, S$  evolves according to the (Itô) Langevin equation

$$\dot{x}_i(t) = \frac{x_i(t)}{\tau_i} \left[ 1 + \sum_{j=1}^S A_{ij} x_j(t) \right] + x_i(t) \xi_i(t), \quad (1)$$

where  $\tau_i$  sets the characteristic time scale of growth/decay of species  $i$ ,  $A_{ij}$  is the interaction matrix, where diagonal entries are the single-species carrying capacities in the absence of interactions, as in the SLM (see below), and  $\xi_i(t)$  is a stochastic term describing the effect of environmental fluctuations on species  $i$ . For most of our analysis, we assume temporally white and uncorrelated environmental noise,

$$\langle \xi_i(t) \xi_j(t') \rangle = \sigma_0^2 \delta(t - t') \delta_{ij}, \quad (2)$$

so that cross-species covariances are generated entirely by the interaction matrix  $A$ . Note that, more generally, one could consider a non-trivial correlation matrix  $W$  encoding shared responses to latent environmental drivers or fields. A structured  $W$  could by itself induce broad distributions of pairwise correlations, even in the absence of biotic interactions, and both  $A$  and  $W$  can in principle be derived from more mechanistic consumer-resource models [15]. Here we deliberately focus solely on biotic interactions and set  $W_{ij} = \delta_{ij}$ , as in previous work some of us found that heterogeneity in  $A$  shapes the correlation distribution more strongly than noise correlations [14]. Neglecting noise correlations is thus a modeling choice that yields a minimal proof-of-concept for interaction-driven associations.

We parameterize the interaction matrix as

$$A = D + \sigma M, \quad (3)$$

where  $D$  is a diagonal matrix corresponding to the uncoupled SLM part (self-regulation terms that fix the carrying capacities in the absence of interactions),  $M$  is a random matrix whose statistics will be chosen to match empirical patterns, and  $\sigma$  controls the magnitude of the perturbation away from the SLM. In this way, we interpolate between an “ideal-gas” limit of uncoupled species ( $\sigma = 0$ ) and an interacting regime ( $\sigma > 0$ ), analogous to a Van der Waals correction. Our goal is to understand how the statistics of  $A$  shape community-level dynamics.

*Balanced Gaussian interaction ensemble* To define the synthetic ISLM ensemble, we proceed in three steps (illustrated in Fig.1D).

First, we consider the uncoupled SLM ( $\sigma = 0$ ) and, for simplicity, assume identical time scales ( $\tau_i = \tau$  for all  $i$ ). The fixed-point solution of Eq. (1), denoted by  $\mathbf{x}^*$ , satisfies

$$A\mathbf{x}^* = D\mathbf{x}^* = -\mathbf{1}, \quad (4)$$

where  $\mathbf{1}$  is the all-ones vector (see SI Section 1). Feasibility requires  $x_i^* > 0$  for all  $i$ . Thus, in the uncoupled limit,  $D_{ii}x_i^* = -1$ , i.e.  $x_i^* = -1/D_{ii}$ . Following Grilli’s work [5], we impose that the fixed points (equivalently, the carrying capacities  $K_i = -1/D_{ii}$ ) are positive and log-normally distributed to match empirical distribution of mean abundances (MAD):

$$K_i = -\frac{1}{D_{ii}} \sim \text{LogNormal}(\mu_K, \sigma_K), \quad (5)$$

where  $\mu_K$  and  $\sigma_K$  are the mean and variance of the distribution.

Secondly, we introduce interactions as a perturbation of the uncoupled SLM by writing the interaction matrix as in (3). Rather than sampling  $M$  directly, we first construct an intermediate random matrix  $G$  with zero row sum and then define  $M$  from  $G$  and the fixed point  $x^*$ . Concretely, we draw a sparse Gaussian matrix  $G$

with connectivity  $C$  by setting a random fraction  $1 - C$  of the off-diagonal entries to zero and sampling the remaining ones as independent Gaussian variables with zero mean and variance  $\text{Var}(G_{ij}) = 1/S$  (see Methods and SI Section 3.B). The diagonal of  $G$  is set to zero, and for each row  $i$  we subtract the mean over the nonzero entries so that

$$\sum_{j=1}^S G_{ij} = 0 \quad \text{for all } i, \quad (6)$$

ensuring that the net interaction received by each species is centered. This row-balance condition corresponds to orthogonality with respect to the homogeneous vector,  $G\mathbf{1} = \mathbf{0}$ . We then define  $M = -GD$ . By construction,  $M$  has zero diagonal and, because of (4), satisfies

$$M\mathbf{x}^* = -GD\mathbf{x}^* = G\mathbf{1} = \mathbf{0}, \quad (7)$$

so the balance (row-orthogonality) condition holds and the fixed-point vector is left unchanged when interactions are turned on. The full interaction matrix is then

$$A = D + \sigma M = D - \sigma GD, \quad (8)$$

which automatically ensures  $A\mathbf{x}^* = -\mathbf{1}$  for any  $\sigma$ .

This procedure generates an ensemble of sparse, balanced, random interaction matrices with log-normally distributed mean abundances and single-species statistics unchanged, while allowing us to tune the typical number of associations per species via the connectance  $C$  and the overall interaction heterogeneity via  $\sigma$  to match empirical correlation patterns.

In what follows, using techniques from the physics of disordered systems and random matrix theory, as well as computational analyses, we characterize the phase diagram of the ISLM and show that the connectivity, diversity, and strength of interactions play a crucial role in shaping the dynamics and stability of *in silico* ecological communities.

## RESULTS

*Random-matrix stability analysis.* Because the ISLM involves a large number of coupled degrees of freedom, stability is controlled by collective properties of the interaction matrix rather than by any single entry. Random matrix theory provides a natural framework to quantify these collective effects: in particular, it predicts the typical location and spread of the eigenvalue spectrum for large disordered networks, and thus yields analytic criteria for when fixed-point solutions lose stability as interaction strength and heterogeneity are increased.

More specifically, dividing (1) by  $x_i(t)$  and linearizing around  $\mathbf{x}^*$  yields a multivariate Ornstein–Uhlenbeck process with an effective matrix  $A_{\text{eff}}$  given by (see Methods

and SI–Section 1.B for details)

$$\tau A_{\text{eff}} = -AD^{-1} = -I - \sigma MD^{-1} = -I + \sigma G. \quad (9)$$

Importantly, as noted in the previous section, the balance condition implies  $G\mathbf{1} = \mathbf{0}$ , so  $\mathbf{1}$  is an eigenvector with eigenvalue 0. Since this is a rank-one constraint, it pins just one eigenvalue and does not affect the bulk spectrum as  $S \rightarrow \infty$ . In that limit, the eigenvalues of  $G$  follow the circular law [46–48], forming (to leading order) a disk of radius  $\sqrt{C}$  in the complex plane, so the spectrum of  $\tau A_{\text{eff}} = -I + \sigma G$  is the same disk rescaled by  $\sigma$  and shifted to be centered at  $-1$ . Linear stability is lost when the disk first reaches the origin, i.e. when  $g \equiv \sigma\sqrt{C} = 1$ , which is the classic May criterion for random ecosystems (see SI–Section 1.D). As a particular example, Fig. 3 panels A.1–A.3 show the spectral density of matrix  $G$ , confined to a disk whose radius increases with  $\sigma$ . In this particular case, since  $C = 1/2$ , the instability threshold occurs at  $\sigma = 1/\sqrt{2}$ .

*Dynamical mean-field theory approach* In order to go beyond linear stability analysis, we carried out a dynamical mean-field theory (DMFT) analysis of the ISLM. As previously discussed, this extends the standard generalized Lotka–Volterra framework by incorporating three key ingredients: a balanced, random ensemble of interactions, log-normally distributed diagonal elements, and multiplicative environmental noise. In the thermodynamic limit  $S \rightarrow \infty$ , DMFT becomes exact, reducing the full  $S$ -dimensional stochastic dynamics to an effective one-dimensional process for a single “representative” species with abundance  $x(t)$  [36, 49]. As derived in the SI, the effective equation is (SI, Eq. (131))

$$\dot{x}(t) = x(t)[1 - x(t) + \eta(t) + \xi(t)], \quad (10)$$

where  $\xi(t)$  is the original multiplicative environmental noise and  $\eta(t)$  is an emergent effective Gaussian noise generated by the random interactions with the rest of the network. The statistics of  $\eta(t)$  are fixed by the DMFT self-consistency condition, which relates its covariance to the autocorrelation of the effective trajectory (see SI–Section 3)

$$\langle \eta(t)\eta(t') \rangle = \sigma^2 \left( \langle x(t)x(t') \rangle - \langle x(t) \rangle \langle x(t') \rangle \right), \quad (11)$$

so that interaction-induced fluctuations feedback onto the dynamics of the focal species.

As in generalized Lotka–Volterra models [24, 26, 27, 36, 50], the effective process displays distinct dynamical phases as parameters vary: a stable fixed-point regime with finite stationary abundances, a chaotic regime with persistent irregular fluctuations that can drive extinctions, and an unstable regime with diverging populations (see SI–Section 3).

Because in our case environmental fluctuations enter multiplicatively, the term “fixed point” must be under-

stood in a statistical sense: in this phase the noise-averaged abundance (and the full stationary distribution) is time-independent, but individual trajectories still wander stochastically according to the stochastic logistic model (SLM). By contrast, in the chaotic phase even the noise-averaged abundance exhibits irregular temporal dynamics, and chaos must be characterized at the level of these underlying mean trajectories, on top of which environmental noise adds an additional layer of randomness (see SI-Section 5).

Quite remarkably—as we show analytically in SI Section 3.D/E—the orthogonality constraint forces a self-consistent cancellation of interaction-generated noise across the entire stable fixed-point phase. This implies that, for the balanced random ensemble, the noise term vanishes in the large-community limit,  $\eta(t) \equiv 0$  as  $S \rightarrow \infty$ . The effective dynamics therefore reduce *exactly* to a stochastic logistic equation driven only by multiplicative environmental noise, recovering the single-species SLM previously used to explain universal “macroecological laws” [5]. In this way, we provide a microscopic, analytically controlled derivation of Grilli’s one-species description from a high-dimensional interacting community with log-normal carrying capacities and balanced interactions—one of the central results of this work.

*Computational validation of dynamical phases and chaos* Before proceeding, we test the dynamical phases predicted by DMFT by simulating finite communities with interactions drawn from our synthetic ensemble and estimating the largest Lyapunov exponent (LLE), whose positivity is the standard hallmark of chaos. We simulate a community with  $S = 1000$  species up to  $t_{\max} = 10^2$  (time step  $h = 0.01$ ), for varying interaction widths and connectivities. The phase diagram in Fig. 2A reveals the same three regimes. For small interaction heterogeneity  $\sigma$ , the LLE is negative across the  $(C, \sigma)$  plane and trajectories relax to a unique fixed point (region FP), consistent with the stable DMFT solution. Beyond the fixed-point solution limit of instability  $\sigma = 1/\sqrt{C}$  (white curve), a thin band with positive LLE appears (region C), marking the onset of chaotic dynamics. Owing to finite size and finite observation time, this chaotic band is slightly shifted inward and narrower than the DMFT prediction; in the large- $S$  limit we expect the boundaries to coincide (see Figure S3 included in the SI). As  $\sigma$  increases further (keeping  $C$  fixed), trajectories cross a second boundary (dashed line) beyond which they diverge and leave the biologically realistic domain, corresponding to the unbounded phase U in DMFT. The time series in Fig. 2B–D illustrate these behaviors at fixed connectivity  $C = 0.85$ : below the stability line, all species relax to stationary abundances (FP, panel D); in the intermediate band, abundances show bounded irregular fluctuations with positive LLE (chaotic phase C, panel C); and for larger  $\sigma$ , trajectories blow up in finite time (unbounded phase U, panel B). Together, these simulations provide a

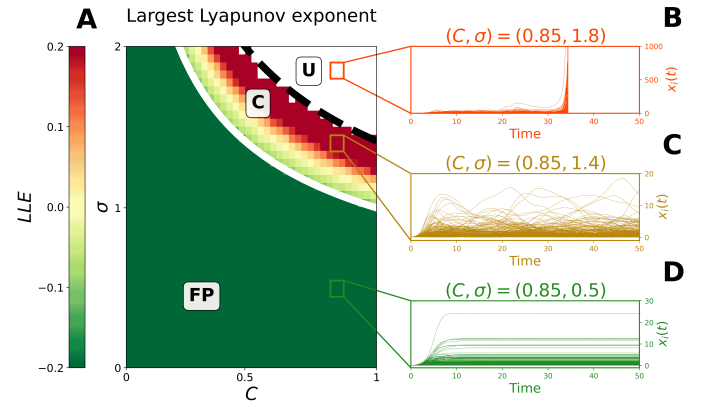


**Figure 2. The synthetic model exhibits fixed-point, chaotic, and unbounded dynamical phases.** **A.** Heat map of the largest Lyapunov exponent (LLE) as a function of  $\sigma$  and  $C$  (negative values are plotted as zero for clarity). Three regimes can be distinguished: a fixed-point phase (FP), a chaotic phase (C), and an unbounded phase (U) in which trajectories blow up. The white solid line and the black dashed line delimit the FP–C and C–U boundaries, respectively. Simulations were performed for communities with  $S = 10^3$  species (to suppress finite-size effects), without environmental noise ( $\sigma_0 = 0$ , the effect of noise is further explored in the SI-Section 5.B), and averaged over  $M = 50$  independent realizations of the quenched interactions. **B–D.** Representative time series illustrating the dynamical behavior in each regime shown in panel A.

direct dynamical confirmation of the fixed-point, chaotic, and unbounded regimes predicted by DMFT.

*Computational verification of macroecological laws in the synthetic ISLM model* Having characterized the dynamical phases of the ISLM in the infinite-size (mean-field) limit, we next use simulations to test whether the macroecological laws of [5] are preserved when interactions are turned on in finite communities.

Because of the constraint in (4), the perturbation  $M$  leaves the fixed points unchanged, so the MAD is satisfied by construction (see Figure 3 panels C.1–C.3). The remaining macroecological laws are likewise robust, as shown in the other panels of Fig. 3. We simulate a community with  $S = 100$  species up to  $t_{\max} = 10^2$  (time step  $h = 0.01$ ), collecting  $M = 10^3$  independent measurements, for three interaction strengths  $\sigma$  ( $\sigma = 0$  in the first row,  $\sigma = 1/\sqrt{8}$  in the second, and  $\sigma = 1/\sqrt{2}$  in the third) at fixed connectivity  $C = 0.5$ . Remarkably, approaching this edge leaves the AFD and MAD essentially unchanged and preserves Taylor’s law on average—the points scatter around the ideal straight line, as in real microbiome data (see e.g. [23, 51] and Panels B, C, and D)—while association diversity is strongly enhanced (Panels E.1–E.3). Near the instability, a wide range of correlation-histogram shapes emerges across network realizations (E.3), indicating many distinct coupling patterns that reproduce the same single-species laws yet dif-

fer markedly in interspecific structure.

*Beyond mean-field theory: from model to data* As already discussed, DMFT is exact in the infinite-community limit  $S \rightarrow \infty$ , where it reduces the full interacting dynamics to an effective single-species process. In this limit, pairwise covariances—and thus inter-species correlations—vanish by self-averaging over many interaction partners. Empirical microbiome data from diverse environments, however, exhibit nontrivial pairwise associations, so reproducing their distribution requires going beyond mean field. For large but finite communities, we capture these residual covariances by including the leading  $1/S$  finite-size corrections around the DMFT solution; we develop this beyond-DMFT framework below (see Materials and Methods and SI Section 4). [52]

This divergence can be exploited to construct a practical estimator of an effective stability parameter  $g$ , directly linking it to simple observables such as the empirical covariance distribution and the community size  $S$ . Here we extend this framework to the ISLM ensemble and, because microbiome time series are typically short, adapt it to use short-time covariances [53] rather than asymptotic long-time ones (see SI Section 4.L for details).

This yields an explicit expression relating the normalized width of covariances,  $\Delta$ , to the stability parameter  $g$  (with the edge of instability for the fixed-point solution at  $g = 1$ ) thereby allowing us to place actual microbiome data in the phase diagram. The implicit expression, derived in detail in the SI, reads:

$$S\Delta^2 = \frac{1}{8} \left( -6 - \frac{2}{\lambda} + \sqrt{\lambda} + \frac{4}{\sqrt{\lambda}} + \frac{3}{\lambda^{3/2}} \right), \quad (12)$$

where  $S$  is the number of species,  $\lambda = 1 - g^2$  and  $\Delta$  is the normalized width of covariances:

$$\Delta^2 = \frac{1}{S} \frac{\sum_{i,j \neq i}^S C_{ij}^2}{\left( \sum_i^S C_{ii} \right)^2}, \quad (13)$$

where  $C_{ij}$  denotes the short-time covariance matrix estimated from empirical data.

*Fitting empirical biome association patterns at the edge of instability* We now use our estimator (12) to infer an effective stability parameter  $g$  from empirical correlation patterns and the community size. In the model, the edge of instability corresponds to  $g = \sigma\sqrt{C} = 1$ . An inferred value of  $g$  therefore does not pin down a unique point in the  $(C, \sigma)$  plane, but rather a one-dimensional manifold defined by  $g = \sigma\sqrt{C}$ . This degeneracy reflects that, aside from finite-size effects, the correlation width is controlled only by the total interaction disorder, which depends on  $\sigma$  and  $C$  through their combination  $\sigma\sqrt{C}$ . Consequently, one parameter (e.g.,  $C$ ) can be chosen freely; given  $C$  and the inferred  $g$ , one then fixes  $\sigma = g/\sqrt{C}$  and samples many realizations of the ISLM interaction network at these values.

For each realization, we set  $S$  equal to the empirical number of species, draw an interaction network from the balanced ensemble, simulate the dynamics, and compute the resulting covariance (association) histogram. We then retain those networks whose association statistics best match the empirical distribution. This two-step procedure explicitly acknowledges that associations are non-universal and realization-dependent in finite networks, and uses them to select representative networks within an ensemble that already captures the robust one-point statistics.

Applying this inference scheme first to synthetic data generated with the ISLM model, we verified that the estimator behaves as expected: the inferred stability parameter  $g(C, \sigma)$  closely follows the theoretical prediction and increases towards 1 as  $(C, \sigma)$  approaches the DMFT stability boundary  $\sigma = 1/\sqrt{C}$  (Fig. 4A, colormap and black line). We then applied the same procedure to empirical time series from seawater, river, glacier, and lake microbiomes (see Methods). Their distance to the edge of instability was quantified and found to lie in the range  $g \in [0.93, 0.97]$  (icons and labels in Fig. 4B–E). Thus, all analyzed communities appear to operate very close to the edge of instability, with systematic but modest biome-to-biome variation. Part of this variation is captured by differences in the inferred stability parameter  $g$ : consistent with the beyond-mean-field theory, biomes with larger  $g$  (such as glacier microbiomes) display broader empirical correlation histograms (Fig. 4D), reflecting increased association heterogeneity, whereas those with slightly smaller  $g$  have narrower distributions (Fig. 4B,C,E). In addition, the theory predicts that, even at fixed  $g$ , the detailed shape of the correlation histogram depends on the specific realization of the interaction and noise networks. Consequently, variability across biomes reflects both genuine differences in  $g$  and sample-to-sample fluctuations arising from network-realization.

*Dysbiosis is linked to a retreat from the edge of instability* Our analysis of environmental communities suggests that microbiomes often operate near the edge of instability, a regime frequently associated with enhanced responsiveness, adaptability, and resilience in complex systems [37, 38]. The human gut microbiome is a particularly relevant case because it plays a central role in host health [54–56]. Dysbiosis—a persistent departure from a healthy microbial state, often accompanied by loss of key taxa and functions—has been linked to a wide range of diseases [35, 56–62].

Despite its clinical relevance, the ecological mechanisms underlying the transition from healthy to dysbiotic states remain unclear, limiting mechanistically grounded interventions [63, 64]. While recent work has argued that dysbiosis reflects a shift in the global balance of interactions toward more positive coupling [35], such claims typically rely on reconstructing full interaction networks from short and noisy time series—a difficult inverse prob-

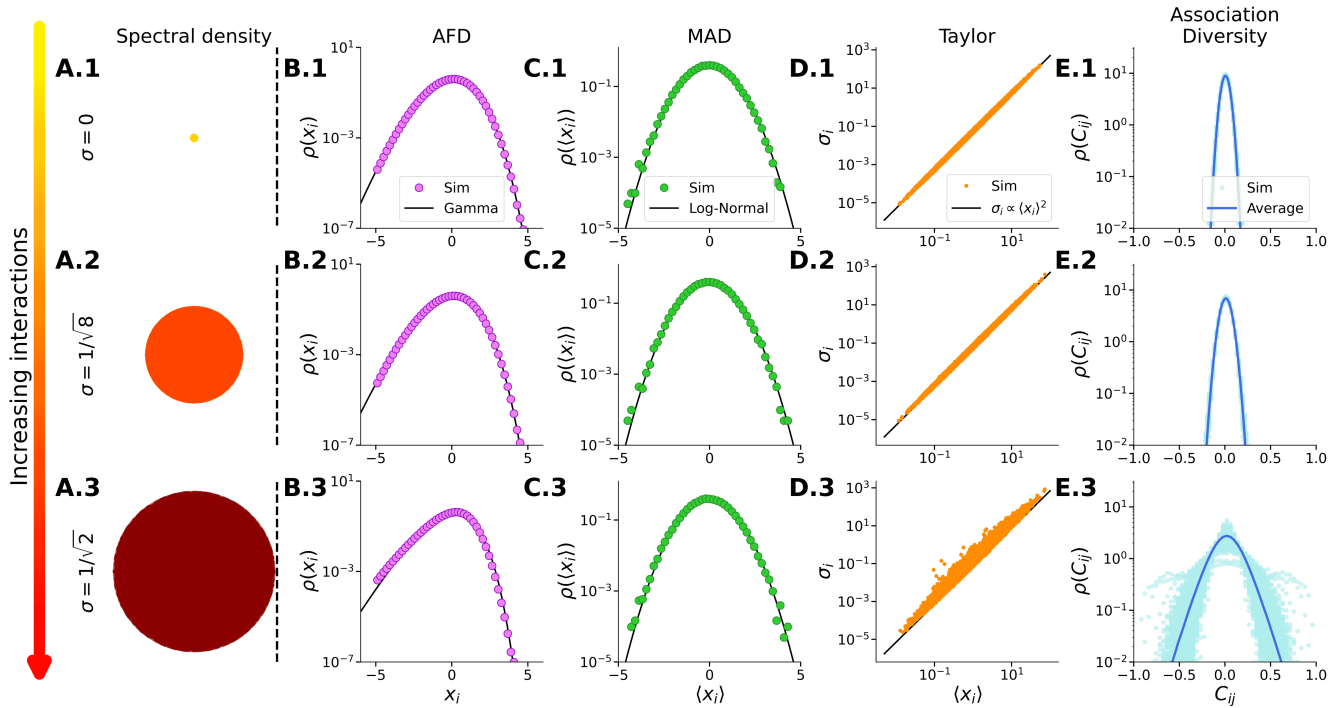


**Figure 3. Grilli's laws are preserved in the interacting ISLM model, while approaching the edge of instability broadens the correlation histogram and enhances association diversity.** **B.1–B.3** Spectral density of the effective interaction matrix in (9) for three values of the interaction strength: B.1  $\sigma = 0$  (pure SLM), B.2  $\sigma = 1/\sqrt{8}$ , and B.3  $\sigma = 1/\sqrt{2}$ . The connectivity is fixed at  $C = 1/2$ , so panel B.3 lies exactly at the edge of instability. We use  $\mu_{LN} = 0$  and  $\sigma_{LN} = 1$  for the log-normal parameters. **C.1–C.3** Abundance fluctuation distribution (AFD) for the same values of  $\sigma$ . Points show simulation results for a community with  $S = 200$  species, integrated up to  $t_{\max} = 100$  with time step  $h = 0.01$ , noise variance  $\sigma_0 = 1$ , and growth time scale  $\tau = 1$ , averaged over  $M = 500$  independent realizations. The black line is the best-fit Gamma distribution. **D.1–D.3** Mean abundance distribution (MAD). Green dots are simulation results; the black curve is the log-normal distribution from which the values of  $-1/D_{ii}$  are drawn. **E.1–E.3** Taylor's law. Points show the empirical relationship between mean and standard deviation from simulations; the black line is the theoretical scaling  $\sigma_i \propto \langle x_i \rangle^2$  (plotted as  $y = x^2$ ). **H.1–H.3** Association diversity for the three values of  $\sigma$ . For small and intermediate interaction strengths (H.1–H.2) the correlation histograms are narrow, while at the edge of instability (H.3) they become much broader. Light points correspond to different realizations of the quenched disorder, and the dark line shows their average, highlighting the multitude of possible correlation patterns compatible with the same single-species macroecological laws.

lem with well-known caveats [16, 65].

Here we take a complementary approach and test whether healthy and dysbiotic microbiomes differ in their proximity to the ISLM edge of instability. Importantly, this distance can be inferred directly from the breadth of short-time pairwise correlations, without reconstructing microscopic interaction networks. We therefore apply the same pipeline used above for environmental microbiomes to estimate the stability parameter  $g$  from human gut metagenomic datasets, comparing healthy individuals with multiple dysbiosis-associated conditions, such as inflammatory bowel disease (IBD), irritable bowel syndrome (IBS), colorectal cancer (CRC), and Clostridioides difficile infection (CDI).

The correlation histograms (Fig. 5A–C) already suggest a systematic difference between groups: healthy subjects display slightly broader, more heterogeneous as-

sociations and a larger mean stability estimate,  $\langle g \rangle \approx 0.86$ , whereas ulcerative colitis and Crohn's disease microbiomes show progressively narrower histograms and smaller values,  $\langle g \rangle \approx 0.77$  and  $\langle g \rangle \approx 0.74$ , respectively. Pooling subjects within each group (Fig. 5D) yields significantly separated  $g$  distributions: the two independent healthy cohorts overlap and lie markedly closer to the edge of instability ( $g = 1$ ) than the inflammatory bowel disease (IBD) cohorts (ulcerative colitis and Crohn's disease). To quantify this separation, we treat the individual  $g$  estimates as samples and compute the area under the receiver operating characteristic (ROC) curve between pairs of diagnoses (see SI Section 6.B/C for methodological details and SI Section 6.E for the resulting AUC values).

As a null check, reshuffling bacterial abundances across samples (randomly reassigning each species' abundance

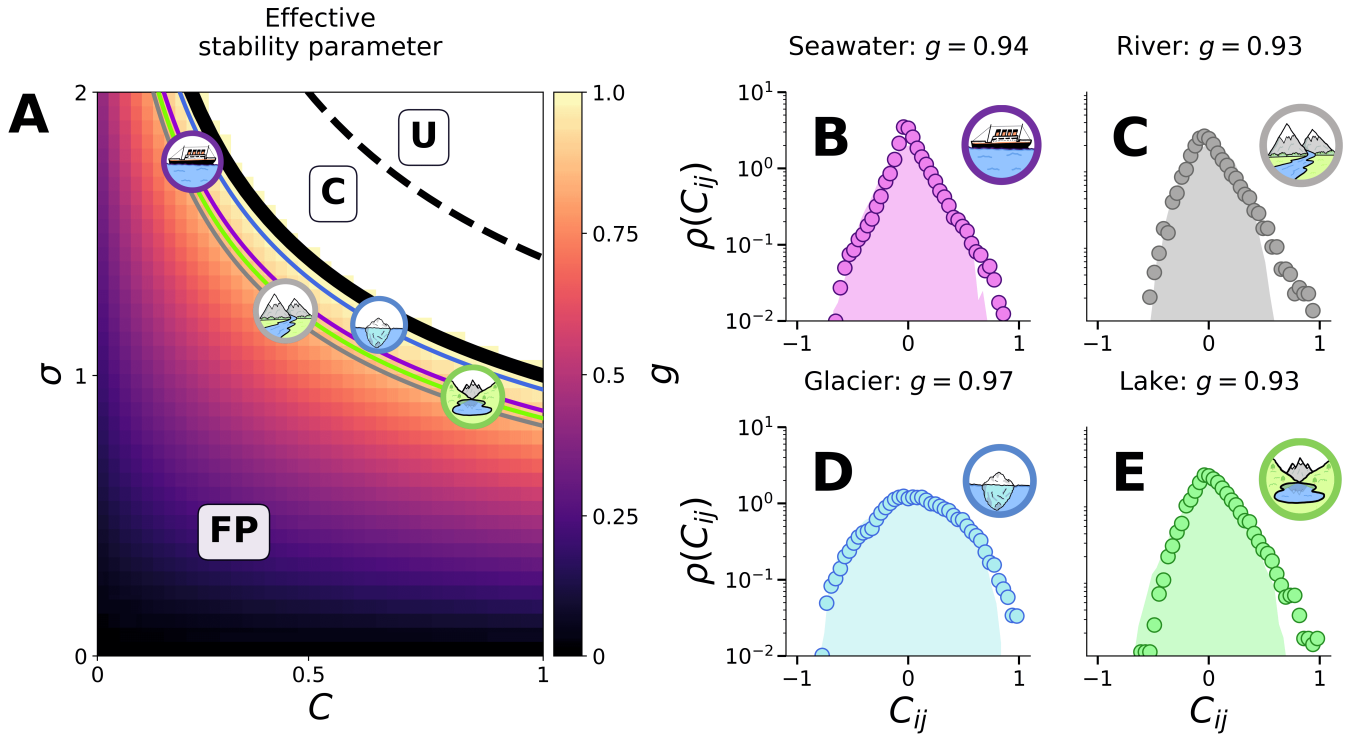


**Figure 4. Empirical biomes are found more likely at the edge of instability.** **A.** Distance to the edge of instability, measured via the estimator of (12). The color map shows the value of  $g$ . The black line shows the boundary of instability ( $\sigma\sqrt{C} = 1$ ). Below this boundary, the fixed point solution is stable and, above it, it becomes linearly unstable. Four different lines are shown in violet, grey, blue and green, indicating each of the four microbiomes analyzed: Seawater (Panel B), River (Panel C), Glacier (Panel D) and Lake (Panel E), respectively. Lines depict the possible combinations of  $(\sigma, C)$  giving rise to the reported values of  $g$ , measured for each biome. **B-E** Histograms of correlations for the four microbiomes, each with their own inferred value of  $g$ . Points show empirical values; shades show the best fit found by simulating the dynamics for  $S = 200$  and  $M = 10^3$  different realizations of the quenched disorder at the value of  $\sigma$  needed to reproduce the empirical  $g$  (with fixed  $C = 0.5$ ).

profile to different individuals) destroys the correlation structure and collapses these differences in  $g$  (inset to Fig. 5D), confirming that the signal in  $g$  originates from genuine dynamical correlations rather than from potential confounders such as sampling noise. Across additional disease cohorts analyzed with the same pipeline (IBS, CRC, CDI; Fig. 5E–G), the same qualitative pattern holds: healthy microbiomes systematically sit closer to the critical regime of the ISLM ensemble, whereas dysbiosis is associated with a robust shift toward more strongly stable states with reduced dynamical diversity and reactivity to perturbations. The sampling scheme used to construct the covariance matrices and  $g$  distributions in Fig. 5 (subsampling parameters and cohort-specific filters) is described in SI Section 6.B/D, and its robustness to changes in these choices is examined in SI Section 6.F. Finally, as a negative control, we analyzed healthy subjects from two independent studies (SI Section 6.G): over a broad range of sampling parameters, these two groups are not separable by our estimator, indicating that the procedure does not generate spurious

differences between comparable healthy cohorts.

## DISCUSSION

Microbial macroecology poses an apparent puzzle. On the one hand, a simple effective stochastic logistic model (SLM) without inter-species interactions already reproduces the single-species macroecological laws of Grilli *et al.*. On the other hand, experiments and clinical evidence show that interactions in microbiomes are central to stability, function, and disease: for example, they have been implicated in gut disorders such as Crohn’s disease and inflammatory bowel conditions [66–68], and several current treatments explicitly harness competitive interactions among bacteria [69, 70].

Reconciling these two facts requires models in which interactions can be strong and structurally diverse without destroying the robust one-point statistics captured by the SLM. In this work, we address this tension by constructing a minimal, analytically tractable interacting stochastic logistic model (ISLM) that preserves the SLM

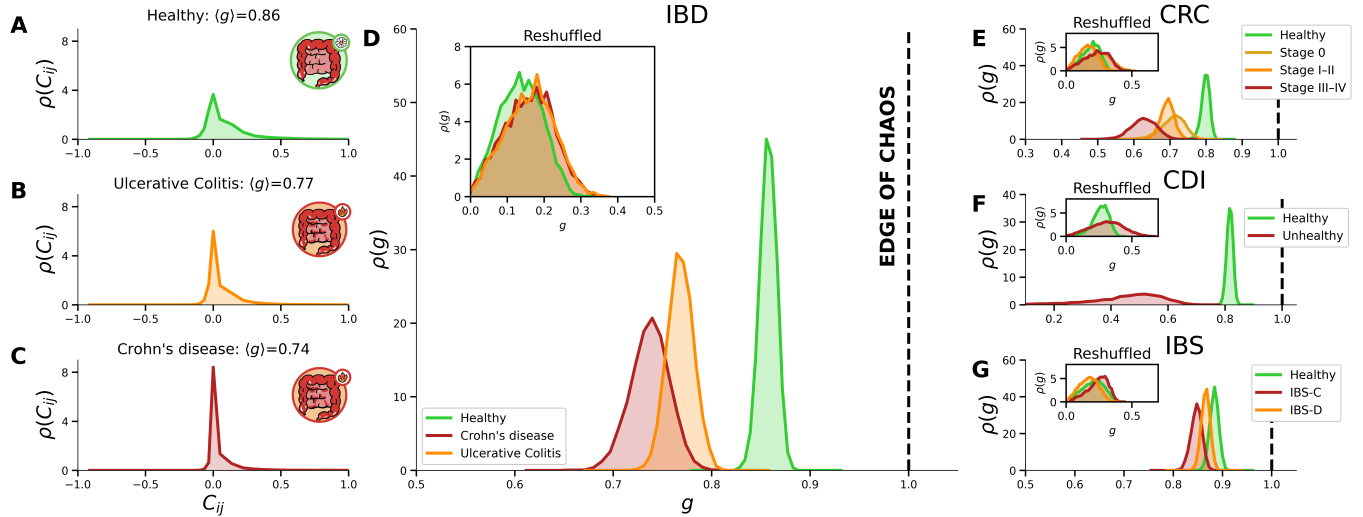


**Figure 5. Dysbiosis-associated conditions are farther from the critical point than healthy cohorts.** (A–C) Distributions of pairwise species–species correlations  $\rho(C_{ij})$  for Healthy controls (A), Ulcerative Colitis (B), and Crohn’s disease (C) gut microbiomes. For each cohort we generated  $M = 1000$  independent subsamples; each subsample contains  $T_2 = 200$  randomly selected samples (without replacement within a subsample). An occupancy filter of 0.2 was applied so that only taxa present in at least 20% of the selected samples were retained, yielding  $\sim 100$  taxa per dataset. (D) Distributions of the estimated distance to criticality  $g$  for the four groups (two healthy cohorts (group 1 and group 2); two disease cohorts (UC, CD). Brackets report the AUC p-value between (i) the two disease cohorts (U–U), (ii) the two healthy cohorts (H–H), and (iii) pooled Unhealthy versus pooled Healthy (U–H). Small p-values indicate evidence for distributional differences; the U–H contrast shows clear separation (at least for the available data), whereas H–H is not significant and U–U shows a modest shift. As an interpretable effect size, the *AUC* equals the probability that a randomly chosen value from one group exceeds a value from the other; in this setting it quantifies separability of both distributions. The inset (*Reshuffled*) shows  $g$  after random reshuffling that destroys the association between taxa and samples; the distinctive cohort structure disappears, confirming that the observed separations arise from genuine ecological organization rather than sampling artifacts.

backbone at the level of single-species statistics while embedding species in a high-dimensional interaction ensemble, where interaction networks are encoded by a balanced Gaussian matrix built on log-normally distributed self-interaction terms and subject to environmental noise.

Dynamic mean-field theory (DMFT) shows that this ensemble exhibits a phase diagram with a stable fixed-point phase, a chaotic phase, and an unbounded phase, separated by an instability line that obeys a May-like linear-stability criterion. Remarkably, throughout the stable phase the DMFT effective process reduces exactly to the one-species stochastic logistic equation, so the three macroecological laws (AFD, MAD, Taylor’s law) remain intact even as interactions strongly reshape community-level dynamics. This provides a natural explanation for why a non-interacting model such as the stochastic logistic model can successfully capture macroecological patterns of empirical (interacting) microbiomes. In this sense, the ISLM acts as a “Van der Waals correction” to the ecological ideal gas: it preserves the successful mean-field description of marginal abundances while enriching the dynamical and associational structure.

Finite-community-size (beyond-mean-field) corrections around the DMFT solution generate nonzero species-species covariances, whose distribution broadens

as the instability line is approached. Extending previous theoretical frameworks [71–74] to our ISLM ensemble and to short-time covariances, we derive an estimator for a single stability parameter  $g$  that can be inferred directly from empirical covariance distributions and community size. In our parametrization,  $g = 1$  marks the edge of instability, so  $g$  acts as an effective order parameter: it determines the width of the correlation histogram and places communities in the  $(C, \sigma)$  phase diagram without reconstructing the full microscopic interaction network.

Applying this framework to synthetic data confirmed that the estimator behaves as expected and that, near the edge, the model generates a wide variety of correlation patterns across realizations while preserving single-species statistics. We then used the same pipeline on transversal and longitudinal microbiome data from several natural environments, including aquatic, glacial, and others. All these biomes are found to operate close to the instability line ( $g \approx 0.93$ –0.97), with systematic but modest differences between environments. Biomes with larger  $g$  display broader empirical correlation histograms, consistent with the theoretical prediction that association diversity increases as communities approach the edge of instability. Relatedly, our conclusion that

microbiomes operate near the edge of instability echoes recent work on ecological “collectivity,” quantified by the spectral radius of the interaction matrix normalized by self-regulation, which increases as indirect effects propagate more broadly through the community [75, 76]. In this sense, their collectivity metric and our distance to the May-like instability line capture the same underlying mechanism: as the dominant spectral scale approaches its critical threshold, community-wide fluctuations and heterogeneous covariation are amplified.

Focusing next on the human gut, we asked whether health and disease differ in their distance to instability [77–79]. Across multiple cohorts, healthy microbiomes consistently show broader, more heterogeneous association patterns and larger values of  $g$  than dysbiosis-associated states. In particular, inflammatory bowel disease cohorts (ulcerative colitis and Crohn’s disease) exhibit narrower correlation histograms and lower  $g$  than healthy controls [67, 68, 80], indicating a retreat from the edge of instability. The same qualitative shift is observed in additional conditions commonly linked to dysbiosis (IBS, CRC, CDI; see Fig. 5), and it is robust to changes in filtering and inference parameters (see SI Section 6.F). Null reshuffling tests, which destroy data structure while preserving marginal abundances, largely collapse these differences, confirming that they arise from genuine dynamical organization rather than from static sampling artifacts.

Thus, our results suggest that  $g$  may offer a simple and robust dynamical marker of microbiome health. Distinguishing healthy from dysbiotic communities remains a long-standing challenge [81, 82], with many proposed signals—most notably reduced diversity—proving non-universal across diseases [83–86]. In contrast,  $g$  consistently separates healthy from diseased individuals while showing no significant differences between independent healthy cohorts, indicating that it captures a reproducible and disease-relevant signal of the underlying ecological dynamics. Moreover, its computation relies solely on abundance covariances, making it fast, data-efficient, and independent of any explicit inference of the interaction network.

Conceptually, our work connects several research lines. It embeds ensemble-based approaches to microbiome inference within the dynamical phase structure of high-dimensional ecological models, extending May’s stability criterion to a setting that preserves realistic single-species macroecology. It shows that a simple, random-interaction extension of the SLM is sufficient to reconcile universal one-point statistics with the observed breadth and variability of pairwise associations. And it translates these ideas into a practical inference tool: the scalar parameter  $g$ , estimated from short time series, provides a coarse but interpretable summary of community dynamics that can stratify health states and potentially track progression. In doing so, it brings the analysis of mi-

crobiomes closer to the classical framework of community ecology based on generalized Lotka-Volterra models, and highlights microbial communities as an exceptional testbed for stability-diversity theory and other ecological laws that are difficult to probe in macroscopic ecosystems.

At the same time, our framework is merely a first step, with important limitations that future work will need to address. First, it rests on strong but transparent modeling assumptions: interactions are treated as pairwise and random with Gaussian statistics and constrained only by balance and sparsity; environmental noise is taken as unstructured and multiplicative; and spatial structure, migration, and explicit resource dynamics are neglected. Real microbiomes undoubtedly display more structured interactions and stronger phylogenetic and metabolic constraints, and—in the human gut, for example—are further shaped by host-mediated feedbacks [78]. Moreover, correlations between species can arise not only from direct interactions but also from shared environmental responses or phylogenetic similarity, which we do not model explicitly here [15]. Our demonstration that pairwise direct interactions drawn from a simple ensemble can reproduce broad association patterns should therefore be viewed as a proof of concept rather than a claim that this is the sole mechanism behind observed correlations.

Second, we have restricted in our parsimonious modeling approach to pairwise interactions of Lotka-Volterra type. There is growing evidence that higher-order interactions, which naturally emerge in coarse-grained consumer-resource models, may play an important role in community stability and in the relationship between diversity and robustness [15, 87, 88]. Let us underline, however, that notably, when tuned close to the edge of instability, this pairwise model also generates non-trivial higher-order correlations [23, 89], which could be directly compared with empirically measured multi-species statistics as these become available.

Also, demographic noise and immigration are omitted. While demographic noise appears subdominant to environmental fluctuations for the macroecological laws we consider, and immigration mainly affects dynamics far from steady state, both ingredients might be relevant in open, spatially extended ecosystems and could modify the effective position of communities in the phase diagram.

These caveats point to natural extensions. On the theoretical side, it will be important to incorporate additional structure into the interaction ensemble—such as consumer-resource constraints, trophic or metabolic layers, or phylogenetic dependence—and to explore the impact of higher-order interactions, space, and migration. On the empirical side, controlled perturbation experiments and longer longitudinal datasets could test more directly whether communities with larger  $g$  indeed dis-

play stronger and more diverse responses to perturbations, and whether therapeutic interventions that restore health (e.g., diet, probiotics, fecal microbiota transplantation) drive  $g$  back toward the critical regime identified here.

In summary, our study suggests that association diversity in microbiomes is not an incidental byproduct of noise and sampling, but a quantitative reflection of where communities sit in a dynamical phase diagram. By linking broad, realization-dependent correlation patterns to a simple stability parameter and showing that this parameter stratifies microbiome health states, we provide a bridge between macroecological laws, interaction ensembles, and the broader idea that some aspects of living systems may have evolved to exploit functional advantages by operating near the edge of a phase transition—without necessarily being tuned to an exact critical point.

## MATERIALS AND METHODS

### Numerical integration of stochastic dynamics and Lyapunov exponents

We simulate the interacting stochastic logistic model (ISLM) by numerically integrating the stochastic differential equations in Eq. (1) using a Milstein scheme [90]. Time is discretized in steps of size  $h$  (typically  $h = 10^{-2}$ , with smaller values checked for convergence), and at each step both the deterministic drift and the multiplicative noise term are updated using the standard Milstein scheme for scalar stochastic differential equations with linear multiplicative noise, which ensures positivity of the solutions. Unless otherwise stated, we integrate up to a maximum time  $t_{\max}$ , discard an initial transient, and sample species abundances at regular intervals to estimate macroecological observables (abundance-fluctuation distributions, mean-abundance distributions, Taylor's law) and covariance matrices.

To characterize dynamical regimes and locate the onset of chaos, we computed the largest Lyapunov exponent (LLE) using the classical Benettin algorithm [91]. For a given realization of the quenched disorder and noise, we evolve in parallel a reference trajectory and a perturbed trajectory, initialized with an infinitesimal separation  $\delta x(0)$  and driven by the *same* realization of the stochastic noise. At fixed time intervals  $\Delta t$ , we measure the norm of the separation, renormalize it to a fixed small value, and accumulate the finite-time growth rates. The LLE is then estimated as the long-time average of these growth rates. A positive LLE indicates chaotic dynamics, while a negative LLE corresponds to a stable fixed-point regime; the transition between these regimes defines the edge of instability in the  $(C, \sigma)$  parameter space.

### Construction of the random Gaussian interaction ensemble

The random interaction ensemble is constructed in two steps: we first draw a sparse, row-balanced Gaussian matrix  $G$  and then obtain the interaction matrix  $M$  and the full community matrix  $A$  by rescaling with the fixed point  $x^*$ .

Given the number of species  $S$  and connectance  $C$ , we start from a dense Gaussian matrix  $G^{(0)}$  with independent entries  $G_{ij}^{(0)} \sim \mathcal{N}(0, 1/S)$ . We then draw an independent Bernoulli mask  $B_{ij}$  with  $\mathbb{P}(B_{ij} = 1) = C$  and set  $B_{ii} = 0$ , so that only a fraction  $C$  of the off-diagonal entries are retained. The masked matrix is  $G_{ij} = B_{ij} G_{ij}^{(0)}$ , with  $G_{ii} = 0$ . To enforce row balance, we subtract from each non-zero off-diagonal entry in row  $i$  the mean over the kept entries in that row:

$$\mu_i = \frac{\sum_j G_{ij}}{\sum_j B_{ij}}, \quad G_{ij} \leftarrow G_{ij} - \mu_i \quad \text{for all } j \text{ with } B_{ij} = 1. \quad (14)$$

After this operation, each row satisfies  $\sum_j G_{ij} = 0$ , i.e.  $G\mathbf{1} = 0$ , and the diagonal remains zero. The diagonal matrix  $D$  is fixed by the uncoupled stochastic logistic model: we prescribe a deterministic fixed point vector  $x^*$  and set  $D = -\text{diag}(1/x^*)$ , so that  $\text{diag}(x^*) = -D^{-1}$ , as in (4). The interaction matrix  $M$  is then obtained by rescaling  $G$  with the components of  $x^*$ ,  $M = -GD = G\text{diag}(1/x^*)$ . By construction,  $M$  has zero diagonal and satisfies (7),  $Mx^* = G\text{diag}(1/x^*)x^* = G\mathbf{1} = 0$ , so that turning on interactions does not shift the fixed point. Finally, interactions are introduced as a perturbation of the uncoupled SLM via (8)  $A = D + \sigma M = D - \sigma GD$ , and the effective stability matrix entering the linearized dynamics around  $x^*$  reads as in (9),  $A_{\text{eff}} = \frac{1}{\tau}(-I + \sigma G)$ , which directly links the Gaussian ensemble for  $G$  to the spectrum of the effective Jacobian (see SI Section 1 for further details and analytical results).

### Estimation of the distance to criticality from covariance matrices

As shown in the SI (see Section 4 for details), in the fixed-point phase of the ISLM, the distance to criticality can be quantified by a single parameter  $g$  defined through the leading eigenvalue  $\lambda$  of the effective stability matrix,  $\lambda = 1 - g^2$ . Within dynamical mean-field theory, the normalized width of the distribution of short-time covariances provides an explicit relation between  $\lambda$  and the empirical covariance matrix.

Given a covariance (or correlation) matrix  $C$  of size  $S \times S$ , we define the normalized width  $\Delta$  as in (13). This quantity can be linked to the short-time limits of the four-point observable,  $\Psi^{\text{short}}$ , and the average variance of the effective single-species process,  $C_y^{\text{short}}$ , in the DMFT

description (see SI Section 4 for explicit definitions):

$$S\Delta^2 := \frac{\Psi^{\text{short}}}{(C_y^{\text{short}})^2} - 1. \quad (15)$$

In the ISLM this quantity is related to the leading eigenvalue  $\lambda$  by (12), with  $\lambda \in (0, 1]$  in the stable phase.

To estimate the distance to criticality from data, we proceed as follows. For each community or cohort, we first compute a short-time covariance matrix  $C$  by subsampling the time series (or individuals) with the procedure detailed in the SI (Section 6.B). From  $C$  we compute  $\Delta$  and the scalar quantity  $A = S\Delta^2$ . (12) is then solved numerically for  $\lambda$  by introducing  $x = \sqrt{\lambda}$ , which yields a quartic equation

$$x^4 - (8A + 6)x^3 + 4x^2 - 2x + 3 = 0. \quad (16)$$

Among its real positive roots, we select the physically admissible solution  $x \in (0, 1]$ , corresponding to  $\lambda = x^2 \in (0, 1]$ . The distance to criticality is finally obtained as  $g = \sqrt{1 - \lambda}$ , which coincides with the interaction parameter in our parametrization ( $g = \sigma\sqrt{C}$ ) in the mean-field limit.

### Data Availability

All microbiome data analyzed in this study were previously published. For the analysis of different diseases and the impact on gut-microbiome dynamics, we used the following datasets:

- **IBD:** Metagenomic data from the Inflammatory Bowel Disease Multi'omics Database (IBDMDB, <https://ibdmd.org/>) and Ref. [92].
- **IBS:** Metagenomic data from Ref. [93].
- **CDI:** Metagenomic data from Ref. [94].
- **CRC:** Metagenomic data from Ref. [95].
- **Independent healthy cohorts:** Two independent healthy-control cohorts based on 16S rRNA sequencing from Ref. [96].

The environmental and human-gut microbiome datasets used to characterize macroecological patterns and association diversity are the same as in Ref. [5].

### Data processing

*Environmental microbiomes (Fig. 4)* For the biome analysis in Fig. 4 we use the same environmental microbiome datasets as in [5], comprising glacier, lake, river and seawater communities, all of them cross-sectional.

For each biome we start from the species-by-sample relative-abundance table of Ref.[5] and apply an occupancy filter to remove extremely rare taxa. Specifically, for a given occupancy threshold  $o$  we retain only the most prevalent species, i.e. those present in at least a fraction  $o$  of the samples in that biome. This yields an effective number of species  $S$ , together with a number of samples  $T$  for each choice of  $o$ , and we define the units-to-samples ratio  $r = S/T$ . We explore several occupancy thresholds (e.g.  $o = 0.5, 0.95, 0.99$ ) and, for each biome, select the threshold that minimizes  $r$  under the constraint  $S \geq 100$ . The resulting values of  $o$ ,  $S$ ,  $T$  and  $r$  for all biomes are summarized in Table I.

Biome	chosen $o$	$S$	$T$	$r = S/T$
Glacier	0.99	260	30	8.67
Lake	0.95	132	198	0.67
River	0.95	147	188	0.78
Seawater	0.50	199	474	0.42

Table I. Occupancy thresholds  $o$  selected for the environmental biomes in Fig. 4, together with the resulting number of species  $S$ , number of samples  $T$ , and aspect ratio  $r = S/T$  (selection criterion: minimize  $r$  with  $S \geq 100$ ).

*Human gut cohorts and disease datasets (Fig. 5)* For the analysis of human gut microbiome data under different diseases (IBD, IBS, CRC, CDI and independent healthy cohorts) we follow the preprocessing and subsampling pipeline described in detail in SI Section 6.B. Briefly, for each study we construct a taxa-by-sample table of relative abundances, apply the same basic filtering steps as in the biome datasets (removing extremely low-occupancy taxa and samples with insufficient coverage), and restrict the analysis to taxa passing a study-specific occupancy threshold. Disease cohorts are typically cross-sectional: each sample corresponds to one individual, and subsamples used for estimating  $g$  are constructed by randomly drawing groups of individuals within each diagnosis category.

*Disease separation from distance to criticality* After filtering, the abundance of each retained taxon is standardized across samples within a given biome or cohort (subtracting the sample mean and dividing by the sample standard deviation). We then compute the empirical covariance matrix  $C$  of these standardized variables. The width of the covariance distribution is summarized by the normalized second moment  $\Delta$  defined in (13). We then use the dynamical mean-field relation of (12) to solve for the leading eigenvalue  $\lambda$  and infer the distance to criticality  $g = \sqrt{1 - \lambda}$ . Repeating this procedure over many subsamples within each biome or diagnosis group yields the distributions of  $g$  reported in Figs. 4 and 5; full details, including the choice of subsample size and the number of repetitions per cohort, are given in SI Sections 6.C–6.F.

For each biome or diagnosis group, the pipeline de-

scribed above and in SI Section 6.B yields a distribution of distance-to-instability estimates  $g$  obtained from many short-time subsamples. To quantify how well  $g$  separates healthy and diseased microbiomes, we treat the individual  $g$  values as classification scores and perform a receiver operating characteristic (ROC) analysis between pairs of groups. For a given pair (e.g. healthy vs. ulcerative colitis), we compute the area under the curve (AUC) as a non-parametric measure of separation (SI Section 6.C). An AUC of 1 (or 0) corresponds to perfect separation by  $g$ , whereas AUC = 0.5 indicates no discriminative power. In the main text we report AUC values and associated confidence intervals (estimated by resampling  $g$  values within each group) as our summary statistics for the degree of separation between diagnoses (SI Section 6.E).

As controls, we compare independent healthy cohorts from different studies, for which AUC values remain close to 0.5 over a broad range of sampling parameters, indicating that our estimator does not generate spurious differences between comparable healthy groups (SI Section 6.G).

This work has been supported by Grant No. PID2023-149174NB-I00 financed by the Spanish Ministry and Agencia Estatal de Investigación MCIU/AEI/10.13039/501100011033 and EDRF funds. We are thankful to Jacopo Grilli, William Shoemaker, Samir Suweis and Aniello Lampo for enlightening discussions.

cal stability emerges at the level of strains in the human gut microbiome, *mBio* **14**, e02502 (2023), <https://journals.asm.org/doi/pdf/10.1128/mbio.02502-22>.

- [9] C. K. Fisher and P. Mehta, Identifying keystone species in the human gut microbiome from metagenomic time-series using sparse linear regression, *PLoS ONE* **9**, e102451 (2014).
- [10] K. M. Martini, S. S. Boddu, M. N. Taylor, I. Nemenman, and N. M. Vega, Correlations in microbial abundance data reveal host-bacteria and bacteria-bacteria interactions jointly shaping the *C. elegans* microbiome, *Physical Review Research* **6**, 043219 (2024).
- [11] A. Carr, C. Diener, N. S. Baliga, and S. M. Gibbons, Use and abuse of correlation analyses in microbial ecology, *The ISME journal* **13**, 2647 (2019).
- [12] S. Pinto, E. Benincà, E. H. van Nes, M. Scheffer, and J. A. Bogaards, Species abundance correlations carry limited information about microbial network interactions, *PLoS Comp. Biol.* **18**, e1010491 (2022).
- [13] P.-Y. Ho, B. H. Good, and K. C. Huang, Competition for fluctuating resources reproduces statistics of species abundance over time across wide-ranging microbiotas, *eLife* **11**, e75168 (2022).
- [14] J. Camacho-Mateu, A. Lampo, M. Sireci, M. A. Muñoz, and J. A. Cuesta, Sparse species interactions reproduce abundance correlation patterns in microbial communities, *Proceedings of the National Academy of Sciences* **121**, e2309575121 (2024).
- [15] M. Sireci, M. A. Muñoz, and J. Grilli, Environmental fluctuations explain the universal decay of species-abundance correlations with phylogenetic distance, *Proceedings of the National Academy of Sciences* **120**, e2217144120 (2023).
- [16] K. Faust and J. Raes, Microbial interactions: from networks to models, *Nature Reviews Microbiology* **10**, 538–550 (2012).
- [17] R. R. Stein, V. Bucci, N. C. Toussaint, C. G. Buffie, G. Rätsch, E. G. Pamer, C. Sander, and J. B. Xavier, Ecological modeling from time-series inference: Insight into dynamics and stability of intestinal microbiota, *PLoS Computational Biology* **9**, e1003388 (2013).
- [18] O. S. Venturelli, A. V. Carr, G. Fisher, R. H. Hsu, R. Lau, B. P. Bowen, S. Hromada, T. Northen, and A. P. Arkin, Deciphering microbial interactions in synthetic human gut microbiome communities, *Molecular Systems Biology* **14**, e8157 (2018).
- [19] K. Z. Coyte, J. Schluter, and K. R. Foster, The ecology of the microbiome: Networks, competition, and stability, *Science* **350**, 663–666 (2015).
- [20] N. Masuda, Z. M. Boyd, D. Garlaschelli, and P. J. Mucha, Introduction to correlation networks: Interdisciplinary approaches beyond thresholding, *Physics Reports* **1136**, 1 (2025).
- [21] M. Castro, R. Vida, J. Galeano, and J. A. Cuesta, Scarce data, noisy inferences and overfitting: the hidden flaws in ecological dynamics modelling, *Journal of the Royal Society Interface* **22**, 20250183 (2025).
- [22] R. Zapién-Campos, F. Bansept, and A. Traulsen, Stochastic models allow improved inference of microbiome interactions from time series data, *PLOS Biology* **22**, e3002913 (2024).
- [23] J. Pasqualini, A. Maritan, A. Rinaldo, S. Facchini, E. Savarino, A. Altieri, and S. Suweis, *Microbiomes*

\* mamunoz@onsager.ugr.es

- [1] P. Atkins, J. de Paula, and J. Keeler, *Atkins' Physical Chemistry*, 11th ed. (Oxford University Press, Oxford, 2018) chs. 1–2 summarize the historical development of the ideal-gas law from the 17th–19th centuries.
- [2] R. K. Pathria and P. D. Beale, *Statistical Mechanics*, 4th ed. (Academic Press, London, 2021) chs. 1–3 (kinetic theory, ideal gas), Ch. 7 (equations of state incl. van der Waals), Chs. 12–13 (phase transitions and critical phenomena).
- [3] M. Kardar, *Statistical Physics of Particles* (Cambridge University Press, Cambridge, 2007) sec. 1.3 (Maxwell–Boltzmann), Ch. 7 (mean-field and van der Waals), Chs. 8–9 (critical points and universality).
- [4] W. R. Shoemaker, K. J. Locey, and J. T. Lennon, A macroecological theory of microbial biodiversity ecology, *Nature Ecol. Evol.* **5**, 1 (2017).
- [5] J. Grilli, Macroecological laws describe variation and diversity in microbial communities, *Nature Comm.* **11**, 1 (2020).
- [6] L. Descheemaeker and S. de Buyl, Stochastic logistic models reproduce experimental time series of microbial communities, *eLife* **9**, e55650 (2020).
- [7] B. W. Ji, R. U. Sheth, P. D. Dixit, K. Tchourine, and D. Vitkup, Macroecological dynamics of gut microbiota, *Nature Microbiol.* **5**, 768 (2020).
- [8] R. Wolff, W. Shoemaker, and N. Garud, Ecologi-

Through the Looking Glass: Linking species interactions to dysbiosis through a disordered Lotka–Volterra framework, *eLife* **14**, RP105948 (2025).

[24] F. Roy, M. Barbier, G. Biroli, and G. Bunin, Complex interactions can create persistent fluctuations in high-diversity ecosystems, *PLOS Computational Biology* **16**, e1007827 (2020).

[25] R. May, Will a large complex system be stable?, *Nature* **238**, 413 (1972).

[26] G. Biroli, G. Bunin, and C. Cammarota, Marginally stable equilibria in critical ecosystems, *New Journal of Physics* **20**, 083051 (2018).

[27] A. Altieri, F. Roy, C. Cammarota, and G. Biroli, Properties of equilibria and glassy phases of the random Lotka–Volterra model with demographic noise, *Physical Review Letters* **126**, 258301 (2021).

[28] M. T. Pearce, A. Agarwala, and D. S. Fisher, Stabilization of extensive fine-scale diversity by ecologically driven spatiotemporal chaos, *Proceedings of the National Academy of Sciences* **117**, 14572 (2020).

[29] A. Mahadevan, M. T. Pearce, and D. S. Fisher, Spatiotemporal ecological chaos enables gradual evolutionary diversification without niches or tradeoffs, *Elife* **12**, e82734 (2023).

[30] I. Dalmedigos and G. Bunin, Dynamical persistence in high-diversity resource-consumer communities, *PLoS computational biology* **16**, e1008189 (2020).

[31] D. A. Kessler and N. M. Shnerb, Generalized model of island biodiversity, *Physical Review E* **91**, 042705 (2015).

[32] E. Blumenthal, J. W. Rocks, and P. Mehta, Phase Transition to Chaos in Complex Ecosystems with Nonreciprocal Species-Resource Interactions, *Physical Review Letters* **132**, 127401 (2024).

[33] Y. Liu, J. Hu, H. Lee, and J. Gore, Complex ecosystems lose stability when resource consumption is out of niche, *Physical Review X* **15**, 10.1103/physrevx.15.011003 (2025).

[34] G. Aguadé-Gorgorió and S. Kéfi, Alternative cliques of coexisting species in complex ecosystems, *Journal of Physics: Complexity* **5**, 025022 (2024).

[35] R. C. López, J. A. Bonachela, M. G. Dominguez-Bello, M. Manhart, S. A. Levin, M. J. Blaser, and M. A. Muñoz, Imbalance in gut microbial interactions as a marker of health and disease, *bioRxiv* , 2025 (2025).

[36] G. Bunin, Ecological communities with Lotka–Volterra dynamics, *Physical Review E* **95**, 042414 (2017).

[37] M. A. Muñoz, Colloquium: Criticality and dynamical scaling in living systems, *Reviews of Modern Physics* **90**, 031001 (2018).

[38] T. Mora and W. Bialek, Are biological systems poised at criticality?, *Journal of Statistical Physics* **144**, 268 (2011).

[39] D. R. Chialvo, Emergent complex neural dynamics, *Nature Physics* **6**, 744 (2010).

[40] C. G. Langton, Computation at the edge of chaos: Phase transitions and emergent computation, *Physica D: Non-linear Phenomena* **42**, 12 (1990).

[41] N. Bertschinger and T. Natschläger, Real-time computation at the edge of chaos in recurrent neural networks, *Neural Computation* **16**, 1413 (2004).

[42] W. L. Shew and D. Plenz, The functional benefits of criticality in the cortex, *The Neuroscientist* **19**, 88 (2013).

[43] J. Hidalgo, J. Grilli, S. Suweis, M. A. Muñoz, J. R. Bavares, and A. Maritan, Information-based fitness and the emergence of criticality in living systems, *Proceedings of the National Academy of Sciences of the USA* **111**, 10095 (2014).

[44] J. Hu, D. R. Amor, M. Barbier, G. Bunin, and J. Gore, Emergent phases of ecological diversity and dynamics mapped in microcosms, *Science* **378**, 85 (2022), <https://www.science.org/doi/pdf/10.1126/science.abm7841>.

[45] N. Zamponi, T. S. Grigera, E. Gudowska-Nowak, and D. R. Chialvo, Scale free density and correlations fluctuations in the dynamics of large microbial ecosystems, *arXiv preprint arXiv:2206.12384* (2022).

[46] T. Tao, V. Vu, and M. Krishnapur, Random Matrices: Universality of ESDs and the Circular Law, *Annals of Probability* **38**, 2023 (2010).

[47] S. Allesina and S. Tang, Stability criteria for complex ecosystems, *Nature* **483**, 205 (2012).

[48] K. Rajan and L. F. Abbott, Eigenvalue spectra of random matrices for neural networks, *Physical Review Letters* **97**, 188104 (2006).

[49] H. Sompolinsky, A. Crisanti, and H.-J. Sommers, Chaos in random neural networks, *Physical review letters* **61**, 259 (1988).

[50] E. Mallmin, A. Traulsen, and S. De Monte, Chaotic turnover of rare and abundant species in a strongly interacting model community, *Proceedings of the National Academy of Sciences* **121**, e2312822121 (2024).

[51] J. Camacho-Mateu, A. Lampo, S. Ares, and J. A. Cuesta, Nonequilibrium microbial dynamics unveil a new macroecological pattern beyond taylor's law, *Physical Review E* **110**, 044402 (2024).

[52] Related beyond-mean-field approaches have been developed for neural networks [71–74], where they show that the width of the distribution of (long-time window) correlation pairs diverges as the DMFT fixed-point solution approaches the edge of a transition.

[53] R. Calvo, C. Martorell, A. Roig, and M. A. Muñoz, Robust scaling in human brain dynamics despite latent variables and limited sampling distortions, *arXiv preprint arXiv:2506.03640* (2025).

[54] W. M. de Vos, H. Tilg, M. Van Hul, and P. D. Cani, Gut microbiome and health: mechanistic insights, *Gut* **71**, 1020–1032 (2022).

[55] K. Hou, Z.-X. Wu, X.-Y. Chen, J.-Q. Wang, D. Zhang, C. Xiao, D. Zhu, J. B. Koya, L. Wei, J. Li, and Z.-S. Chen, Microbiota in health and diseases, *Signal Transduction and Targeted Therapy* **7**, 10.1038/s41392-022-00974-4 (2022).

[56] I. Cho and M. J. Blaser, The human microbiome: at the interface of health and disease, *Nature Reviews Genetics* **13**, 260–270 (2012).

[57] Z. Huang, K. Liu, W. Ma, D. Li, T. Mo, and Q. Liu, The gut microbiome in human health and disease—Where are we and where are we going? A bibliometric analysis, *Frontiers in Microbiology* **13**, 10.3389/fmicb.2022.1018594 (2022).

[58] M. Buchanan, Understanding the microbiome (2018).

[59] J. Jovel, L. A. Dieleman, D. Kao, A. L. Mason, and E. Wine, The human gut microbiome in health and disease, in *Metagenomics* (Elsevier, 2018) p. 197–213.

[60] C. A. Lozupone, J. I. Stombaugh, J. I. Gordon, J. K. Jansson, and R. Knight, Diversity, stability and resilience of the human gut microbiota, *Nature* **489**, 220 (2012).

[61] M. Seppi, J. Pasqualini, S. Facchini, E. V. Savarino, and S. Suweis, Emergent functional organization of gut micro-

biomes in health and diseases, *Biomolecules* **14**, 5 (2023).

[62] J. Pasqualini, S. Facchin, A. Rinaldo, A. Maritan, E. Savarino, and S. Suweis, Emergent ecological patterns and modelling of gut microbiomes in health and in disease, *PLOS Computational Biology* **20**, e1012482 (2024).

[63] T. S. Schmidt, J. Raes, and P. Bork, The human gut microbiome: From association to modulation, *Cell* **172**, 1198–1215 (2018).

[64] W. M. de Vos and E. A. de Vos, Role of the intestinal microbiome in health and disease: from correlation to causation, *Nutrition Reviews* **70**, S45–S56 (2012).

[65] K. Faust, Open challenges for microbial network construction and analysis, *The ISME Journal* **15**, 3111–3118 (2021).

[66] P. D. Newell and A. E. Douglas, Interspecies Interactions Determine the Impact of the Gut Microbiota on Nutrient Allocation in *Drosophila melanogaster*, *Appl. Env. Microbiol.* **80**, 788 (2014).

[67] S. Khanna and L. E. Raffals, The Microbiome in Crohn’s Disease: Role in Pathogenesis and Role of Microbiome Replacement Therapies, *Gastroenterol. Clin. N. Am.* **46**, 481 (2017).

[68] D. N. Frank, A. L. S. Amand, R. A. Feldman, E. C. Boedeker, N. Harpaz, and N. R. Pace, Molecular-phylogenetic characterization of microbial community imbalances in human inflammatory bowel diseases, *Proc. Natl. Acad. Sci. USA* **104**, 13780 (2007).

[69] J. de Dios Caballero, R. Vida, M. Cobo, L. Máiz, L. Suárez, J. Galeano, F. Baquero, R. Cantón, and R. del Campo, Individual patterns of complexity in cystic fibrosis lung microbiota, including predator bacteria, over a 1-year period, *mBio* **8**, e00959 (2017).

[70] J. D. Palmer and K. R. Foster, Bacterial species rarely work together, *Science* **376**, 581 (2022).

[71] D. Dahmen, S. Grün, M. Diesmann, and M. Helias, Second type of criticality in the brain uncovers rich multiple-neuron dynamics, *Proceedings of the National Academy of Sciences* **116**, 13051 (2019), number: 26.

[72] D. G. Clark, L. Abbott, and A. Litwin-Kumar, Dimension of Activity in Random Neural Networks, *Physical Review Letters* **131**, 118401 (2023).

[73] D. G. Clark, O. Marschall, A. v. Meegen, and A. Litwin-Kumar, Connectivity structure and dynamics of nonlinear recurrent neural networks (2025), arXiv:2409.01969 [q-bio].

[74] M. Dick, A. Van Meegen, and M. Helias, Linking network- and neuron-level correlations by renormalized field theory, *Physical Review Research* **6**, 033264 (2024).

[75] Y. R. Zelnik, N. Galiana, M. Barbier, M. Loreau, E. Galbraith, and J.-f. Arnoldi, How collectively integrated are ecological communities?, *Ecology Letters* **27**, e14358 (2024).

[76] G. Aguadé-Gorgorió and S. Kéfi, Emergent coexistence and the limits of reductionism in ecological communities, *bioRxiv* , 2025 (2025).

[77] D. A. Relman, The human microbiome: ecosystem resilience and health, *Nutr. Rev.* **70**, S2 (2012).

[78] D. Zheng, T. Liwinski, and E. Elinav, Interaction between microbiota and immunity in health and disease, *Cell Research* **30**, 492 (2020).

[79] M. T. Sorbara and E. G. Pamer, Microbiome-based therapeutics, *Nature Reviews Microbiology* **20**, 365 (2022).

[80] M. Lee and E. B. Chang, Inflammatory Bowel Diseases (IBD) and the Microbiome—Searching the Crime Scene for Clues, *Gastroenterology* **160**, 524 (2021).

[81] M. Van Hul, P. D. Cani, C. Petitfils, W. M. De Vos, H. Tilg, and E. M. El-Omar, What defines a healthy gut microbiome?, *Gut* **73**, 1893–1908 (2024).

[82] E. Rinninella, P. Raoul, M. Clintoni, F. Franceschi, G. A. D. Miggiano, A. Gasbarrini, and M. C. Mele, What is the Healthy Gut Microbiota Composition? A Changing Ecosystem across Age, Environment, Diet, and Diseases, *Microorganisms* **7**, 14 (2019).

[83] F. Magne, M. Gotteland, L. Gauthier, A. Zazueta, S. Pesoa, P. Navarrete, and R. Balamurugan, The firmicutes/bacteroidetes ratio: A relevant marker of gut dysbiosis in obese patients?, *Nutrients* **12**, 1474 (2020).

[84] V. K. Gupta, M. Kim, U. Bakshi, K. Y. Cunningham, J. M. Davis, K. N. Lazaridis, H. Nelson, N. Chia, and J. Sung, A predictive index for health status using species-level gut microbiome profiling, *Nature Commun.* **11**, 10.1038/s41467-020-18476-8 (2020).

[85] J. Halfvarson, C. J. Brislawn, R. Lamendella, Y. Vázquez-Baeza, W. A. Walters, L. M. Bramer, M. D’Amato, F. Bonfiglio, D. McDonald, A. Gonzalez, E. E. McClure, M. F. Dunklebarger, R. Knight, and J. K. Jansson, Dynamics of the human gut microbiome in inflammatory bowel disease, *Nature Microbiology* **2**, 10.1038/nmicrobiol.2017.4 (2017).

[86] Z. Ma, L. Li, and N. J. Gotelli, Diversity-disease relationships and shared species analyses for human microbiome-associated diseases, *The ISME Journal* **13**, 1911 (2019).

[87] J. Grilli, G. Barabás, M. J. Michalska-Smith, and S. Allesina, Higher-order interactions stabilize dynamics in competitive network models, *Nature* **548**, 210 (2017).

[88] A. D. Letten and D. B. Stouffer, The mechanistic basis for higher-order interactions and non-additivity in competitive communities, *Ecology Letters* **22**, 423 (2019).

[89] F. E. Rosas, P. A. Mediano, A. I. Luppi, T. F. Varley, J. T. Lizier, S. Stramaglia, H. J. Jensen, and D. Marinazzo, Disentangling high-order mechanisms and high-order behaviours in complex systems, *Nature Physics* **18**, 476 (2022).

[90] R. Toral and P. Colet, *Stochastic Numerical Methods* (Wiley-VCH, Weingheim, Germany, 2014).

[91] G. Benettin, L. Galgani, A. Giorgilli, and J.-M. Strelcyn, Lyapunov Characteristic Exponents for smooth dynamical systems and for hamiltonian systems; A method for computing all of them. Part 2: Numerical application, *Meccanica* **15**, 21 (1980).

[92] J. Lloyd-Price, C. Arze, A. N. Ananthakrishnan, M. Schirmer, J. Avila-Pacheco, T. W. Poon, E. Andrews, N. J. Ajami, K. S. Bonham, C. J. Brislawn, D. Casero, H. Courtney, A. Gonzalez, T. G. Graeber, A. B. Hall, K. Lake, C. J. Landers, H. Mallick, D. R. Plichta, M. Prasad, G. Rahnavard, J. Sauk, D. Shungin, Y. Vázquez-Baeza, R. A. White, J. Braun, L. A. Denson, J. K. Jansson, R. Knight, S. Kugathasan, D. P. B. McGovern, J. F. Petrosino, T. S. Stappenbeck, H. S. Winter, C. B. Clish, E. A. Franzosa, H. Vlamakis, R. J. Xavier, and C. Huttenhower, Multi-omics of the gut microbial ecosystem in inflammatory bowel diseases, *Nature* **569**, 655–662 (2019).

[93] R. A. Mars, Y. Yang, T. Ward, M. Houtti, S. Priya, H. R. Lekatz, X. Tang, Z. Sun, K. R. Kalari, T. Korem, Y. Bhattarai, T. Zheng, N. Bar, G. Frost, A. J. Johnson, W. van Treuren, S. Han, T. Ordog, M. Grover, J. Sonnenburg, M. D’Amato, M. Camilleri, E. Elinav, E. Segal,

R. Blekhman, G. Farrugia, J. R. Swann, D. Knights, and P. C. Kashyap, Longitudinal multi-omics reveals subset-specific mechanisms underlying irritable bowel syndrome, *Cell* **182**, 1460 (2020).

[94] P. Ferretti, J. Wirbel, O. M. Maistrenko, T. Van Rossum, R. Alves, A. Fullam, W. Akanni, C. Schudoma, A. Schwarz, R. Thielemann, L. Thomas, S. Kandels, R. Hercog, A. Telzerow, I. Letunic, M. Kuhn, G. Zeller, T. S. Schmidt, and P. Bork, *C. difficile* may be overdiagnosed in adults and is a prevalent commensal in infants, *eLife* 10.7554/elife.90111.1 (2023).

[95] S. Yachida, S. Mizutani, H. Shiroma, S. Shiba, T. Nakajima, T. Sakamoto, H. Watanabe, K. Masuda, Y. Nishimoto, M. Kubo, F. Hosoda, H. Rokutan, M. Matsumoto, H. Takamaru, M. Yamada, T. Matsuda, M. Iwasaki, T. Yamaji, T. Yachida, T. Soga, K. Kurokawa, A. Toyoda, Y. Ogura, T. Hayashi, M. Hatakeyama, H. Nakagama, Y. Saito, S. Fukuda, T. Shibata, and T. Yamada, Metagenomic and metabolomic analyses reveal distinct stage-specific phenotypes of the gut microbiota in colorectal cancer, *Nature Medicine* **25**, 968–976 (2019).

[96] J. Park, K. Kato, H. Murakami, K. Hosomi, K. Tanisawa, T. Nakagata, H. Ohno, K. Konishi, H. Kawashima, Y.-A. Chen, A. Mohsen, J.-z. Xiao, T. Odamaki, J. Kunisawa, K. Mizuguchi, and M. Miyachi, Comprehensive analysis of gut microbiota of a healthy population and covariates affecting microbial variation in two large Japanese cohorts, *BMC Microbiology* **21**, 10.1186/s12866-021-02215-0 (2021).

Supplemental Material for:  
 Microbiome association diversity reflects proximity to the edge of  
 instability

Rubén Calvo, Adrián Roig, Roberto Corral López, José Camacho-Mateu, José A. Cuesta,  
 and Miguel A. Muñoz

February 2, 2026

## 1 The Interacting Stochastic Logistic Model (ISLM):

In the main text, we focus on a model of interacting species where the abundance of each species  $i$ , with  $i = 1, 2, \dots, S$ , evolves according to the Langevin equation

$$\dot{x}_i(t) = \frac{x_i(t)}{\tau} \left[ 1 + \sum_{j=1}^S A_{ij} x_j(t) \right] + \sigma_0 x_i(t) \xi_i(t), \quad (1)$$

where  $\xi_i(t)$  is a zero-mean, white noise term with  $\langle \xi_i(t) \xi_j(s) \rangle = \delta(t-s) \delta_{ij}$ . This stochastic differential equation is only well defined after we set a particular interpretation and, in the main text, we mainly discussed Itô's [1]. In this interpretation (i.e. using Itô's calculus), the change of variables  $u_i = \log x_i$ , leads to

$$\frac{d}{dt} \log x_i(t) = \frac{\dot{x}_i}{x_i} - \frac{\sigma_0^2}{2} = \frac{1}{\tau} \left[ \left( 1 - \frac{\sigma_0^2 \tau}{2} \right) + \sum_{j=1}^S A_{ij} x_j(t) \right] + \sigma_0 \xi_i(t). \quad (2)$$

Let us analyze this stochastic differential equation (SDE) in detail.

### 1.1 Mean abundance of each species

Taking averages over noise realizations (denoted  $\langle \cdot \rangle$ ) on both sides of the equation gives

$$\frac{d}{dt} \langle \log x_i \rangle = \frac{1}{\tau} \left( 1 + \sum_{j=1}^S A_{ij} \langle x_j \rangle \right) - \frac{\sigma_0^2}{2}. \quad (3)$$

At stationary states the left-hand side of the previous equation vanishes, i.e.  $\dot{u}_i(t) = 0$ , and one has

$$\frac{\sigma_0^2 \tau}{2} = 1 + \sum_{j=1}^S A_{ij} \langle x_j \rangle, \quad (4)$$

which, in vector form, may be written as

$$A \langle \mathbf{x} \rangle = - \left( 1 - \frac{\sigma_0^2 \tau}{2} \right) \mathbf{1}. \quad (5)$$

Denoting by  $\mathbf{x}^*$  the fixed point of the deterministic limit of (1) (i.e., the limit as  $\sigma_0 \rightarrow 0$ ), then

$$A \mathbf{x}^* = -\mathbf{1} \quad \Rightarrow \quad \langle \mathbf{x} \rangle = \left( 1 - \frac{\sigma_0^2 \tau}{2} \right) \mathbf{x}^*. \quad (6)$$

That is, the addition of the noise term only shifts the position of the fixed point. In particular, if the fixed points are log-normally distributed, so will be the mean abundances of each species after the noise is turned on ( $\sigma \neq 0$ ). Interestingly, this puts an upper limit to how large the noise can be, namely

$$\sigma_0 < \sqrt{\frac{2}{\tau}}. \quad (7)$$

## 1.2 Linear approximation of the dynamics

Linearizing Equation (2) around the fixed point leads to

$$\frac{d}{dt}u_i(t) \approx A_{\text{eff}}u_i(t) + \sigma_0\xi_i(t), \quad \text{with } A_{\text{eff}} = \frac{1}{\tau}A \text{ diag}\left(e^{u_1^*}, \dots, e^{u_S^*}\right), \quad (8)$$

where the fixed point  $\mathbf{u}^*$  (let us denote also  $\tilde{\mathbf{x}}$ , such that  $\exp(\mathbf{u}^*) = \tilde{\mathbf{x}}$ ) is defined (in Itô's interpretation) as

$$\frac{1}{\tau} \left[ \left(1 - \frac{\sigma_0^2\tau}{2}\right) + \sum_{j=1}^S A_{ij} \tilde{x}_j(t) \right] = 0 \quad \Rightarrow \quad \tilde{\mathbf{x}} = \langle \mathbf{x} \rangle. \quad (9)$$

In particular, this means that  $\mathbf{u}^* = \log\langle \mathbf{x} \rangle$ . Substituting into (8) leads to

$$A_{\text{eff}} = \frac{1}{\tau}A \text{ diag}(\langle x_1 \rangle, \dots, \langle x_S \rangle) = \frac{k}{\tau}A \text{ diag}(x_1^*, \dots, x_S^*) = \frac{k}{\tau}(D \cdot \text{diag}(\mathbf{x}^*) + \sigma M \cdot \text{diag}(\mathbf{x}^*)), \quad (10)$$

where we have used the decomposition  $A = D + \sigma M$ , and  $k \equiv (1 - \sigma_0^2\tau/2)$ . Now, because  $D$  and  $M$  were explicitly built such that  $D \cdot \mathbf{x}^* = -\mathbf{1}$  and  $M \cdot \mathbf{x}^* = \mathbf{0}$ , one gets

$$A_{\text{eff}} = \frac{k}{\tau}(-\mathbf{I} + \sigma G), \quad G \equiv M \cdot \text{diag}(\mathbf{x}^*). \quad (11)$$

As  $M$  is, by construction, orthogonal to the fixed point,  $G$  fulfills

$$G \mathbf{1} = M \text{diag}(x^*) \mathbf{1} = M x^* = 0, \quad (12)$$

which imposes the condition that the homogeneous eigenmode  $\mathbf{1}$  is an eigenvector of  $G$  with eigenvalue 0.

## 1.3 Correlations in the linearized model

Once the dynamics are reduced, close to the mean abundances, to a set of linear coupled Ornstein-Uhlenbeck equations, the (short-time) covariance matrix  $\hat{\Sigma}$  can be expressed as the solution to the Lyapunov equation (see e.g. [2] and references therein)

$$A_{\text{eff}}\hat{\Sigma} + \hat{\Sigma}A_{\text{eff}}^T = \sigma_0^2\mathbf{I}. \quad (13)$$

This equation does not admit, in general, a closed-form solution for  $\hat{\Sigma}$  in terms of  $A_{\text{eff}}$ . Let us remark that  $\hat{\Sigma}$  is the covariance matrix for the linearized process in log space  $u_i = \log(x_i/\langle x_i \rangle)$ . If environmental fluctuations are small (i.e., if  $\sigma_0$  is small) then  $u_i \approx x_i/\langle x_i \rangle - 1 = (x_i - \langle x_i \rangle)/\langle x_i \rangle$ . This means that the covariance,  $\Sigma$ , of the original process and the covariance of its linearized counterpart are related as

$$\hat{\Sigma}_{ij} = \frac{\Sigma_{ij}}{\langle x_i \rangle \langle x_j \rangle} = \frac{1}{k^2} \frac{\Sigma_{ij}}{x_i^* x_j^*} \quad \Rightarrow \quad \hat{\Sigma} = D^{-1} \Sigma D^{-1}. \quad (14)$$

On the other hand, the (Pearson's) correlation matrix associated with  $\Sigma$  is

$$C_{ij} = \frac{\Sigma_{ij}}{\sqrt{\Sigma_{ii}\Sigma_{jj}}}, \quad (15)$$

so that:

$$\tilde{C}_{ij} \equiv \frac{\tilde{\Sigma}_{ij}}{\sqrt{\tilde{\Sigma}_{ii}\tilde{\Sigma}_{jj}}} = \frac{\Sigma_{ij}/(x_i^* x_j^*)}{\sqrt{\Sigma_{ii}/(x_i^*)^2 \Sigma_{jj}/(x_j^*)^2}} = \frac{\Sigma_{ij}/(x_i^* x_j^*)}{\sqrt{\Sigma_{ii}\Sigma_{jj}}/(x_i^* x_j^*)} = \frac{\Sigma_{ij}}{\sqrt{\Sigma_{ii}\Sigma_{jj}}} = C_{ij}. \quad (16)$$

Therefore the Pearson's correlation matrix is invariant under this diagonal rescaling:  $\tilde{C}_{ij} = C_{ij}$  for all  $i, j$ .

## 1.4 Condition of linear stability

If the matrix elements  $G_{ij}$ , with  $i, j \in \{1, \dots, S\}$ , are i.i.d., drawn from a distribution with finite first and second moments and such that each row is orthogonal to the vector  $\mathbf{1} = (1, \dots, 1)$ , then in the limit  $S \rightarrow \infty$  the spectral density of  $G$  converges to a uniform distribution bounded in a disk in the complex plane centered at 0 with radius [3, 4]

$$R = \sqrt{S \operatorname{Var}(G_{ij})}. \quad (17)$$

In the main text we choose  $G$  such that  $\operatorname{Var}(G_{ij}) = C/S$  and therefore the limiting spectral radius is

$$R = \sqrt{C}. \quad (18)$$

The effective linear response matrix can be written as

$$\tau A_{\text{eff}} = -\mathbf{I} + \sigma G,$$

so its eigenvalues are contained in a disk of radius  $\sigma\sqrt{C}$  centered at  $-1$  in the complex plane.

The condition for linear stability is

$$\max_{\lambda \in \operatorname{sp}(A_{\text{eff}})} \Re(\lambda) < 0. \quad (19)$$

Combining this condition with the bounds on the spectrum above implies

$$-1 + \sigma\sqrt{C} < 0,$$

which is the resulting stability criterion.

## 2 Grilli's laws for the stochastic logistic model without interactions

We consider the stochastic logistic model (SLM) for the abundance  $x_i(t)$  of species  $i$ ,

$$\dot{x}_i(t) = \frac{x_i(t)}{\tau_i} \left[ 1 + \sum_{j=1}^S A_{ij} x_j(t) \right] + \sigma_0 x_i(t) \xi_i(t), \quad (20)$$

where  $\xi_i(t)$  is a Gaussian white noise with  $\langle \xi_i(t) \rangle = 0$  and  $\langle \xi_i(t) \xi_j(t') \rangle = \delta_{ij} \delta(t - t')$ . In the absence of interactions we take

$$A_{ij} = -\frac{1}{K_i} \delta_{ij}, \quad (21)$$

and assume that all time scales are equal,  $\tau_i = \tau$ . The dynamics of each species is then uncoupled and obeys

$$\dot{x}_i(t) = \frac{x_i(t)}{\tau} \left( 1 - \frac{x_i(t)}{K_i} \right) + \sigma_0 x_i(t) \xi_i(t). \quad (22)$$

In the following we drop the species index  $i$  for clarity and work with a single generic species.

### 2.1 Fokker–Planck equation and stationary distribution

Interpreting (22) in the Itô sense, we can write

$$\dot{x}(t) = f(x) + g(x) \xi(t), \quad (23)$$

with drift and noise amplitude

$$f(x) = \frac{x}{\tau} \left( 1 - \frac{x}{K} \right), \quad g(x) = \sigma_0 x. \quad (24)$$

The corresponding Fokker–Planck equation for the probability density  $P(x, t)$  is

$$\frac{\partial P(x, t)}{\partial t} = -\frac{\partial}{\partial x} [f(x)P(x, t)] + \frac{1}{2} \frac{\partial^2}{\partial x^2} [g^2(x)P(x, t)] = -\frac{\partial}{\partial x} \left[ \frac{x}{\tau} \left( 1 - \frac{x}{K} \right) P \right] + \frac{\sigma_0^2}{2} \frac{\partial^2}{\partial x^2} [x^2 P]. \quad (25)$$

The stationary distribution  $P_*(x)$  satisfies  $\partial_t P_* = 0$ . For a one-dimensional Itô process, the stationary solution of (25) can be written as

$$P_*(x) \propto \frac{1}{g^2(x)} \exp \left( \int^x dy \frac{2f(y)}{g^2(y)} \right). \quad (26)$$

In our case  $g^2(x) = \sigma_0^2 x^2$ , and

$$\frac{2f(y)}{g^2(y)} = \frac{2}{\sigma_0^2} \frac{1}{\tau} \frac{y(1-y/K)}{y^2} = \frac{2}{\sigma_0^2 \tau} \left( \frac{1}{y} - \frac{1}{K} \right). \quad (27)$$

Integrating this expression we obtain

$$\int^x dy \frac{2f(y)}{g^2(y)} = \frac{2}{\sigma_0^2 \tau} \left( \log x - \frac{x}{K} \right) + \text{const.} \quad (28)$$

Substituting into Eq. (26) gives

$$P_*(x) \propto \frac{1}{\sigma_0^2 x^2} \exp \left[ \frac{2}{\sigma_0^2 \tau} \left( \log x - \frac{x}{K} \right) \right] = \text{const} \times x^{\frac{2}{\sigma_0^2 \tau} - 2} \exp \left( -\frac{2x}{\sigma_0^2 \tau K} \right). \quad (29)$$

This is a Gamma distribution

$$P_*(x) = \frac{1}{\Gamma(\alpha) \theta^\alpha} x^{\alpha-1} \exp \left( -\frac{x}{\theta} \right), \quad x > 0, \quad (30)$$

with shape and scale parameters

$$\alpha = \frac{2}{\sigma_0^2 \tau} - 1, \quad \theta = \frac{\sigma_0^2 \tau K}{2}. \quad (31)$$

Thus, in the absence of interactions, the abundance fluctuation distribution (AFD) of each species is Gamma-distributed.

## 2.2 Taylor's law

For a Gamma distribution with parameters  $(\alpha, \theta)$ , the mean and variance are

$$\langle x \rangle = \alpha \theta, \quad \text{Var}(x) = \alpha \theta^2. \quad (32)$$

Eliminating  $\theta$  we obtain

$$\text{Var}(x) = \frac{1}{\alpha} \langle x \rangle^2. \quad (33)$$

(33) is precisely Taylor's law with exponent 2: across species, the variance of abundances scales as the square of the mean, with a prefactor  $1/\alpha$  that is independent of the species identity,

$$\text{Var}(x_i) = \frac{1}{\alpha} \langle x_i \rangle^2, \quad i = 1, \dots, S. \quad (34)$$

In the SLM,  $\alpha$  depends only on the noise amplitude  $\sigma_0$  and the common time scale  $\tau$  (see (31)) and is therefore the same for all species (provided they share the same environmental noise statistics). Differences in carrying capacities  $K_i$  change only the scale parameter  $\theta_i$  and hence the mean abundance  $\langle x_i \rangle$ , but not  $\alpha$ . This hence proves that Taylor's law is fulfilled in the SLM.

### 2.3 Mean abundance distribution (MAD)

In the absence of interactions, each species follows the stochastic logistic dynamics in (22). As shown above, the stationary abundance distribution of a single species is Gamma with parameters

$$\alpha = \frac{2}{\sigma_0^2 \tau} - 1, \quad \theta_i = \frac{\sigma_0^2 \tau K_i}{2}, \quad (35)$$

where  $K_i$  is the carrying capacity of species  $i$ . In Itô's calculus, the stationary mean abundance of species  $i$  is therefore

$$\langle x_i \rangle = \alpha \theta_i = \left( \frac{2}{\sigma_0^2 \tau} - 1 \right) \frac{\sigma_0^2 \tau K_i}{2} = c K_i, \quad c \equiv 1 - \frac{\sigma_0^2 \tau}{2}. \quad (36)$$

Hence the mean abundance is simply a constant dilation of the deterministic fixed point  $x_i^* = K_i$ .

To obtain the mean abundance distribution (MAD) across species, we now assume that the carrying capacities are independently drawn from a log-normal distribution,

$$K_i \sim \text{LogNormal}(\mu_K, \sigma_K^2), \quad (37)$$

i.e.

$$\log K_i \sim \mathcal{N}(\mu_K, \sigma_K^2). \quad (38)$$

Using (36), the mean abundance of species  $i$  is

$$m_i \equiv \langle x_i \rangle = c K_i. \quad (39)$$

Taking logarithms,

$$\log m_i = \log c + \log K_i. \quad (40)$$

Since  $\log K_i$  is Gaussian and  $\log c$  is a constant shift, we obtain

$$\log m_i \sim \mathcal{N}(\mu_K + \log c, \sigma_K^2), \quad (41)$$

which implies that the mean abundances are themselves log-normally distributed,

$$m_i \sim \text{LogNormal}(\mu_K + \log c, \sigma_K^2). \quad (42)$$

Therefore, choosing log-normally distributed carrying capacities directly yields a log-normal mean abundance distribution (MAD) across species. The multiplicative effect of environmental noise in the Itô interpretation appears only as a global dilation factor  $c$  and does not change the log-normal form of the MAD.

## 3 Dynamical Mean Field Derivation of the Effective process

### 3.1 Dynamical model

Here we address the problem of disentangling ecological forces from a statistical-physics perspective. For this, we first focus on a the interacting stochastic logistic model (ISLM). The abundance of species  $i = 1, \dots, S$  evolves according to the set of coupled stochastic differential equations

$$\dot{x}_i(t) = \frac{x_i(t)}{\tau_i} \left[ 1 + \sum_{j=1}^S A_{ij} x_j(t) \right] + x_i(t) \xi_i(t), \quad (43)$$

where  $\tau_i$  sets the characteristic timescale of growth or decline for species  $i$ ,  $A_{ij}$  is the interaction matrix, and  $\xi_i(t)$  is an uncorrelated Gaussian white noise with

$$\langle \xi_i(t) \rangle = 0, \quad \langle \xi_i(t) \xi_j(t') \rangle = \sigma_0^2 \delta_{ij} \delta(t - t'). \quad (44)$$

We decompose the interaction matrix as  $A = D + \sigma M$ , where:

- $D$  is a diagonal matrix that encodes the intrinsic regulation (effective carrying capacity) of each species in the absence of interactions.
- $M$  is a random matrix whose statistics will be chosen to reproduce empirical ecological patterns.
- $\sigma$  controls the overall strength of interactions, continuously interpolating between the uncoupled SLM limit ( $\sigma = 0$ , ideal-gas-like) and a strongly interacting regime ( $\sigma \gg 0$ , Van der Waals-like).

### 3.2 Construction of the interaction matrix

We now specify the statistical ensemble used to generate the interaction matrix  $A$ .

#### Distribution of intrinsic terms

The diagonal elements of  $D$  are sampled independently from a log-normal distribution with negative support:

$$D_{ii} \sim -\log \mathcal{N}(\hat{\mu}, \hat{\sigma}), \quad (45)$$

so that  $D_{ii} < 0$  and each species is self-limiting in the absence of interactions.

For  $\sigma = 0$ , the fixed point  $x^*$  of Eq. (43) is determined by

$$1 + D_{ii} x_i^* = 0 \quad \Rightarrow \quad x_i^* = -\frac{1}{D_{ii}}, \quad (46)$$

which we collect into the diagonal matrix

$$\text{diag}(x^*) = -D^{-1}. \quad (47)$$

#### Random connectivity and weights

To introduce sparse random interactions, we draw two independent random matrices  $B$  and  $Z$ :

$$Z_{ij} \sim \mathcal{N}\left(0, \frac{1}{S}\right), \quad (48)$$

$$B_{ij} \sim \text{Bernoulli}(C), \quad (49)$$

where the connectivity  $C \in [0, 1]$  is the probability that an interaction between  $i$  and  $j$  is present. Equivalently, the distribution of each entry of  $B$  is

$$P(B_{ij}) = C \delta(B_{ij} - 1) + (1 - C) \delta(B_{ij}). \quad (50)$$

We then construct an intermediate random matrix  $G$  with zero row-sum, ensuring that the net interaction of each species is centered. For each row  $i$  we define

$$G_{ij} = B_{ij} \left[ Z_{ij} - \frac{1}{S} \sum_{k=1}^S B_{ik} Z_{ik} \right], \quad (51)$$

so that

$$\sum_{j=1}^S G_{ij} = 0 \quad \text{for all } i. \quad (52)$$

By construction, all entries  $B_{ij}$ ,  $B_{ik}$  and  $Z_{ij}$ ,  $Z_{ik}$  are independent for  $j \neq k$ .

#### Rescaling by the deterministic fixed point

We define the random matrix  $M$  by rescaling  $G$  with the typical abundances  $x^*$  of the uncoupled system:

$$M = G \cdot \text{diag}^{-1}(x^*), \quad \text{diag}(x^*) = -D^{-1}, \quad (53)$$

so that

$$M = -GD. \quad (54)$$

Hence the full interaction matrix

$$A = D + \sigma M = D - \sigma GD \quad (55)$$

has components

$$A_{ij} = \begin{cases} D_{ii}, & i = j, \\ -\sigma D_{jj} G_{ij}, & i \neq j. \end{cases} \quad (56)$$

The sum of all entries of  $A$  can therefore be expressed as

$$\sum_{i,j} A_{ij} = \sum_i D_{ii} - \sigma \sum_{i \neq j} D_{jj} G_{ij}. \quad (57)$$

Our strategy is to construct the generating functional of the stochastic dynamics and then integrate over the random degrees of freedom associated with  $Z$  and  $B$ . Since the diagonal entries  $D_{ii}$  are independent and do not induce direct coupling between different species, we keep them explicit until the end of the calculation. At that stage, the entries  $D_{ii}$  will be encoded as an effective quenched randomness, distributed according to the prescribed log-normal law.

### 3.3 Generating Functional analysis

We now perform a generating functional analysis in order to derive a dynamical mean-field theory (DMFT) for the generalized Lotka–Volterra dynamics defined in Eq. (43). Throughout this section the number of species is denoted by  $S$ , and we work in the thermodynamic limit  $S \rightarrow \infty$ .

#### 3.3.1 Definition of the generating functional

We consider connectivity  $C = 1$  for this analysis. For a given realization of the quenched disorder  $D$  and  $Z$ , we introduce the Martin–Siggia–Rose–Janssen–De Dominicis (MSRJD) generating functional

$$Z[\mathbf{j}] = \int \mathcal{D}D \mathcal{P}(D) \int \mathcal{D}[\mathbf{x}, \hat{\mathbf{x}}] \int \mathcal{D}Z \mathcal{P}(Z) \exp \left( iS_{\text{MSR}}[\mathbf{x}, \hat{\mathbf{x}}; D, Z] + i \sum_i \int dt j_i(t) x_i(t) \right), \quad (58)$$

where  $j_i(t)$  are source fields for the abundances and

$$S_{\text{MSR}} = \sum_i \int dt \hat{x}_i(t) \left[ \frac{\dot{x}_i(t)}{x_i(t)} - \left( 1 + \sum_j A_{ij} x_j(t) \right) \right]. \quad (59)$$

Here  $A_{ij}$  is the interaction matrix defined in the previous subsection,

$$A_{ij} = \begin{cases} D_{ii}, & i = j, \\ -\sigma D_{jj} G_{ij}, & i \neq j, \end{cases} \quad (60)$$

with  $G_{ij} = Z_{ij} - \frac{1}{S} \sum_k Z_{ik}$ .

It is convenient to separate the different contributions in the action:

$$S_{\text{MSR}} = \sum_i \int dt \hat{x}_i(t) \left[ \frac{\dot{x}_i(t)}{x_i(t)} - 1 \right] - \sum_{ij} \int dt \hat{x}_i(t) A_{ij} x_j(t) \quad (61)$$

$$= \sum_i \int dt \hat{x}_i(t) \left[ \frac{\dot{x}_i(t)}{x_i(t)} - 1 \right] - \sum_i \int dt \hat{x}_i(t) D_{ii} x_i(t) - \sigma \sum_{i \neq j} \int dt \hat{x}_i(t) D_{jj} G_{ij} x_j(t). \quad (62)$$

Introducing the shorthand

$$R_{ij} \equiv \int dt \hat{x}_i(t) x_j(t), \quad (63)$$

we can rewrite

$$S_{\text{MSR}} = \sum_i \int dt \hat{x}_i(t) \left[ \frac{\dot{x}_i(t)}{x_i(t)} - 1 \right] - \sum_i D_{ii} R_{ii} - \sigma \sum_{i \neq j} D_{jj} G_{ij} R_{ij}. \quad (64)$$

Thus the generating functional takes the form

$$Z[\mathbf{j}] = \int \mathcal{D}D \mathcal{P}(D) \int \mathcal{D}[\mathbf{x}, \hat{\mathbf{x}}] \int \mathcal{D}Z \mathcal{P}(Z) \exp \left\{ i \sum_i \int dt j_i(t) x_i(t) \right. \quad (65)$$

$$\left. + i \sum_i \int dt \hat{x}_i(t) \left[ \frac{\dot{x}_i(t)}{x_i(t)} - 1 \right] - i \sum_i D_{ii} R_{ii} - i \sigma \sum_{i \neq j} D_{jj} G_{ij} R_{ij} \right\}. \quad (66)$$

### 3.3.2 Disorder average over the Gaussian weights $Z$

We now average over the Gaussian weights  $Z_{ij}$ , drawn independently as

$$Z_{ij} \sim \mathcal{N}\left(0, \frac{1}{S}\right). \quad (67)$$

Using the definition

$$G_{ij} = Z_{ij} - \frac{1}{S} \sum_k Z_{ik}, \quad (68)$$

we write the interaction term as

$$-i\sigma \sum_{i \neq j} D_{jj} G_{ij} R_{ij} = -i\sigma \sum_{i \neq j} D_{jj} Z_{ij} R_{ij} + i \frac{\sigma}{S} \sum_{i \neq j} \sum_k D_{jj} Z_{ik} R_{ij}. \quad (69)$$

In the second term we relabel the dummy indices  $(j, k)$  and reorganize the sums so that both contributions take the form of a linear coupling to  $Z_{ij}$ . More explicitly,

$$-i\sigma \sum_{i \neq j} D_{jj} G_{ij} R_{ij} = -i\sigma \sum_{i \neq j} D_{jj} R_{ij} Z_{ij} + i \frac{\sigma}{S} \sum_{i \neq k} \sum_{j \neq i} D_{kk} R_{ik} Z_{ij} \quad (70)$$

$$= - \sum_{i \neq j} H_{ij} Z_{ij}, \quad (71)$$

where we have defined the (in general complex) coefficients

$$H_{ij} \equiv i\sigma \left[ D_{jj} R_{ij} - \frac{1}{S} \sum_k D_{kk} R_{ik} \right]. \quad (72)$$

The part of the action depending on  $Z_{ij}$  is therefore

$$S_Z = - \sum_{i \neq j} H_{ij} Z_{ij}. \quad (73)$$

The Gaussian average over  $Z$  is straightforward:

$$\left\langle \exp \left( - \sum_{i \neq j} H_{ij} Z_{ij} \right) \right\rangle_Z = \prod_{i \neq j} \int dZ_{ij} \sqrt{\frac{S}{2\pi}} \exp \left( - \frac{S}{2} Z_{ij}^2 - H_{ij} Z_{ij} \right) \quad (74)$$

$$\propto \exp \left( \frac{1}{2S} \sum_{i \neq j} H_{ij}^2 \right). \quad (75)$$

Substituting (72), we note that  $H_{ij} \propto i\sigma$ , so that

$$H_{ij}^2 = (i\sigma)^2 [\dots]^2 = -\sigma^2 [\dots]^2, \quad (76)$$

and the exponential becomes

$$\left\langle \exp \left( - \sum_{i \neq j} H_{ij} Z_{ij} \right) \right\rangle_Z \propto \exp \left( - \frac{\sigma^2}{2S} \sum_{i \neq j} \left[ D_{jj} R_{ij} - \frac{1}{S} \sum_k D_{kk} R_{ik} \right]^2 \right). \quad (77)$$

Using this result in Eq. (66), the disorder-averaged generating functional over  $Z$  reads

$$\begin{aligned} \langle Z[j] \rangle_Z = & \int \mathcal{D}D \mathcal{P}(D) \int \mathcal{D}[\underline{x}, \dot{\underline{x}}] \int \exp \left\{ i \sum_i \int dt j_i(t) x_i(t) \right. \\ & + i \sum_i \int dt \hat{x}_i(t) \left[ \frac{\dot{x}_i(t)}{x_i(t)} - 1 \right] - i \sum_i D_{ii} R_{ii} \\ & \left. - \frac{\sigma^2}{2S} \sum_{i \neq j} \left[ D_{jj} B_{ij} R_{ij} - \frac{1}{S} \sum_k D_{kk} B_{ij} R_{ik} \right]^2 \right\}. \end{aligned} \quad (78)$$

Expanding the square, one obtains

$$\begin{aligned}
& \sum_{i \neq j} \left[ D_{jj} R_{ij} - \frac{1}{S} \sum_k D_{kk} R_{ik} \right]^2 \\
&= \sum_{i \neq j} D_{jj}^2 R_{ij}^2 - \frac{2}{S} \sum_{i \neq j} \sum_k D_{jj} D_{kk} R_{ij} R_{ik} \\
&+ \frac{1}{S^2} \sum_{i \neq j} \sum_{k_1 \neq j} \sum_{k_2 \neq j} D_{k_1 k_1} D_{k_2 k_2} R_{ik_1} R_{ik_2}.
\end{aligned} \tag{79}$$

### 3.3.3 Macroscopic order parameters

Guided by the structure of the terms appearing after the disorder average, we introduce the following order parameters:

$$M(t) = \frac{1}{S} \sum_i D_{ii} x_i(t), \tag{80}$$

$$C_D(t, t') = \frac{1}{S} \sum_i D_{ii}^2 x_i(t) x_i(t'), \tag{81}$$

$$L(t, t') = \frac{1}{S} \sum_i \hat{x}_i(t) \hat{x}_i(t'). \tag{82}$$

The object  $M(t)$  is a disorder-weighted mean abundance,  $C_D(t, t')$  is a disorder-weighted two-time correlation function, and  $L(t, t')$  encodes correlations between response fields.

After some algebra (reorganizing the sums over species indices and keeping only terms that scale as  $\mathcal{O}(S)$ ), the exponent in (78) can be written as

$$\begin{aligned}
& i \sum_i \int dt \hat{x}_i(t) \left[ \frac{\dot{x}_i(t)}{x_i(t)} - 1 \right] - i \sum_i D_{ii} R_{ii} \\
& - \frac{\sigma^2}{2} \int dt dt' \left\{ S \left( 1 - \frac{1}{S} \right)^2 C_D(t, t') L(t, t') - 2(S-1)M(t)M(t')L(t, t') \right. \\
& \left. + M(t)M(t')L(t, t') + \frac{1}{S} C_D(t, t') L(t, t') + \mathcal{O}\left(\frac{1}{S}\right) \right\}.
\end{aligned} \tag{83}$$

In the thermodynamic limit  $S \rightarrow \infty$ , keeping the leading  $\mathcal{O}(S)$  terms and defining the connected correlator

$$\tilde{C}(t, t') = C_D(t, t') - M(t)M(t'), \tag{84}$$

this simplifies to

$$i \sum_i \int dt \hat{x}_i(t) \left[ \frac{\dot{x}_i(t)}{x_i(t)} - 1 \right] - i \sum_i D_{ii} R_{ii} - S \frac{\sigma^2}{2} \int dt dt' \tilde{C}(t, t') L(t, t') + \mathcal{O}(1). \tag{85}$$

Therefore, up to subleading corrections in  $S$ , the disorder-averaged generating functional can be written as

$$\begin{aligned}
\langle Z[\mathbf{j}] \rangle_{B,Z} = & \int \mathcal{D}D \mathcal{P}(D) \int \mathcal{D}[\mathbf{x}, \hat{\mathbf{x}}] \exp \left\{ i \sum_i \int dt j_i(t) x_i(t) \right. \\
& + i \sum_i \int dt \hat{x}_i(t) \left[ \frac{\dot{x}_i(t)}{x_i(t)} - 1 + D_{ii} x_i(t) \right] \\
& \left. - S \frac{\sigma^2}{2} \int dt dt' \tilde{C}(t, t') L(t, t') + \mathcal{O}(1) \right\}.
\end{aligned} \tag{86}$$

To treat the order parameters at the saddle point level, we enforce their definitions via functional delta constraints. For  $M(t)$ ,

$$1 = \int \mathcal{D}\underline{M} \delta \left( M(t) - \frac{1}{S} \sum_i D_{ii} x_i(t) \right) \quad (87)$$

$$= \int \mathcal{D}[\hat{M}, \underline{M}] \exp \left( iS \int dt \hat{M}(t) \left[ M(t) - \frac{1}{S} \sum_i D_{ii} x_i(t) \right] \right). \quad (88)$$

Similarly, for  $C_D(t, t')$ ,

$$\begin{aligned} 1 &= \int \mathcal{D}\underline{C_D} \delta \left( C_D(t, t') - \frac{1}{S} \sum_i D_{ii}^2 x_i(t) x_i(t') \right) \\ &= \int \mathcal{D}[\hat{C}, \underline{C_D}] \exp \left( iS \int dt dt' \hat{C}(t, t') \left[ C_D(t, t') - \frac{1}{S} \sum_i D_{ii}^2 x_i(t) x_i(t') \right] \right), \end{aligned} \quad (89)$$

and for  $L(t, t')$ ,

$$\begin{aligned} 1 &= \int \mathcal{D}\underline{L} \delta \left( L(t, t') - \frac{1}{S} \sum_i \hat{x}_i(t) \hat{x}_i(t') \right) \\ &= \int \mathcal{D}[\hat{L}, \underline{L}] \exp \left( iS \int dt dt' \hat{L}(t, t') \left[ L(t, t') - \frac{1}{S} \sum_i \hat{x}_i(t) \hat{x}_i(t') \right] \right). \end{aligned} \quad (90)$$

Here, by  $\mathcal{D}[\hat{\mathcal{N}}, \underline{\mathcal{N}}]$  we denote a functional measure over fields of two time arguments,

$$\mathcal{D}[\hat{\mathcal{N}}, \underline{\mathcal{N}}] = \prod_{t, t'} \frac{d\hat{\mathcal{N}}(t, t') d\mathcal{N}(t, t')}{2\pi/S}, \quad (91)$$

and similarly for fields of a single time argument.

Inserting the identities (88)–(90) into Eq. (86) we obtain a functional integral of the form

$$\langle Z[\mathbf{j}] \rangle = \int \mathcal{D}[\hat{M}, M] \mathcal{D}[\hat{C}, C_D] \mathcal{D}[\hat{L}, L] \exp \left( S \mathcal{Q}[M, \hat{M}, C_D, \hat{C}, L, \hat{L}] + \mathcal{O}(1) \right), \quad (92)$$

where the functional  $\mathcal{Q}$  naturally splits into three contributions,

$$\mathcal{Q} = \Psi + \Phi + \Omega. \quad (93)$$

**(i) Conjugate-order-parameter part  $\Psi$ .** The first contribution collects the direct products of order parameters and their conjugates:

$$\Psi = i \int dt \hat{M}(t) M(t) + i \int dt dt' [\hat{C}(t, t') C_D(t, t') + \hat{L}(t, t') L(t, t')]. \quad (94)$$

**(ii) Variance term  $\Phi$ .** The second contribution originates from the variance term proportional to  $\tilde{C}(t, t') L(t, t')$  in Eq. (86):

$$\Phi = -\frac{\sigma^2}{2} \int dt dt' L(t, t') \tilde{C}(t, t'). \quad (95)$$

**(iii) Single-species contribution  $\Omega$ .** Finally, the third term  $\Omega$  results from the remaining path integral over the microscopic dynamics of each species, which factorizes over  $i$  in the thermodynamic limit:

$$\begin{aligned} \Omega = \frac{1}{S} \sum_i \log \int \mathcal{D}\underline{x}_i \mathcal{D}\hat{\underline{x}}_i p_i(x_i(0)) & \exp \left( i \int dt j_i(t) x_i(t) + i \int dt \hat{j}_i(t) \hat{x}_i(t) \right) \\ & \times \exp \left( i \int dt \hat{x}_i(t) \left[ \frac{\dot{x}_i(t)}{x_i(t)} - (1 - D_{ii}x_i(t)) \right] \right) \\ & \times \exp \left( -i \int dt \hat{M}(t) D_{ii} x_i(t) \right) \\ & \times \exp \left( -i \int dt dt' \left[ \hat{C}_D(t, t') D_{ii}^2 x_i(t) x_i(t') + \hat{L}(t, t') \hat{x}_i(t) \hat{x}_i(t') \right] \right). \end{aligned} \quad (96)$$

Here  $p_i(x_i(0))$  denotes the initial condition of species  $i$ , and we have assumed a factorized initial distribution over species,  $p_0(\underline{x}(0)) = \prod_i p_i(x_i(0))$ .

The crucial point is that each of the three functionals  $\Psi$ ,  $\Phi$  and  $\Omega$  contains contributions of at least order  $\mathcal{O}(S^0)$  in the thermodynamic limit. Therefore the leading behaviour of  $\langle Z \rangle$  is controlled by the saddle point of  $\mathcal{Q}$ .

### 3.3.4 Saddle-point equations and interpretation of $\Omega$

We now find the saddle point by taking functional derivatives of  $\mathcal{Q}$  with respect to the order parameters and their conjugates, and setting them to zero. This yields a set of self-consistency relations.

From variations with respect to the “non-hatted” order parameters we obtain:

$$\frac{\delta \mathcal{Q}}{\delta \hat{M}(t)} = 0 \quad \Rightarrow \quad \hat{M}(t) = 2 \int dt' M(t') L(t, t'), \quad (97)$$

$$\frac{\delta \mathcal{Q}}{\delta C_D(t, t')} = 0 \quad \Rightarrow \quad i \hat{C}(t, t') = \frac{\sigma^2}{2} L(t, t'), \quad (98)$$

$$\frac{\delta \mathcal{Q}}{\delta L(t, t')} = 0 \quad \Rightarrow \quad i \hat{L}(t, t') = \frac{\sigma^2}{2} \hat{C}(t, t'). \quad (99)$$

On the other hand, variations with respect to the conjugate fields yield:

$$\frac{\delta \mathcal{Q}}{\delta \hat{M}(t)} = 0 \quad \Rightarrow \quad M(t) = - \lim_{S \rightarrow \infty} \frac{\delta \Omega}{\delta \hat{M}(t)}, \quad (100)$$

$$\frac{\delta \mathcal{Q}}{\delta \hat{C}(t, t')} = 0 \quad \Rightarrow \quad C(t, t') = - \lim_{S \rightarrow \infty} \frac{\delta \Omega}{\delta \hat{C}(t, t')}, \quad (101)$$

$$\frac{\delta \mathcal{Q}}{\delta \hat{L}(t, t')} = 0 \quad \Rightarrow \quad L(t, t') = - \lim_{S \rightarrow \infty} \frac{\delta \Omega}{\delta \hat{L}(t, t')}. \quad (102)$$

Equations (97)–(102) show that the conjugate fields  $\hat{M}$ ,  $\hat{C}$  and  $\hat{L}$  play a role analogous to source fields for the macroscopic order parameters, with  $\Omega$  acting as an effective “free-energy” functional at the level of single-species trajectories.

Using the saddle-point relations (97)–(99) and the definitions of the order parameters (80)–(82), we can write  $\Omega$  as

$$\Omega = \frac{1}{S} \sum_i \log Z_{\text{eff}}^{(i)}[\underline{j}_i, \hat{\underline{j}}_i], \quad (103)$$

where the effective single-species generating functional is

$$\begin{aligned} Z_{\text{eff}}^{(i)}[\underline{j}_i, \hat{\underline{j}}_i] &= \int \mathcal{D}\underline{x}_i \mathcal{D}\hat{\underline{x}}_i p_i(x_i(0)) \exp \left( i \int dt \hat{x}_i(t) \left[ \frac{\dot{x}_i(t)}{x_i(t)} - (1 - D_{ii}x_i(t)) \right] \right) \\ &\quad \times \exp \left( i \int dt D_{ii}j_i(t)x_i(t) + i \int dt \hat{j}_i(t)\hat{x}_i(t) - i \int dt M(t)\hat{x}_i(t) \right) \\ &\quad \times \exp \left( -\frac{\sigma^2}{2} \int dt dt' \left[ L(t, t')x_i(t)x_i(t') + \tilde{C}(t, t')\hat{x}_i(t)\hat{x}_i(t') \right] \right). \end{aligned} \quad (104)$$

This expression shows clearly how the effective single-species process is coupled to the macroscopic order parameters.

### 3.3.5 Vanishing of pure response correlators and self-consistent order parameters

The response sources  $\hat{j}_i(t)$  have been introduced so that derivatives of  $\langle Z \rangle$  with respect to  $\hat{j}$  generate moments of the response fields  $\hat{x}_i(t)$ . However, physical averages contain only the  $x_i(t)$ ; moments involving only response fields are purely auxiliary and, for a properly normalized generating functional, must vanish.

Indeed, imposing that the disorder-averaged generating functional is normalized for all  $\hat{\mathbf{j}}$ ,

$$\overline{Z[\mathbf{0}, \hat{\mathbf{j}}]} = 1, \quad (105)$$

implies that

$$\langle \hat{x}_i(t_1) \cdots \hat{x}_i(t_n) \rangle_i = (-i)^n \frac{\delta^n}{\delta \hat{j}_i(t_1) \cdots \delta \hat{j}_i(t_n)} \overline{Z[\mathbf{0}, \hat{\mathbf{j}}]} \Big|_{\hat{\mathbf{j}}=0} = 0 \quad (106)$$

for any  $n \geq 1$ . In particular,

$$L(t, t') = \frac{1}{S} \sum_i \langle \hat{x}_i(t)\hat{x}_i(t') \rangle_i = 0. \quad (107)$$

Thus the saddle-point solution has  $L = 0$ , but from (99) the conjugate field  $\hat{L}$  remains finite and encodes the noise kernel through  $\tilde{C}(t, t')$ .

Using the effective generating functional (104), the order parameters can be expressed as averages over the effective process:

$$M(t) = \lim_{S \rightarrow \infty} \frac{1}{S} \sum_i \langle D_{ii}x_i(t) \rangle_i, \quad (108)$$

$$C(t, t') = \lim_{S \rightarrow \infty} \frac{1}{S} \sum_i \langle D_{ii}^2 x_i(t)x_i(t') \rangle_i, \quad (109)$$

$$L(t, t') = \lim_{S \rightarrow \infty} \frac{1}{S} \sum_i \langle \hat{x}_i(t)\hat{x}_i(t') \rangle_i = 0. \quad (110)$$

Here  $\langle \cdot \rangle_i$  denotes an average with respect to  $Z_{\text{eff}}^{(i)}$ .

Equivalently, we can express these quantities as derivatives of  $\Omega$  with respect to the sources:

$$-i \frac{\delta \Omega}{\delta j_i(t)} \Big|_{\mathbf{j}=\mathbf{0}} = M(t), \quad (111)$$

$$-\frac{\delta^2 \Omega}{\delta j_i(t) \delta j_i(t')} \Big|_{\mathbf{j}=\mathbf{0}} = C(t, t') - M(t)M(t'), \quad (112)$$

$$-\frac{\delta^2 \Omega}{\delta \hat{j}_i(t) \delta \hat{j}_i(t')} \Big|_{\mathbf{j}=\mathbf{0}} = L(t, t') = 0. \quad (113)$$

### 3.3.6 Effective single-species process

After integrating out the degrees of freedom and enforcing the saddle-point conditions, the microscopic dynamics of different species become statistically independent. The macroscopic behaviour is fully encoded in the order parameters  $M$  and  $\tilde{C}$ , while the index  $i$  becomes irrelevant in the thermodynamic limit. We can therefore define an effective process for a representative species, with measure

$$\begin{aligned} \mathcal{M}[x, \hat{x}] &= p_0(x(0)) \exp \left( i \int dt \hat{x}(t) \left[ \frac{\dot{x}(t)}{x(t)} - (1 - Dx(t)) + \hat{j}(t) \right] \right) \\ &\times \exp \left( -\frac{\sigma^2}{2} \int dt dt' \tilde{C}(t, t') \hat{x}(t) \hat{x}(t') \right), \end{aligned} \quad (114)$$

where  $D$  is now a single random variable sampled from the log-normal distribution  $\mathcal{P}(D)$  (the distribution of diagonal elements  $D_{ii}$ ). Expectation values with respect to the effective process are defined as

$$\langle f[\underline{x}, \hat{\underline{x}}] \rangle_* = \frac{\int \mathcal{D}\underline{x} \mathcal{D}\hat{\underline{x}} f[\underline{x}, \hat{\underline{x}}] \mathcal{M}[\underline{x}, \hat{\underline{x}}]}{\int \mathcal{D}\underline{x} \mathcal{D}\hat{\underline{x}} \mathcal{M}[\underline{x}, \hat{\underline{x}}]}. \quad (115)$$

By performing a Hubbard–Stratonovich transformation, the quadratic term in  $\hat{x}$  can be written as an average over a Gaussian noise  $\eta(t)$  with

$$\mathbb{E}[\eta(t)] = 0, \quad \mathbb{E}[\eta(t)\eta(t')] = \sigma^2 \tilde{C}(t, t'). \quad (116)$$

Equivalently, we can write the effective measure as

$$\mathcal{M}[x, \hat{x}] \propto \left\langle \exp \left( i \int dt \hat{x}(t) \left[ \frac{\dot{x}(t)}{x(t)} - (1 - Dx(t)) - \eta(t) + \hat{j}(t) \right] \right) \right\rangle_{\eta}, \quad (117)$$

where the average is over realizations of  $\eta$ . The self-consistency conditions take the form

$$M(t) = \langle Dx(t) \rangle_*, \quad (118)$$

$$\sigma^2 \tilde{C}(t, t') = \sigma^2 (\langle D^2 x(t)x(t') \rangle_* - \langle Dx(t) \rangle_* \langle Dx(t') \rangle_*) = \langle \eta(t)\eta(t') \rangle_*. \quad (119)$$

Finally, (117) shows that the effective dynamics of a representative species is governed by the one-dimensional stochastic differential equation

$$\dot{x}(t) = x(t) \left[ 1 - Dx(t) + \eta(t) + \hat{j}(t) + \xi(t) \right], \quad (120)$$

where  $\xi(t)$  denotes the original environmental noise (if present) and  $\eta(t)$  is the emergent, self-consistent noise generated by the random interactions. The parameter  $D$  is a quenched random variable drawn from the prescribed log-normal distribution of intrinsic rates.

We rename  $x \rightarrow Dx$  such that we can write the effective process as follows

$$\dot{x}(t) = x(t) \left[ 1 - x(t) + \eta(t) + \hat{j}(t) + \xi(t) \right], \quad (121)$$

which is a random Generalized Lotka–Volterra effective process with temporal correlations of the effective noise given by  $\langle \eta(t)\eta(t') \rangle_* = \sigma^2 (\langle x(t)x(t') \rangle_* - \langle x(t) \rangle_* \langle x(t') \rangle_*)$

## 3.4 Static phase: self-consistent fixed-point distribution

In the stable phase the DMFT effective process for a representative species

$$\dot{x}(t) = x(t) [1 - x(t) + \eta(t)], \quad (122)$$

where  $\eta(t)$  is an effective Gaussian noise with zero mean and two time correlations

$$\langle \eta(t)\eta(t') \rangle = \sigma^2 \tilde{C}(t, t'). \quad (123)$$

relax to a stationary distribution. In the static phase, trajectories for single realizations converge to a fixed point and the effective noise becomes static,

$$\eta(t) \equiv \eta^* = \sigma \sqrt{q - M^2} z, \quad z \sim \mathcal{N}(0, 1), \quad (124)$$

Here and in the following,  $\langle \cdot \rangle$  denotes an average over species and disorder in the thermodynamic limit. For a fixed realization of  $z$ , the stationary condition  $\dot{x} = 0$  applied to (122) gives

$$x^*(z) \left[ 1 - x^*(z) + \eta^*(z) \right] = 0. \quad (125)$$

Besides the absorbing solution  $x^*(z) = 0$ , a positive fixed point exists whenever

$$1 - x^*(z) + \eta^*(z) = 0, \quad (126)$$

i.e.

$$x^*(z) = 1 + \eta^*(z) = 1 + \sigma \sqrt{q - M^2} z. \quad (127)$$

It is convenient to parameterize the noise amplitude in terms of a dimensionless parameter

$$\Delta \equiv \frac{1}{\sigma \sqrt{q - M^2}}. \quad (128)$$

Then we can write

$$x^*(z) = \left( 1 + \frac{z}{\Delta} \right) = \frac{\Delta + z}{\Delta}. \quad (129)$$

The positivity constraint  $x^*(z) > 0$  implies

$$1 + \frac{z}{\Delta} > 0 \iff z > -\Delta. \quad (130)$$

Therefore, only those realizations of the static noise with  $z > -\Delta$  correspond to surviving species; those with  $z \leq -\Delta$  fall into the absorbing state  $x^* = 0$ .

Let us obtain the distribution of  $x^*$  induced by the Gaussian variable  $z \sim \mathcal{N}(0, 1)$ . Denote the standard normal measure by

$$\mathcal{D}z = \frac{dz}{\sqrt{2\pi}} e^{-z^2/2}. \quad (131)$$

For a given  $D > 0$  we define the following local moments of the stationary abundance:

$$\phi = \int_{-\Delta}^{\infty} \mathcal{D}z, \quad (132)$$

$$M = \int_{-\Delta}^{\infty} \mathcal{D}z x^*(z), \quad (133)$$

$$q = \int_{-\Delta}^{\infty} \mathcal{D}z [x^*(z)]^2. \quad (134)$$

Here  $\phi$  is the survival probability (the fraction of species with  $x^* > 0$ ), while  $M$  and  $q$  are the first and second unweighted moments of  $x^*$  among surviving species (unconditional on extinction, i.e. zero contribution for extinct ones).

Using (129), these integrals can be evaluated in closed form. Introduce the standard Gaussian pdf and cdf

$$a_1(\Delta) = \frac{1}{\sqrt{2\pi}} e^{-\Delta^2/2}, \quad a_0(\Delta) = \int_{-\infty}^{\Delta} \mathcal{D}z = \frac{1}{2} \left[ 1 + \text{erf} \left( \frac{\Delta}{\sqrt{2}} \right) \right]. \quad (135)$$

Then

$$\phi = \int_{-\Delta}^{\infty} \mathcal{D}z = a_0(\Delta). \quad (136)$$

For the first moment we obtain

$$M = \int_{-\Delta}^{\infty} \mathcal{D}z \frac{\Delta + z}{\Delta} \quad (137)$$

$$= \frac{1}{\Delta} \left[ \int_{-\Delta}^{\infty} \mathcal{D}z z + \Delta \int_{-\Delta}^{\infty} \mathcal{D}z \right] \equiv \Delta^{-1} w_1. \quad (138)$$

Using the standard Gaussian identities we find

$$\int_{-\Delta}^{\infty} \mathcal{D}z = a_0(\Delta), \quad \int_{-\Delta}^{\infty} \mathcal{D}z z = a_1(\Delta). \quad (139)$$

Therefore

$$M = \Delta^{-1} (a_0(\Delta) + \Delta a_1(\Delta)). \quad (140)$$

For the second moment we proceed analogously:

$$q = \int_{-\Delta}^{\infty} \mathcal{D}z \left( \frac{\Delta + z}{\Delta} \right)^2 = \frac{1}{\Delta^2} \int_{-\Delta}^{\infty} \mathcal{D}z (z^2 + 2\Delta z + \Delta^2). \quad (141)$$

The remaining Gaussian integrals are

$$\int_{-\Delta}^{\infty} \mathcal{D}z z^2 = a_0(\Delta) - \Delta a_1(\Delta). \quad (142)$$

Combining everything,

$$\int_{-\Delta}^{\infty} \mathcal{D}z (z^2 + 2\Delta z + \Delta^2) = [a_0(\Delta) - \Delta a_1(\Delta)] + 2\Delta a_1(\Delta) + \Delta^2 a_0(\Delta) \quad (143)$$

$$= (1 + \Delta^2) a_0(\Delta) + \Delta a_1(\Delta). \quad (144)$$

Hence

$$q = \Delta^{-2} [(1 + \Delta^2) a_0(\Delta) + \Delta a_1(\Delta)] \equiv \Delta^{-2} w_2. \quad (145)$$

Equations (136), (140) and (145) express the survival fraction and the first two moments of the abundance fixed point for a given  $D$  in terms of the single dimensionless parameter  $\Delta$  and the error function. All together

$$\phi = a_0(\Delta) \quad (146)$$

$$M = \sigma \sqrt{q - M^2} (a_1(\Delta) + \Delta a_0(\Delta)) \equiv \sigma \sqrt{q - M^2} w_1 \quad (147)$$

$$q = \sigma^2 (q - M^2) [(1 + \Delta^2) a_0(\Delta) + \Delta a_1(\Delta)] \equiv \sigma^2 (q - M^2) w_2 \quad (148)$$

which is a closed system of equations.

We want to show that in the stable phase the unique possible solutions that have finite abundance are restricted by the condition  $\Delta^{-1} = 0$ . This implies  $q = M^2$  and  $\phi = 1$  for  $\sigma > 0$ .

Subtracting the square of (147) from (148) leads to the condition

$$(q - M^2) [1 - \sigma^2 (w_2 - w_1^2)] = 0 \quad (149)$$

Assume that  $q > M^2$  and  $1 = \sigma^2 (w_2 - w_1^2)$ , where  $w_2, w_1$  are functions of  $\Delta \geq 0$ . However, for  $\sigma < 1$  the function  $g(\Delta) = w_2(\Delta) - w_1(\Delta)^2 - \frac{1}{\sigma^2}$  does not cross the x-axis; for  $\sigma = 1$  it tends to zero when  $\Delta \rightarrow \infty$ ; and for  $\sigma > 1$  it has a finite  $\Delta > 0$  where it crosses. This means that for  $\sigma \leq 1$  the stable phase is characterized by the solution  $q - M^2 = 0$  in Eq. 149, and whenever  $\sigma > 1$  there exists a solution where  $\infty > \sigma \Delta^{-1} = q - M^2 > 0$ . We show in the next section, the regime where  $\sigma > 1$  is already unstable. This leaves us with the unique choice  $\sigma < 1$  that characterizes the stable phase. Then, in all this phase it is verified that  $\Delta^{-1} = 0$ , which implies that  $q = M^2$  and the effective noise vanishes. Thus, the zero row-sum property of the interaction matrix  $M$  implies that the effective noise vanishes in the thermodynamic limit, which, as desired, keeps the fixed points to be the inverse of the log-normal diagonal matrix  $D$ .

### 3.5 Grilli's laws in the stable phase

As shown in the previous section, the stable phase is characterized by the condition  $\Delta^{-1} = 0$ . Now, we add the environmental noise to the equation. For a small amplitude of the noise, the effect of it is that trajectories would fluctuate around fixed point solutions. Then condition  $\Delta^{-1} = 0$  still holds at first order approximation, this makes the effective process to be the following stochastic differential equation with multiplicative noise

$$\dot{x}(t) = x(t) (1 - x(t) + \sigma_0 \xi(t)) \quad (150)$$

where  $\xi(t)$  is white noise with variance  $\sigma_0^2$ . That is, the original interacting dynamics reduces in the thermodynamic limit due to the zero row-sum property to a decoupled single stochastic differential equation, encapsulating Grilli's decoupled logistic model and its consequent Grilli's laws for microbial communities. However, our model is dynamically richer: when the effective noise does not vanish, the model is able to exhibit chaotic behavior, a property that the decoupled model does not have.

### 3.6 Stability Analysis

The next step is to deduce the combination of parameters for the instability line: the line that delimits when the dynamics goes from the stable phase to the chaotic phase.

Let us assume that we run the dynamics and the system relaxes towards the static solution  $(x^*, \eta^*)$ , then we introduce a small perturbation and quantify if it decays towards the fixed point solution or not.

$$\dot{x} = x (1 - x + \eta + \epsilon \xi) \quad (151)$$

where  $\epsilon$  is the small parameter that controls the intensity of the perturbation and  $\xi$  is a white noise with unit variance and zero mean. That is, we define time dependent variables around the fixed point solution at order  $\epsilon$

$$\eta(t) = \eta^* + \epsilon \nu(t) \quad (152)$$

$$x(t) = x^* + \epsilon y(t) \quad (153)$$

Linearizing the dynamics, we obtain

$$O(\epsilon^0) : \quad x^* (1 - x^* + \eta^*) = 0 \quad (154)$$

$$O(\epsilon) : \quad \dot{y} = x^* (-y + \nu + \xi) + y (1 - x^* + \eta^*). \quad (155)$$

In the stable phase, we know that we reach feasible solutions characterized by  $x^* \neq 0$ , then  $1 - x^* + \eta^* = 0$  and the previous relation at order  $\epsilon$  reduces to the equation

$$\dot{y} = x^* (-y + \nu + \xi). \quad (156)$$

In Fourier space, we can write the first order differential equation as follows

$$\frac{i\omega}{x^*} \tilde{y}(\omega) = -\tilde{y}(\omega) + \tilde{\nu}(\omega) + \tilde{\xi}(\omega) \quad (157)$$

where we denoted by tilded terms the corresponding Fourier transforms.

We need relations between the moments of the dynamic variable  $y$  and the effective noise  $\nu$ . Recurring to the self-consistent relations we obtain the following

$$\langle \eta(t) \eta(t') \rangle = \langle \eta^* \eta^* \rangle + \epsilon (\langle \eta^* \nu(t) \rangle + \langle \eta^* \nu(t') \rangle) + \epsilon^2 \langle \nu(t) \nu(t') \rangle \quad (158)$$

$$\langle x(t) x(t') \rangle = q + \epsilon (\langle x^* y(t') \rangle + \langle x^* y(t) \rangle) + \epsilon^2 \langle y(t) y(t') \rangle \quad (159)$$

both are linked by the relation

$$\langle \eta(t)\eta(t') \rangle = \sigma^2 [\langle x(t)x(t') \rangle - \langle x(t) \rangle \langle x(t') \rangle] \quad (160)$$

where averages are taken with respect to the static distribution and the effective process  $\nu$  after the perturbation applied. Then

$$O(\epsilon^0) : \langle \eta^* \eta^* \rangle = \sigma^2 (q - M^2) \quad (161)$$

$$O(\epsilon) : \langle \eta^* \nu(t) \rangle + \langle \eta^* \nu(t') \rangle = \sigma^2 [\langle x^* y(t') \rangle - \langle x^* \rangle \langle y(t') \rangle + \langle x^* y(t) \rangle - \langle x^* \rangle \langle y(t) \rangle] \quad (162)$$

$$O(\epsilon^2) : \langle \nu(t) \nu(t') \rangle = \sigma^2 (\langle y(t) y(t') \rangle - \langle y(t) \rangle \langle y(t') \rangle) \quad (163)$$

Computing  $\langle |\tilde{y}(\omega)|^2 \rangle$  from (157), taking averages, using the previous self-consistent relations, and evaluating at  $\omega = 0$  we obtain the following result

$$\langle |\tilde{y}(0)|^2 \rangle = \phi [\sigma^2 (\langle |\tilde{y}(0)|^2 \rangle - \langle |\tilde{y}(0)|^2 \rangle) + 1]. \quad (164)$$

From (157) we can directly take averages to show that  $\langle \tilde{y}(0) \rangle = 0$  since  $\langle \nu \rangle = \langle \xi \rangle = 0$ . Thus, clearing  $\langle |\tilde{y}(0)|^2 \rangle$  from (164), we get

$$\langle |\tilde{y}(0)|^2 \rangle = \frac{\phi}{1 - \phi \sigma^2}. \quad (165)$$

For  $1 - \phi \sigma^2 > 0$  the system is in the stable phase, whereas for  $1 - \phi \sigma^2 < 0$  the term  $\langle |\tilde{y}(0)|^2 \rangle < 0$  leads to an incongruence and therefore signals the unstable phase.

## 4 Inferring the distance to the edge of chaos

In the main text, we linked the distance to the edge of chaos to the width of the correlation histogram, following previous works [5]. Here, we give a simple derivation for this methodology.

### 4.1 The Ornstein-Uhlenbeck process

In section 1.2, we proved that the population dynamics could be expressed (in log-space and after linearization) as a set of linear stochastic differential equations, an Ornstein-Uhlenbeck process [6]. In vector form, this set of equations can be expressed as:

$$\partial_t \mathbf{x}(t) = -\frac{k}{\tau} (\mathbf{I} - \sigma \mathbf{G}) \mathbf{x}(t) + \sigma_0 \boldsymbol{\xi}(t), \quad (166)$$

where  $\mathbf{G} = M \cdot \text{diag}(x^*)$ , c.f (8). Define a new time variable

$$t' = \frac{k}{\tau} t \quad \Rightarrow \quad \partial_t = \frac{k}{\tau} \partial_{t'}. \quad (167)$$

In terms of  $t'$  the equation becomes

$$\frac{k}{\tau} \partial_{t'} \mathbf{x}(t') = -\frac{k}{\tau} (\mathbf{I} - \sigma \mathbf{G}) \mathbf{x}(t') + \sigma_0 \boldsymbol{\xi}(t'), \quad (168)$$

and dividing both sides by  $k/\tau$  we obtain

$$\partial_{t'} \mathbf{x}(t') = -(\mathbf{I} - \sigma \mathbf{G}) \mathbf{x}(t') + \frac{\tau}{k} \sigma_0 \boldsymbol{\xi}(t'). \quad (169)$$

We now introduce a rescaled noise

$$\boldsymbol{\eta}(t') \equiv \sqrt{\frac{\tau}{k}} \boldsymbol{\xi}(t'), \quad (170)$$

which satisfies

$$\langle \eta_i(t') \rangle = 0, \quad \langle \eta_i(t') \eta_j(s') \rangle = \delta_{ij} \delta(t' - s'). \quad (171)$$

In terms of  $\boldsymbol{\eta}$ , the dynamics reads

$$\partial_{t'} \mathbf{x}(t') = -(I - \sigma G) \mathbf{x}(t') + \sigma_0 \sqrt{\frac{\tau}{k}} \boldsymbol{\eta}(t'), \quad (172)$$

which is again an Ornstein–Uhlenbeck process, with an effective noise amplitude

$$D = \sigma_0^2 \frac{\tau}{k}. \quad (173)$$

In what follows, in order to make notation more compact, we drop the primes to denote the time dilation, and just focus on the set of linear dynamics:

$$\partial_t \mathbf{x}(t) = -(I - \sigma G) \mathbf{x}(t) + \sqrt{D} \boldsymbol{\xi}(t). \quad (174)$$

The aim of this section is to derive the Dynamic Mean-Field expression for this set of linear dynamics.

## 4.2 Change of basis to transversal and longitudinal modes

It is convenient to work in a basis that is aligned with the homogeneous direction (i.e., the vector  $\mathbf{1} = (1, \dots, 1)$ ). To this end, we introduce an orthogonal matrix  $U \in \mathbb{R}^{S \times S}$ ,

$$U^\top U = UU^\top = I, \quad (175)$$

whose first column coincides with the normalized homogeneous vector,

$$U_{i0} = \frac{1}{\sqrt{S}} \quad \text{for all } i = 1, \dots, S. \quad (176)$$

The remaining columns of  $U$  form an orthonormal basis of the subspace orthogonal to the homogeneous vector.

We then define the rotated variables

$$\mathbf{X}(t) = U^\top \mathbf{x}(t), \quad \boldsymbol{\xi}'(t) = U^\top \boldsymbol{\xi}(t), \quad G' = U^\top G U. \quad (177)$$

Because  $U$  is orthogonal, the transformed noise  $\boldsymbol{\xi}'(t)$  has the same statistics as  $\boldsymbol{\xi}(t)$ ,

$$\langle \xi'_a(t) \xi'_b(s) \rangle = \delta_{ab} \delta(t - s), \quad a, b = 0, \dots, S - 1. \quad (178)$$

Multiplying (174) on the left by  $U^\top$ , and using the definitions above, we obtain the dynamics in the rotated basis,

$$\partial_t \mathbf{X}(t) = -(I - \sigma G') \mathbf{X}(t) + D \boldsymbol{\xi}'(t), \quad (179)$$

or, in components,

$$\partial_t X_a(t) = -X_a(t) + \sigma \sum_{b=0}^{S-1} G'_{ab} X_b(t) + \sqrt{D} \xi'_a(t), \quad a = 0, \dots, S - 1. \quad (180)$$

Here  $a = 0$  labels the longitudinal (homogeneous) mode, while  $a = 1, \dots, S - 1$  label the transverse modes.

## 4.3 Moment generating functional for the linear dynamics

We now formulate the dynamics (179) within the Martin–Siggia–Rose–De Dominicis–Janssen (MSRDJ) path–integral formalism, which yields a generating functional of the form:

$$Z[\mathbf{j}, \tilde{\mathbf{j}}] = \int \mathcal{D}\mathbf{X} \mathcal{D}\tilde{\mathbf{X}} \exp \left( -S[\mathbf{X}, \tilde{\mathbf{X}}] + \sum_{a=0}^{S-1} \int dt [j_a(t) X_a(t) + \tilde{j}_a(t) \tilde{X}_a(t)] \right), \quad (181)$$

where the MSRDJ action  $S$  reads

$$S[\mathbf{X}, \tilde{\mathbf{X}}] = \sum_{a=0}^{S-1} \int dt \left[ \tilde{X}_a(t) \left( \partial_t X_a(t) + X_a(t) - \sigma \sum_{b=0}^{S-1} G'_{ab} X_b(t) \right) - \frac{D}{2} \tilde{X}_a(t)^2 \right]. \quad (182)$$

It is convenient to separate the bare (uncoupled) OU part of the action from the interaction mediated by  $G'$ . We write

$$S[\mathbf{X}, \tilde{\mathbf{X}}] = S_0[\mathbf{X}, \tilde{\mathbf{X}}] - S_{\text{int}}[\mathbf{X}, \tilde{\mathbf{X}}], \quad (183)$$

where

$$S_0[\mathbf{X}, \tilde{\mathbf{X}}] = \sum_{a=0}^{S-1} \int dt \left[ \tilde{X}_a(t) (\partial_t X_a(t) + X_a(t)) - \frac{D}{2} \tilde{X}_a(t)^2 \right], \quad (184)$$

and

$$S_{\text{int}}[\mathbf{X}, \tilde{\mathbf{X}}] = \sigma \sum_{a,b=0}^{S-1} \int dt \tilde{X}_a(t) G'_{ab} X_b(t). \quad (185)$$

The interaction term  $S_{\text{int}}$  contains the quenched disorder through the random matrix  $G'$ , while  $S_0$  describes  $S$  independent Ornstein–Uhlenbeck processes (one longitudinal and  $S - 1$  transverse modes) in the absence of coupling.

#### 4.4 Average over the quenched disorder

We now perform the average of the generating functional over the quenched disorder in the connectivity. The random matrix  $G$  is taken to have independent Gaussian entries with zero mean and variance  $\text{Var}(G_{ij}) = 1/S$ , together with the constraint  $G\mathbf{1} = 0$ , where  $\mathbf{1}$  is the homogeneous vector. In the rotated basis defined above, this constraint implies that the first column of  $G'$  vanishes,

$$G'_{a0} = 0 \quad \text{for all } a = 0, \dots, S-1, \quad (186)$$

while the remaining entries

$$G'_{\alpha\beta}, \quad G'_{0\beta}, \quad \alpha, \beta = 1, \dots, S-1, \quad (187)$$

are independent Gaussian random variables with

$$\langle G'_{ab} \rangle = 0, \quad \langle G'_{ab} G'_{cd} \rangle = \frac{1}{S} \delta_{ac} \delta_{bd}. \quad (188)$$

The disorder-averaged generating functional is defined as

$$\overline{Z[\mathbf{j}, \tilde{\mathbf{j}}]} = \int \mathcal{D}G' P(G') Z[\mathbf{j}, \tilde{\mathbf{j}} | G'], \quad (189)$$

where

$$P(G') \propto \exp \left[ -\frac{S}{2} \sum_{a,b=0}^{S-1} G'_{ab}^2 \right] \quad (190)$$

implements the Gaussian distribution with variance  $1/S$ , and  $Z[\mathbf{j}, \tilde{\mathbf{j}} | G']$  is the MSRDJ functional (181) for fixed  $G'$ .

It is convenient to split the rotated degrees of freedom into the longitudinal mode  $X_0$  and the  $S - 1$  transverse modes  $X_\alpha \equiv y_\alpha$ ,  $\alpha = 1, \dots, S - 1$ . In this notation, the interaction part of the MSRDJ action reads

$$S_{\text{int}}[\mathbf{X}, \tilde{\mathbf{X}}] = \sigma \sum_{a,b=0}^{S-1} \int dt \tilde{X}_a(t) G'_{ab} X_b(t) = \sigma \int dt \left[ \sum_{\alpha, \beta=1}^{S-1} \tilde{y}_\alpha(t) G'_{\alpha\beta} y_\beta(t) + \sum_{\beta=1}^{S-1} \tilde{X}_0(t) G'_{0\beta} y_\beta(t) \right], \quad (191)$$

where the terms  $G'_{a0}$  are absent because the first column of  $G'$  is identically zero.

The dependence of the generating functional on the quenched disorder appears only through  $S_{\text{int}}$ . The disorder average is thus a Gaussian integral over the entries  $G'_{\alpha\beta}$  and  $G'_{0\beta}$ :

$$\overline{Z[\mathbf{j}, \tilde{\mathbf{j}}]} = \int \mathcal{D}\mathbf{X} \mathcal{D}\tilde{\mathbf{X}} \exp(-S_0[\mathbf{X}, \tilde{\mathbf{X}}] + \mathbf{j} \cdot \mathbf{X} + \tilde{\mathbf{j}} \cdot \tilde{\mathbf{X}}) \overline{\exp(-S_{\text{int}}[\mathbf{X}, \tilde{\mathbf{X}}])}_{G'}. \quad (192)$$

For a generic Gaussian variable  $G$  with variance  $1/S$  one has

$$\int dG \exp\left(-\frac{S}{2}G^2 + \sigma GA\right) \propto \exp\left(\frac{\sigma^2}{2S}A^2\right), \quad (193)$$

so that the average over  $G'_{\alpha\beta}$  and  $G'_{0\beta}$  yields quartic terms in the dynamical fields. Introducing the shorthand

$$A_{\alpha\beta} := \int dt \tilde{y}_\alpha(t) y_\beta(t), \quad A_{0\beta} := \int dt \tilde{X}_0(t) y_\beta(t), \quad (194)$$

the average over the transverse-transverse block gives

$$\overline{\exp\left[-\sigma \sum_{\alpha,\beta} \int dt \tilde{y}_\alpha(t) G'_{\alpha\beta} y_\beta(t)\right]}_{G'_{\alpha\beta}} = \exp\left[\frac{\sigma^2}{2S} \sum_{\alpha,\beta=1}^{S-1} A_{\alpha\beta}^2\right], \quad (195)$$

and the average over the longitudinal row produces

$$\overline{\exp\left[-\sigma \sum_{\beta=1}^{S-1} \int dt \tilde{X}_0(t) G'_{0\beta} y_\beta(t)\right]}_{G'_{0\beta}} = \exp\left[\frac{\sigma^2}{2S} \sum_{\beta=1}^{S-1} A_{0\beta}^2\right]. \quad (196)$$

The sums over indices can be expressed in terms of collective fields. Writing

$$\sum_{\alpha,\beta} A_{\alpha\beta}^2 = \sum_{\alpha,\beta} \int dt ds \tilde{y}_\alpha(t) \tilde{y}_\alpha(s) y_\beta(t) y_\beta(s), \quad (197)$$

and defining the transverse order parameters

$$Q(t, s) := \frac{1}{S-1} \sum_{\alpha=1}^{S-1} \tilde{y}_\alpha(t) \tilde{y}_\alpha(s), \quad C(t, s) := \frac{1}{S-1} \sum_{\beta=1}^{S-1} y_\beta(t) y_\beta(s), \quad (198)$$

one obtains

$$\sum_{\alpha,\beta} A_{\alpha\beta}^2 = (S-1)^2 \int dt ds Q(t, s) C(t, s). \quad (199)$$

Similarly,

$$\sum_{\beta} A_{0\beta}^2 = \sum_{\beta} \int dt ds \tilde{X}_0(t) \tilde{X}_0(s) y_\beta(t) y_\beta(s) = (S-1) \int dt ds \tilde{X}_0(t) \tilde{X}_0(s) C(t, s). \quad (200)$$

Putting everything together, the quenched-disorder averaged generating functional can be written as

$$\begin{aligned} \overline{Z[\mathbf{j}, \tilde{\mathbf{j}}]} &= \int \mathcal{D}\mathbf{y} \mathcal{D}\tilde{\mathbf{y}} \mathcal{D}\mathbf{X}_0 \mathcal{D}\tilde{\mathbf{X}}_0 \exp \left\{ -S_0[\mathbf{y}, \tilde{\mathbf{y}}] - S_0[\mathbf{X}_0, \tilde{\mathbf{X}}_0] \right. \\ &\quad + \sum_{\alpha=1}^{S-1} \int dt [j_\alpha(t) y_\alpha(t) + \tilde{j}_\alpha(t) \tilde{y}_\alpha(t)] + \int dt [j_0(t) X_0(t) + \tilde{j}_0(t) \tilde{X}_0(t)] \\ &\quad \left. + \frac{\sigma^2}{2S} (S-1)^2 \int dt ds Q(t, s) C(t, s) + \frac{\sigma^2}{2S} (S-1) \int dt ds \tilde{X}_0(t) \tilde{X}_0(s) C(t, s) \right\}, \end{aligned} \quad (201)$$

where  $S_0[\mathbf{y}, \tilde{\mathbf{y}}]$  and  $S_0[\mathbf{X}_0, \tilde{\mathbf{X}}_0]$  denote the bare Ornstein-Uhlenbeck actions (without couplings) for the transverse and longitudinal modes, respectively. The quenched average has generated an effective quartic interaction between response and activity fields, mediated by the collective correlators  $Q(t, s)$  and  $C(t, s)$ .

## 4.5 HS transformation

We now introduce a Hubbard–Stratonovich (HS) transformation in order to decouple the quartic interaction generated by the quenched disorder. The quenched-averaged generating functional can be written as

$$\begin{aligned} \overline{Z[\mathbf{j}, \tilde{\mathbf{j}}]} = & \int \mathcal{D}y \mathcal{D}\tilde{y} \mathcal{D}X_0 \mathcal{D}\tilde{X}_0 \exp \left\{ -S_0[y, \tilde{y}] - S_0[X_0, \tilde{X}_0] \right. \\ & + \sum_{\alpha=1}^{S-1} \int dt [j_\alpha(t) y_\alpha(t) + \tilde{j}_\alpha(t) \tilde{y}_\alpha(t)] + \int dt [j_0(t) X_0(t) + \tilde{j}_0(t) \tilde{X}_0(t)] \\ & \left. + \frac{\sigma^2}{2S} (S-1)^2 \int dt ds Q(t, s) C(t, s) + \frac{\sigma^2}{2S} (S-1) \int dt ds \tilde{X}_0(t) \tilde{X}_0(s) C(t, s) \right\}, \end{aligned} \quad (202)$$

where

$$Q(t, s) = \frac{1}{S-1} \sum_{\alpha=1}^{S-1} \tilde{y}_\alpha(t) \tilde{y}_\alpha(s), \quad C(t, s) = \frac{1}{S-1} \sum_{\beta=1}^{S-1} y_\beta(t) y_\beta(s). \quad (203)$$

The quartic interaction term proportional to  $Q(t, s) C(t, s)$  couples all transverse degrees of freedom through the empirical correlators. To obtain a single-site description, we introduce a collective field  $C(t, s)$  together with a conjugate field  $\tilde{C}(t, s)$ , and enforce the definition of  $C(t, s)$  via a functional constraint.

We insert into (202) the following functional identity

$$\begin{aligned} 1 = & \int \mathcal{D}C \mathcal{D}\tilde{C} \exp \left\{ -\frac{(S-1)^2}{\sigma^2 S} \int dt ds C(t, s) \tilde{C}(t, s) \right. \\ & \left. + (S-1) \int dt ds \tilde{C}(t, s) \frac{1}{S-1} \sum_{\beta=1}^{S-1} y_\beta(t) y_\beta(s) \right\}, \end{aligned} \quad (204)$$

which plays the role of a functional  $\delta$ -constraint selecting  $C(t, s)$  as the empirical two-time correlator of the transverse variables. Up to an overall (irrelevant) normalization, the factor (204) implements

$$C(t, s) = \frac{1}{S-1} \sum_{\beta=1}^{S-1} y_\beta(t) y_\beta(s) \quad (205)$$

at the saddle point. The particular prefactor  $(S-1)^2/(\sigma^2 S)$  is chosen so that the resulting effective action acquires the standard dynamical mean-field structure.

Upon inserting (204) into (202) and collecting all terms depending on  $C$  and  $\tilde{C}$ , the quenched average takes the form

$$\begin{aligned} \overline{Z[\mathbf{j}, \tilde{\mathbf{j}}]} = & \int \mathcal{D}C \mathcal{D}\tilde{C} \exp \left\{ -\frac{(S-1)^2}{\sigma^2 S} \int dt ds C(t, s) \tilde{C}(t, s) \right\} \\ & \times \int \mathcal{D}y \mathcal{D}\tilde{y} \mathcal{D}X_0 \mathcal{D}\tilde{X}_0 \exp \left\{ -S_0[y, \tilde{y}] - S_0[X_0, \tilde{X}_0] \right. \\ & + \sum_{\alpha=1}^{S-1} \int dt [j_\alpha(t) y_\alpha(t) + \tilde{j}_\alpha(t) \tilde{y}_\alpha(t)] + \int dt [j_0(t) X_0(t) + \tilde{j}_0(t) \tilde{X}_0(t)] \\ & + \frac{\sigma^2}{2S} (S-1)^2 \int dt ds Q(t, s) C(t, s) \\ & + \frac{\sigma^2}{2S} (S-1) \int dt ds \tilde{X}_0(t) \tilde{X}_0(s) C(t, s) \\ & \left. + (S-1) \int dt ds \tilde{C}(t, s) \frac{1}{S-1} \sum_{\beta=1}^{S-1} y_\beta(t) y_\beta(s) \right\}. \end{aligned} \quad (206)$$

The exponent in (206) is now *quadratic* in each transverse degree of freedom  $(y_\alpha, \tilde{y}_\alpha)$ , so that the path integral over the transverse modes factorizes into a product of identical single-site contributions. Writing the quadratic terms in  $\tilde{y}_\alpha$  and  $y_\alpha$  explicitly, one finds that the transverse part of the action can be rewritten as

$$\begin{aligned} S_{\text{trans}}[y, \tilde{y}; C, \tilde{C}] &= \sum_{\alpha=1}^{S-1} \int dt \left[ \tilde{y}_\alpha(t) (\partial_t y_\alpha(t) + y_\alpha(t)) - \frac{D}{2} \tilde{y}_\alpha(t)^2 \right] \\ &\quad - \frac{1}{2} \sum_{\alpha=1}^{S-1} \int dt ds \tilde{y}_\alpha(t) C(t, s) \tilde{y}_\alpha(s) \\ &\quad - \sum_{\alpha=1}^{S-1} \int dt ds y_\alpha(t) \tilde{C}(t, s) y_\alpha(s), \end{aligned} \quad (207)$$

so that the transverse contribution to (206) can be written as

$$\begin{aligned} &\int \mathcal{D}y \mathcal{D}\tilde{y} \exp \left( -S_0[y, \tilde{y}] + \frac{1}{2} \sum_{\alpha=1}^{S-1} \tilde{y}_\alpha C \tilde{y}_\alpha + \sum_{\alpha=1}^{S-1} y_\alpha \tilde{C} y_\alpha + \dots \right) \\ &= \left[ \int \mathcal{D}y \mathcal{D}\tilde{y} \exp \left( -S_0[y, \tilde{y}] + \frac{1}{2} \tilde{y} C \tilde{y} + y \tilde{C} y \right) \right]^{S-1}, \end{aligned} \quad (208)$$

where in the last line  $(y, \tilde{y})$  denote a single transverse mode, and we have omitted the source terms for brevity. The longitudinal mode contributes a separate factor

$$Z_{\text{long}}[C] = \int \mathcal{D}X_0 \mathcal{D}\tilde{X}_0 \exp \left\{ -S_0[X_0, \tilde{X}_0] + \frac{\sigma^2}{2S} (S-1) \int dt ds \tilde{X}_0(t) C(t, s) \tilde{X}_0(s) \right\}. \quad (209)$$

The quenched-disorder averaged generating functional can therefore be cast in the standard dynamical mean-field form

$$\begin{aligned} \overline{Z[\mathbf{j}, \tilde{\mathbf{j}}]} &= \int \mathcal{D}C \mathcal{D}\tilde{C} \exp \left\{ -\frac{(S-1)^2}{\sigma^2 S} \int dt ds C(t, s) \tilde{C}(t, s) \right\} \\ &\quad \times \left[ Z_{\text{trans}}[C, \tilde{C}] \right]^{S-1} Z_{\text{long}}[C], \end{aligned} \quad (210)$$

where

$$Z_{\text{trans}}[C, \tilde{C}] = \int \mathcal{D}y \mathcal{D}\tilde{y} \exp \left\{ - \int dt [\tilde{y}(t) (\partial_t y(t) + y(t)) - \frac{D}{2} \tilde{y}(t)^2] + \frac{1}{2} \tilde{y} C \tilde{y} + y \tilde{C} y \right\}, \quad (211)$$

and  $Z_{\text{long}}[C]$  is given above. The fields  $C(t, s)$  and  $\tilde{C}(t, s)$  play the role of dynamical order parameters, describing the self-consistent two-time correlations and response functions of a single effective transverse degree of freedom.

## 4.6 Saddle-point approximation

The disorder-averaged generating functional has the dynamical mean-field representation

$$\begin{aligned} \overline{Z[\mathbf{j}, \tilde{\mathbf{j}}]} &= \int \mathcal{D}C \mathcal{D}\tilde{C} \exp \left\{ -S_{\text{eff}}[C, \tilde{C}] \right\}, \\ S_{\text{eff}}[C, \tilde{C}] &= \frac{(S-1)^2}{\sigma^2 S} \int dt ds C(t, s) \tilde{C}(t, s) \\ &\quad - (S-1) \ln Z_{\text{trans}}[C, \tilde{C}] - \ln Z_{\text{long}}[C], \end{aligned} \quad (212)$$

with

$$Z_{\text{trans}}[C, \tilde{C}] = \int \mathcal{D}y \mathcal{D}\tilde{y} \exp \left\{ - \int dt \left[ \tilde{y}(t)(\partial_t y(t) + y(t)) - \frac{D}{2} \tilde{y}(t)^2 \right] \right. \\ \left. + \frac{1}{2} \int dt ds \tilde{y}(t) C(t, s) \tilde{y}(s) + \int dt ds y(t) \tilde{C}(t, s) y(s) \right\}, \quad (213)$$

and

$$Z_{\text{long}}[C] = \int \mathcal{D}X_0 \mathcal{D}\tilde{X}_0 \exp \left\{ - \int dt \left[ \tilde{X}_0(t)(\partial_t X_0(t) + X_0(t)) - \frac{D}{2} \tilde{X}_0(t)^2 \right] \right. \\ \left. + \frac{\sigma^2}{2S} (S-1) \int dt ds \tilde{X}_0(t) C(t, s) \tilde{X}_0(s) \right\}. \quad (214)$$

The dynamical mean-field (DMF) equations follow from a saddle-point evaluation of the functional integral over  $C$  and  $\tilde{C}$  in the limit of large system size  $S$ . The saddle-point fields  $C^*(t, s)$  and  $\tilde{C}^*(t, s)$  are determined by the stationarity conditions

$$\frac{\delta S_{\text{eff}}}{\delta C(t, s)} \Big|_{C^*, \tilde{C}^*} = 0, \quad \frac{\delta S_{\text{eff}}}{\delta \tilde{C}(t, s)} \Big|_{C^*, \tilde{C}^*} = 0. \quad (215)$$

It is convenient to express these equations in terms of expectation values with respect to the single-site effective measures. For the transverse mode, expectation values are defined as

$$\langle \mathcal{O}[y, \tilde{y}] \rangle_{\text{trans}} := \frac{1}{Z_{\text{trans}}[C^*, \tilde{C}^*]} \int \mathcal{D}y \mathcal{D}\tilde{y} \mathcal{O}[y, \tilde{y}] e^{-S_{\text{eff}}[y, \tilde{y}; C^*, \tilde{C}^*]}, \quad (216)$$

where

$$S_{\text{eff}}[y, \tilde{y}; C^*, \tilde{C}^*] = \int dt \left[ \tilde{y}(t)(\partial_t y(t) + y(t)) - \frac{D^2}{2} \tilde{y}(t)^2 \right] \\ - \frac{1}{2} \int dt ds \tilde{y}(t) C^*(t, s) \tilde{y}(s) - \int dt ds y(t) \tilde{C}^*(t, s) y(s). \quad (217)$$

For the longitudinal mode,

$$\langle \mathcal{O}[X_0, \tilde{X}_0] \rangle_{\text{long}} := \frac{1}{Z_{\text{long}}[C^*]} \int \mathcal{D}X_0 \mathcal{D}\tilde{X}_0 \mathcal{O}[X_0, \tilde{X}_0] e^{-S_{\text{eff}}[X_0, \tilde{X}_0; C^*]}, \quad (218)$$

with

$$S_{\text{eff}}[X_0, \tilde{X}_0; C^*] = \int dt \left[ \tilde{X}_0(t)(\partial_t X_0(t) + X_0(t)) - \frac{D}{2} \tilde{X}_0(t)^2 \right] \\ - \frac{\sigma^2}{2S} (S-1) \int dt ds \tilde{X}_0(t) C^*(t, s) \tilde{X}_0(s). \quad (219)$$

Using the standard identities

$$\frac{\delta \ln Z_{\text{trans}}}{\delta \tilde{C}(t, s)} = \langle y(t) y(s) \rangle_{\text{trans}}, \quad \frac{\delta \ln Z_{\text{trans}}}{\delta C(t, s)} = \frac{1}{2} \langle \tilde{y}(t) \tilde{y}(s) \rangle_{\text{trans}}, \quad (220)$$

and

$$\frac{\delta \ln Z_{\text{long}}}{\delta C(t, s)} = \frac{\sigma^2}{2S} (S-1) \langle \tilde{X}_0(t) \tilde{X}_0(s) \rangle_{\text{long}}, \quad (221)$$

the saddle-point equations can be written explicitly.

The variation with respect to  $\tilde{C}(t, s)$  gives

$$0 = \frac{\delta S_{\text{eff}}}{\delta \tilde{C}(t, s)} \Big|_{C^*, \tilde{C}^*} \\ = \frac{(S-1)^2}{\sigma^2 S} C^*(t, s) - (S-1) \langle y(t) y(s) \rangle_{\text{trans}}. \quad (222)$$

Therefore,

$$C^*(t, s) = \frac{\sigma^2 S}{S - 1} \langle y(t) y(s) \rangle_{\text{trans}} = \frac{\sigma^2 S}{S - 1} C_y^*(t, s), \quad (223)$$

where we have introduced the notation  $C_y(t, s) = \langle y(t) y(s) \rangle_{\text{trans}}$  to denote the correlator of the variable  $y(t)$  (the asterisk denotes just this correlator evaluated at the saddle).

The variation with respect to  $C(t, s)$  yields

$$\begin{aligned} 0 &= \frac{\delta S_{\text{eff}}}{\delta C(t, s)} \Big|_{C^*, \tilde{C}^*} \\ &= \frac{(S - 1)^2}{\sigma^2 S} \tilde{C}^*(t, s) - (S - 1) \frac{1}{2} \langle \tilde{y}(t) \tilde{y}(s) \rangle_{\text{trans}} - \frac{\sigma^2}{2S} (S - 1) \langle \tilde{X}_0(t) \tilde{X}_0(s) \rangle_{\text{long}}. \end{aligned} \quad (224)$$

Dividing by  $(S - 1)$  and rearranging,

$$\tilde{C}^*(t, s) = \frac{\sigma^2 S}{2(S - 1)} \left[ \langle \tilde{y}(t) \tilde{y}(s) \rangle_{\text{trans}} + \frac{\sigma^2}{S} \langle \tilde{X}_0(t) \tilde{X}_0(s) \rangle_{\text{long}} \right]. \quad (225)$$

Equations (223) and (225) are the self-consistent dynamical mean-field equations for the collective correlator  $C(t, s)$  and the conjugate kernel  $\tilde{C}(t, s)$ . In the limit of large system size  $S$ , the factors  $S/(S - 1)$  approach unity, and the longitudinal contribution in (225) is suppressed by a factor  $1/S$ . To leading order in  $1/S$  one obtains the familiar DMF relations

$$C^*(t, s) \simeq \sigma^2 \langle y(t) y(s) \rangle_{\text{trans}} = \sigma^2 C_y^*(t, s), \quad \tilde{C}^*(t, s) \simeq \frac{\sigma^2}{2} \langle \tilde{y}(t) \tilde{y}(s) \rangle_{\text{trans}} = 0, \quad (226)$$

which describe a single effective transverse degree of freedom interacting with a self-consistent Gaussian bath. We have set  $\tilde{C}^*(t, s) = 0$  because the self-correlation of the fields  $\tilde{y}$  must vanish [7].

## 4.7 Effective single-particle dynamics and linear response

At the saddle point, the transverse contribution to the disorder-averaged generating functional factorizes into  $(S - 1)$  identical copies of a single effective degree of freedom. The dynamics of a typical transverse mode  $y(t)$  is encoded in the MSRDJ action  $S_{\text{eff}}[y, \tilde{y}; C^*, \tilde{C}^*]$ ,

$$\begin{aligned} S_{\text{eff}}[y, \tilde{y}; C^*, \tilde{C}^*] &= \int dt \left[ \tilde{y}(t) (\partial_t y(t) + y(t)) - \frac{D}{2} \tilde{y}(t)^2 \right] \\ &\quad - \frac{1}{2} \int dt ds \tilde{y}(t) C^*(t, s) \tilde{y}(s) - \int dt ds y(t) \tilde{C}^*(t, s) \tilde{y}(s), \end{aligned} \quad (227)$$

where  $C^*$  and  $\tilde{C}^*$  are the saddle-point values of the collective kernels. This is precisely the MSRDJ action of a linear Langevin equation with additive Gaussian noise. More explicitly, the effective single-particle dynamics of a transverse mode can be written as

$$\partial_t y(t) = -y(t) + \eta(t) + \sqrt{D} \xi(t), \quad (228)$$

where  $\xi(t)$  is a standard white noise with  $\langle \xi(t) \xi(s) \rangle = \delta(t - s)$ , and  $\eta(t)$  is a zero-mean Gaussian ‘‘mean-field’’ input with covariance

$$\langle \eta(t) \eta(s) \rangle = C^*(t, s). \quad (229)$$

The total effective noise  $\zeta(t) := \eta(t) + D \xi(t)$  is therefore Gaussian with covariance

$$\langle \zeta(t) \zeta(s) \rangle = C^*(t, s) + D \delta(t - s), \quad (230)$$

and the DMF equation (223) enforces the self-consistency between this noise covariance and the autocorrelation of the solution  $y(t)$ .

**Linear response function.** To compute the response function of the effective single-particle process, we add a small external field  $h(t)$  to the dynamics (228),

$$\partial_t y(t) = -y(t) + \eta(t) + \sqrt{D} \xi(t) + h(t). \quad (231)$$

The (causal) linear response function is defined as

$$R^*(t, s) := \left. \frac{\delta \langle y(t) \rangle}{\delta h(s)} \right|_{h=0}, \quad (232)$$

and is related to the MSRDJ fields by

$$R^*(t, s) = \langle y(t) \tilde{y}(s) \rangle_{\text{eff}}. \quad (233)$$

Because the equation is linear and the noise has zero mean, the average  $\langle y(t) \rangle$  obeys the deterministic equation

$$\partial_t \langle y(t) \rangle = -\langle y(t) \rangle + h(t), \quad (234)$$

irrespective of the detailed noise statistics. Writing the formal solution as

$$\langle y(t) \rangle = \int_{-\infty}^{\infty} ds R^*(t, s) h(s), \quad (235)$$

and inserting this into the deterministic equation, one finds that  $R^*$  must satisfy

$$\frac{\partial}{\partial t} R^*(t, s) = -R^*(t, s) + \delta(t - s), \quad R^*(t, s) = 0 \quad \text{for } t < s, \quad (236)$$

where causality enforces  $R^*(t, s) = 0$  for  $t < s$ . The unique solution is

$$R^*(t, s) = \theta(t - s) e^{-(t-s)}, \quad (237)$$

with  $\theta$  the Heaviside step function. In terms of the time difference  $\tau = t - s$ , we write

$$R^*(\tau) := R^*(t, t - \tau) = \theta(\tau) e^{-\tau}. \quad (238)$$

The response function in frequency space is defined as the Fourier transform of  $R^*(\tau)$ ,

$$\chi(\omega) := \int_{-\infty}^{\infty} d\tau e^{i\omega\tau} R^*(\tau) = \int_0^{\infty} d\tau e^{-(1-i\omega)\tau} = \frac{1}{1 - i\omega}. \quad (239)$$

Thus, for the linear network considered here, the effective transverse degree of freedom has the same response function as a bare Ornstein–Uhlenbeck process: all the dependence on the coupling  $\sigma$  enters through the self-consistent noise covariance  $C^*$ , while the linear response (239) remains fixed.

## 4.8 Longitudinal mode at the DMFT saddle

The longitudinal single-site MSRDJ action at the saddle reads

$$\begin{aligned} S_{\text{long}}[X_0, \tilde{X}_0; C^*] &= \int dt \left[ \tilde{X}_0(t) (\partial_t X_0(t) + X_0(t)) - \frac{D^2}{2} \tilde{X}_0(t)^2 \right] \\ &\quad - \frac{\sigma^2}{2S} (S-1) \int dt ds \tilde{X}_0(t) C^*(t, s) \tilde{X}_0(s). \end{aligned} \quad (240)$$

This is of the standard MSRDJ form for a linear Langevin equation with additive Gaussian noise. Introducing the effective noise kernel

$$\Gamma_0(t, s) := D^2 \delta(t - s) + \frac{\sigma^2}{S} (S-1) C^*(t, s), \quad (241)$$

we can rewrite

$$S_{\text{long}}[X_0, \tilde{X}_0; C^*] = \int dt \tilde{X}_0(t) (\partial_t X_0(t) + X_0(t)) - \frac{1}{2} \int dt ds \tilde{X}_0(t) \Gamma_0(t, s) \tilde{X}_0(s). \quad (242)$$

By the usual MSRDJ correspondence, this action describes the effective longitudinal dynamics

$$\partial_t X_0(t) = -X_0(t) + \zeta_0(t), \quad (243)$$

where  $\zeta_0(t)$  is a zero-mean Gaussian process with covariance

$$\langle \zeta_0(t) \zeta_0(s) \rangle = D^2 \delta(t-s) + \frac{\sigma^2}{S} (S-1) C^*(t, s). \quad (244)$$

The dynamical mean-field equations for the order parameters  $C(t, s)$  and  $\tilde{C}(t, s)$  in the large- $S$  limit yield:

$$C^*(t, s) \simeq \sigma^2 C_y^*(t, s). \quad (245)$$

Crucially,  $C^*(t, s)$  in this expression is the transverse DMFT order parameter determined self-consistently; it does not depend on the longitudinal mode. Therefore, at the DMFT saddle the longitudinal mode is *not* self-consistent: it is a simple Ornstein–Uhlenbeck process with linear drift  $-X_0$  driven by a Gaussian noise whose colored component is entirely set by the transverse dynamics. All nontrivial self-consistency and critical behavior reside in the transverse sector, while the longitudinal mode behaves as a passive readout of the network fluctuations.

On the other hand, the longitudinal mode can be related with the mean activity of the network:

$$M(t) := \frac{1}{\sqrt{S}} X_0(t), \quad (246)$$

so that  $X_0(t) = \sqrt{S} M(t)$ . Differentiating with respect to time and using (243) gives

$$\begin{aligned} \partial_t M(t) &= \frac{1}{\sqrt{S}} \partial_t X_0(t) = \frac{1}{\sqrt{S}} [-X_0(t) + \zeta_0(t)] \\ &= -M(t) + \frac{1}{\sqrt{S}} \zeta_0(t). \end{aligned} \quad (247)$$

Thus, for finite  $S$  the mean activity satisfies

$$\partial_t M(t) = -M(t) + \eta_M(t), \quad (248)$$

with an effective noise

$$\eta_M(t) := \frac{1}{\sqrt{S}} \zeta_0(t), \quad (249)$$

whose covariance, by (244), is

$$\begin{aligned} \langle \eta_M(t) \eta_M(s) \rangle &= \frac{1}{S} \langle \zeta_0(t) \zeta_0(s) \rangle \\ &= \frac{1}{S} \left[ D^2 \delta(t-s) + \frac{\sigma^2}{S} (S-1) C^*(t, s) \right] \\ &= \mathcal{O}\left(\frac{1}{S}\right). \end{aligned} \quad (250)$$

Therefore, in the thermodynamic limit  $S \rightarrow \infty$  the mean activity converges to the deterministic solution of

$$\partial_t M(t) = -M(t), \quad (251)$$

while the stochastic fluctuations around this mean are suppressed as  $\text{Var}[M(t)] = \mathcal{O}(1/S)$ . In contrast, the rescaled longitudinal mode  $X_0(t) = \sqrt{S} M(t)$  remains an  $\mathcal{O}(1)$  fluctuation variable governed by the Ornstein–Uhlenbeck dynamics (243) with colored noise set by the transverse DMFT kernel  $C^*(t, s)$ . This decoupling of the mean with respect to the quenched disorder is precisely what we observed when performing DMFT directly into the ISLM, a condition made possible by the row-sum normalization of the matrix  $G_{ij}$ .

## 4.9 Gaussian fluctuations and Hessian around the saddle point

The dynamical mean-field equations are obtained from the saddle-point conditions of the effective action

$$S_{\text{eff}}[C, \tilde{C}] = \frac{(S-1)^2}{\sigma^2 S} \int dt ds C(t, s) \tilde{C}(t, s) - (S-1) \ln Z_{\text{trans}}[C, \tilde{C}] - \ln Z_{\text{long}}[C]. \quad (252)$$

Beyond mean-field, the leading corrections are governed by the Gaussian fluctuations of the collective fields  $C$  and  $\tilde{C}$  around their saddle-point values  $C^*$  and  $\tilde{C}^*$ .

**Fluctuation fields and expansion.** Fluctuations of the order parameter (of the external field created by the quench disorder) are parametrized as

$$C(t, s) = C^*(t, s) + \frac{1}{\sqrt{S-1}} \delta C(t, s), \quad \tilde{C}(t, s) = \tilde{C}^*(t, s) + \frac{1}{\sqrt{S-1}} \delta \tilde{C}(t, s). \quad (253)$$

The factor  $1/\sqrt{S-1}$  is chosen so that the quadratic fluctuation action remains of order one as  $S \rightarrow \infty$ .

The effective action is expanded to second order as

$$S_{\text{eff}}[C, \tilde{C}] = S_{\text{eff}}[C^*, \tilde{C}^*] + S^{(1)}[\delta C, \delta \tilde{C}] + S^{(2)}[\delta C, \delta \tilde{C}] + \dots, \quad (254)$$

where  $S^{(1)}$  vanishes by construction (saddle-point equations), and  $S^{(2)}$  is the quadratic form

$$S^{(2)}[\delta C, \delta \tilde{C}] = \frac{1}{2} \int dt_1 ds_1 dt_2 ds_2 \begin{pmatrix} \delta C(t_1, s_1) \\ \delta \tilde{C}(t_1, s_1) \end{pmatrix}^\top \mathcal{H}(t_1, s_1; t_2, s_2) \begin{pmatrix} \delta C(t_2, s_2) \\ \delta \tilde{C}(t_2, s_2) \end{pmatrix}, \quad (255)$$

with the Hessian kernel

$$\mathcal{H} = \begin{pmatrix} H_{CC} & H_{C\tilde{C}} \\ H_{\tilde{C}C} & H_{\tilde{C}\tilde{C}} \end{pmatrix}, \quad (256)$$

defined by the second functional derivatives of  $S_{\text{eff}}$  at the saddle point,

$$\begin{aligned} H_{CC}(t_1, s_1; t_2, s_2) &= \frac{\delta^2 S_{\text{eff}}}{\delta C(t_1, s_1) \delta C(t_2, s_2)} \Big|_{C^*, \tilde{C}^*}, \\ H_{\tilde{C}\tilde{C}}(t_1, s_1; t_2, s_2) &= \frac{\delta^2 S_{\text{eff}}}{\delta \tilde{C}(t_1, s_1) \delta \tilde{C}(t_2, s_2)} \Big|_{C^*, \tilde{C}^*}, \\ H_{C\tilde{C}}(t_1, s_1; t_2, s_2) &= \frac{\delta^2 S_{\text{eff}}}{\delta C(t_1, s_1) \delta \tilde{C}(t_2, s_2)} \Big|_{C^*, \tilde{C}^*}, \\ H_{\tilde{C}C}(t_1, s_1; t_2, s_2) &= \frac{\delta^2 S_{\text{eff}}}{\delta \tilde{C}(t_1, s_1) \delta C(t_2, s_2)} \Big|_{C^*, \tilde{C}^*}. \end{aligned} \quad (257)$$

**Second derivatives and connected four-point functions.** The collective term

$$\frac{(S-1)^2}{\sigma^2 S} \int dt ds C(t, s) \tilde{C}(t, s) \quad (258)$$

contributes only to the mixed block  $H_{C\tilde{C}}$ :

$$\frac{\delta^2}{\delta C(1) \delta \tilde{C}(2)} \left[ \frac{(S-1)^2}{\sigma^2 S} \int C \tilde{C} \right] = \frac{(S-1)^2}{\sigma^2 S} \delta(t_1 - t_2) \delta(s_1 - s_2), \quad (259)$$

while its  $CC$  and  $\tilde{C}\tilde{C}$  derivatives vanish.

The contributions from the single-site partition functions are expressed in terms of connected four-point functions. For the transverse mode, the identities

$$\frac{\delta \ln Z_{\text{trans}}}{\delta \tilde{C}(t_1, s_1)} = \langle y(t_1) y(s_1) \rangle_{\text{trans}}, \quad \frac{\delta \ln Z_{\text{trans}}}{\delta C(t_1, s_1)} = \frac{1}{2} \langle \tilde{y}(t_1) \tilde{y}(s_1) \rangle_{\text{trans}}, \quad (260)$$

imply

$$\begin{aligned}\frac{\delta^2 \ln Z_{\text{trans}}}{\delta \tilde{C}(t_1, s_1) \delta \tilde{C}(t_2, s_2)} &= \langle y(t_1) y(s_1) y(t_2) y(s_2) \rangle_{\text{trans},c}, \\ \frac{\delta^2 \ln Z_{\text{trans}}}{\delta C(t_1, s_1) \delta C(t_2, s_2)} &= \frac{1}{4} \langle \tilde{y}(t_1) \tilde{y}(s_1) \tilde{y}(t_2) \tilde{y}(s_2) \rangle_{\text{trans},c}, \\ \frac{\delta^2 \ln Z_{\text{trans}}}{\delta C(t_1, s_1) \delta \tilde{C}(t_2, s_2)} &= \frac{1}{2} \langle \tilde{y}(t_1) \tilde{y}(s_1) y(t_2) y(s_2) \rangle_{\text{trans},c},\end{aligned}\tag{261}$$

where  $\langle \dots \rangle_{\text{trans},c}$  denotes connected correlation functions with respect to the effective single-site action of the transverse mode. Similarly, the longitudinal partition function  $Z_{\text{long}}[C]$  generates connected four-point functions of the longitudinal response field  $\tilde{X}_0$ ,

$$\frac{\delta^2 \ln Z_{\text{long}}}{\delta C(t_1, s_1) \delta C(t_2, s_2)} \propto \langle \tilde{X}_0(t_1) \tilde{X}_0(s_1) \tilde{X}_0(t_2) \tilde{X}_0(s_2) \rangle_{\text{long},c},\tag{262}$$

with analogous relations for mixed derivatives involving  $C$ .

**Explicit form of the Hessian blocks.** Collecting the contributions from the collective term and from  $Z_{\text{trans}}$  and  $Z_{\text{long}}$ , the Hessian blocks are

$$\begin{aligned}H_{\tilde{C}\tilde{C}}(t_1, s_1; t_2, s_2) &= -(S-1) \langle y(t_1) y(s_1) y(t_2) y(s_2) \rangle_{\text{trans},c}, \\ H_{CC}(t_1, s_1; t_2, s_2) &= -(S-1) \frac{1}{4} \langle \tilde{y}(t_1) \tilde{y}(s_1) \tilde{y}(t_2) \tilde{y}(s_2) \rangle_{\text{trans},c} - \left. \frac{\delta^2 \ln Z_{\text{long}}}{\delta C(t_1, s_1) \delta C(t_2, s_2)} \right|_{C^*}, \\ H_{C\tilde{C}}(t_1, s_1; t_2, s_2) &= \frac{(S-1)^2}{\sigma^2 S} \delta(t_1 - t_2) \delta(s_1 - s_2) - (S-1) \frac{1}{2} \langle \tilde{y}(t_1) \tilde{y}(s_1) y(t_2) y(s_2) \rangle_{\text{trans},c} - \left. \frac{\delta^2 \ln Z_{\text{long}}}{\delta C(t_1, s_1) \delta \tilde{C}(t_2, s_2)} \right|_{C^*},\end{aligned}\tag{263}$$

and, by symmetry,

$$H_{\tilde{C}C}(t_1, s_1; t_2, s_2) = H_{C\tilde{C}}(t_2, s_2; t_1, s_1).\tag{264}$$

The longitudinal contributions (second derivatives of  $\ln Z_{\text{long}}[C]$ ) are of order 1 in  $S$ , whereas the transverse contributions scale as  $(S-1)$ , which means that the quadratic action  $S^{(2)}$  is dominated, for large  $S$ , by the transverse sector. The longitudinal corrections enter  $H_{CC}$  and  $H_{C\tilde{C}}$  with an extra factor  $1/(S-1)$  relative to the transverse four-point functions and therefore vanish in the thermodynamic limit. To leading order in  $1/S$ , the Hessian kernel reduces to

$$\begin{aligned}H_{\tilde{C}\tilde{C}}(t_1, s_1; t_2, s_2) &\simeq -(S-1) \langle y(t_1) y(s_1) y(t_2) y(s_2) \rangle_{\text{trans},c}, \\ H_{CC}(t_1, s_1; t_2, s_2) &\simeq -(S-1) \frac{1}{4} \langle \tilde{y}(t_1) \tilde{y}(s_1) \tilde{y}(t_2) \tilde{y}(s_2) \rangle_{\text{trans},c}, \\ H_{C\tilde{C}}(t_1, s_1; t_2, s_2) &\simeq \frac{(S-1)^2}{\sigma^2 S} \delta(t_1 - t_2) \delta(s_1 - s_2) - (S-1) \frac{1}{2} \langle \tilde{y}(t_1) \tilde{y}(s_1) y(t_2) y(s_2) \rangle_{\text{trans},c}.\end{aligned}\tag{265}$$

The Gaussian theory defined by  $S^{(2)}$  determines the fluctuations of the correlations  $\delta C(t, s)$  around its mean-field value  $C^*(t, s)$ . Since all the Hessian elements contain an overall factor  $(S-1)$ , it is convenient to define an intensive Hessian  $\mathcal{H}_{AB} = H_{AB}/(S-1)$  and work just with  $\mathcal{H}$  for now on.

**The Hessian in Fourier space** Since the effective process is Gaussian, Wick's theorem applies and the four-point functions factorize into products of two-point functions. For instance,

$$\langle y(t_1) y(s_1) y(t_2) y(s_2) \rangle_{\text{eff},c} = C^*(t_1, t_2) C^*(s_1, s_2) + C^*(t_1, s_2) C^*(s_1, t_2),\tag{266}$$

where  $C^*(t, s) = \sigma^2 \langle y(t) y(s) \rangle_{\text{eff}}$  is the DMF two-point function. Similar Wick decompositions hold for the mixed correlators  $\langle \tilde{y} \tilde{y} y y \rangle_c$  and  $\langle \tilde{y} \tilde{y} \tilde{y} \tilde{y} \rangle_c$  in terms of  $C^*$  and the response functions.

At this point we choose the time arguments in such a way that we isolate the long-time fluctuations of correlations. We set

$$t_2 = t_1 + \tau_1, \quad s_2 = s_1 + \tau_2, \quad (267)$$

and consider the limit

$$|s_1 - t_1| \rightarrow \infty, \quad \tau_1, \tau_2 = \mathcal{O}(1), \quad (268)$$

assuming that the process has reached stationarity ( $C^*(t, s) = C^*(t - s)$ ) and loses correlations at long times. With this choice one obtains

$$C^*(t_1, t_2) = C^*(\tau_1), \quad C^*(s_1, s_2) = C^*(\tau_2), \quad C^*(t_1, s_2) = C^*(s_1 - t_1 + \tau_2) \rightarrow 0, \quad C^*(s_1, t_2) = C^*(t_1 - s_1 + \tau_1) \rightarrow 0, \quad (269)$$

where the last two limits vanish because the dynamics decorrelates on large time scales.

Using (266) together with (269), the connected four-point function simplifies to

$$\langle y(t_1) y(s_1) y(t_2) y(s_2) \rangle_{\text{eff}, c} \xrightarrow{|t_2 - t_1| \rightarrow \infty} C^*(\tau_1) C^*(\tau_2), \quad (270)$$

and therefore, in this limit,

$$\mathcal{H}_{\tilde{C}\tilde{C}} \rightarrow \mathcal{H}_{\tilde{C}\tilde{C}}(\tau_1, \tau_2) = -C^*(\tau_1) C^*(\tau_2), \quad (271)$$

with analogous expressions for the mixed and  $CC$  blocks. Passing to Fourier space,

$$\mathcal{H}_{AB}(\omega_1, \omega_2) = \int d\tau_1 d\tau_2 e^{i\omega_1 \tau_1 + i\omega_2 \tau_2} \mathcal{H}_{AB}(\tau_1, \tau_2), \quad (272)$$

one finds that the Hessian blocks are diagonal in frequency and can be written as

$$\mathcal{H}_{\tilde{C}\tilde{C}}(\omega_1, \omega_2) = -C^*(\omega_1) C^*(\omega_2), \quad (273)$$

$$\mathcal{H}_{C\tilde{C}}(\omega_1, \omega_2) = \left[ -\frac{1}{\sigma^2} + \chi(\omega_1) \chi(\omega_2) \right], \quad (274)$$

$$\mathcal{H}_{CC}(\omega_1, \omega_2) = 0, \quad (275)$$

where  $\chi(\omega)$  is the Fourier transform of the linear response function ( $R^*(t, s)$ ) of the effective single-site process, and  $C^*(\omega)$  is the Fourier transform of the DMF correlator.

**Four-point fluctuations and the observable  $\Psi$**  The Gaussian theory defined by the quadratic fluctuation action  $S^{(2)}[\delta C, \delta \tilde{C}]$  governs the fluctuations of the collective correlator  $C(t, s)$  around its saddle-point value  $C^*(t, s)$ . A convenient object to quantify these fluctuations is the four-time observable

$$\Psi(t_1, s_1, t_2, s_2) := S \langle \delta C(t_1, s_1) \delta C(t_2, s_2) \rangle, \quad \delta C(t, s) = C(t, s) - C^*(t, s), \quad (276)$$

which measures the width of the distribution of two-time correlations across different realizations of the quenched disorder and the noise. In simulations, however, one is usually interested in:

$$\Psi_y(t_1, s_1, t_2, s_2) := S \langle \delta C_y(t_1, s_1) \delta C_y(t_2, s_2) \rangle, \quad \delta C_y(t, s) = C_y(t, s) - C_y^*(t, s), \quad (277)$$

which can be expressed in terms of  $\Psi$  as:

$$\Psi_y = \frac{1}{\sigma^4} \Psi. \quad (278)$$

At quadratic order, we had arrived to the path integral over  $(\delta C, \delta \tilde{C})$  being Gaussian:

$$\mathcal{Z}_{\text{fluc}} = \int \mathcal{D}(\delta C) \mathcal{D}(\delta \tilde{C}) \exp \left[ -S^{(2)}[\delta C, \delta \tilde{C}] \right]. \quad (279)$$

For a Gaussian functional integral of the form

$$S^{(2)}[\Phi] = \frac{1}{2} \Phi^\top \mathcal{H} \Phi, \quad (280)$$

the covariance of the fluctuation fields is given by the inverse of the Hessian  $\mathcal{H}^{-1}$ . In our case, packing the fields into

$$\Phi := \begin{pmatrix} \delta C \\ \delta \tilde{C} \end{pmatrix}, \quad (281)$$

we obtain

$$\langle \delta C(t_1, s_1) \delta C(t_2, s_2) \rangle = [\mathcal{H}^{-1}]_{CC}(t_1, s_1; t_2, s_2), \quad (282)$$

where  $[\mathcal{H}^{-1}]_{CC}$  denotes the  $C$ - $C$  block of the inverse matrix.

The observable  $\Psi$  that quantifies the width of the fluctuations of the correlator is defined as

$$\Psi(t_1, s_1; t_2, s_2) := S \langle \delta C(t_1, s_1) \delta C(t_2, s_2) \rangle, \quad (283)$$

so that, in terms of the Hessian,

$$\Psi(t_1, s_1; t_2, s_2) = S [\mathcal{H}^{-1}]_{CC}(t_1, s_1; t_2, s_2) = \frac{S}{S-1} [\mathcal{H}^{-1}]_{CC}(t_1, s_1; t_2, s_2) \approx [\mathcal{H}]_{CC}^{-1}, \quad (284)$$

where, in the last equality, we have approximated  $S/(S-1) \approx 1$  in the large  $S$  limit.

**Schur-complement formula.** To make (284) explicit, we use the general formula for the inverse of a block matrix. Consider the abstract block form

$$\mathcal{H} = \begin{pmatrix} A & B \\ B^\top & D \end{pmatrix}, \quad (285)$$

where here

$$A \equiv H_{CC}, \quad B \equiv H_{C\tilde{C}}, \quad D \equiv H_{\tilde{C}\tilde{C}}. \quad (286)$$

Assuming that  $D$  is invertible, the  $C$ - $C$  block of the inverse matrix  $\mathcal{H}^{-1}$  is given by the Schur complement:

$$[\mathcal{H}^{-1}]_{CC} = (A - B D^{-1} B^\top)^{-1}. \quad (287)$$

Applying this to our case, we obtain

$$\langle \delta C(t_1, s_1) \delta C(t_2, s_2) \rangle = \left[ \mathcal{H}_{CC} - \mathcal{H}_{C\tilde{C}} \mathcal{H}_{\tilde{C}\tilde{C}}^{-1} \mathcal{H}_{\tilde{C}C} \right]^{-1}(t_1, s_1; t_2, s_2). \quad (288)$$

Therefore, the fluctuation observable  $\Psi$  can be written compactly as

$$\Psi(t_1, s_1; t_2, s_2) = \left[ \mathcal{H}_{CC} - \mathcal{H}_{C\tilde{C}} \mathcal{H}_{\tilde{C}\tilde{C}}^{-1} \mathcal{H}_{\tilde{C}C} \right]^{-1}(t_1, s_1; t_2, s_2). \quad (289)$$

(289) is the Schur-complement expression for  $\Psi$ : it shows that the covariance of the order-parameter fluctuations  $\delta C$  is obtained by inverting the *effective* kernel

$$\mathcal{K}_{CC} := \mathcal{H}_{CC} - \mathcal{H}_{C\tilde{C}} \mathcal{H}_{\tilde{C}\tilde{C}}^{-1} \mathcal{H}_{\tilde{C}C}, \quad (290)$$

which incorporates both the direct  $CC$  block and the indirect coupling through the  $\tilde{C}$  sector.

**Fluctuations of the long-time window covariance** Using the Schur-complement relation

$$\langle \delta C(\omega) \delta C(-\omega) \rangle = \left[ \mathcal{H}_{CC}(\omega) - \mathcal{H}_{C\tilde{C}}(\omega) \mathcal{H}_{\tilde{C}\tilde{C}}^{-1}(\omega) \mathcal{H}_{\tilde{C}C}(\omega) \right]^{-1}, \quad (291)$$

and the fact that here  $\mathcal{H}_{CC}(\omega) = 0$ , we obtain

$$\langle \delta C(\omega) \delta C(-\omega) \rangle = \frac{C^*(\omega) C^*(-\omega)}{\left[ 1 - \sigma^2 \chi(\omega) \chi(-\omega) \right]^2}. \quad (292)$$

The four-point observable  $\Psi(\omega) = S \langle \delta C(\omega) \delta C(-\omega) \rangle$  thus reads

$$\Psi(\omega) = \left[ \frac{|C^*(\omega)|}{1 - \sigma^2 \chi(\omega) \chi(-\omega)} \right]^2. \quad (293)$$

This expression relates the fluctuation spectrum of the two-point correlator to terms of the DMF correlator  $C^*$  and the linear response function  $\chi$ . Substituting the expression for the linear response (239), finally gives:

$$\Psi(\omega) = \left[ \frac{\frac{|C^*(\omega)|}{\sigma^2}}{1 - \frac{1}{1 + \omega^2}} \right]^2. \quad (294)$$

In particular, let us observe that:

$$\frac{\Psi(\omega)}{|C^*(\omega)|^2} = \frac{\Psi_y(\omega)}{|C_y(\omega)|^2} = \left[ \frac{1}{1 - \sigma(\omega)^2} \right]^2, \quad (295)$$

with  $\sigma(\omega)^2 = \sigma^2 / (1 + \omega^2)$ .

#### 4.10 Connection with microscopic observables

**Average correlations.** Up to this point, we have derived a closed expression that links the fluctuations of the correlations to the amplitude of the quenched disorder,  $\sigma$ , within the DMF framework. We now relate these macroscopic quantities to microscopic observables that can be directly computed from simulations (or data).

We denote by  $C_{ij}(\omega)$  the empirical covariance matrix of the dynamics (180). Concretely,  $C_{ij}(\omega)$  is the frequency-dependent covariance between  $y_i(t)$  and  $y_j(t)$  at frequency  $\omega$ :

$$C_{ij}(\omega) := \langle y_i(\omega) y_j(-\omega) \rangle, \quad (296)$$

where  $\langle \cdot \rangle$  denotes the average over both the quenched disorder and the dynamical noise. The DMF self-covariance, averaged over sites, is defined as

$$C_y(\omega) := \frac{1}{S} \sum_{i=1}^S C_{ii}(\omega) = \frac{1}{S} \sum_{i=1}^S \langle y_i(\omega) y_i(-\omega) \rangle. \quad (297)$$

Thus, the DMF order parameter  $C_y(\omega)$  is identified with the site-averaged diagonal of the microscopic covariance matrix.

From the saddle-point analysis, the effective dynamics of a typical transverse mode is given by the linear Langevin equation

$$\partial_t y(t) = -y(t) + \eta(t) + \sqrt{D} \xi(t), \quad (298)$$

where  $\xi(t)$  is a standard white noise,  $\langle \xi(t) \xi(s) \rangle = \delta(t-s)$ , and  $\eta(t)$  is a zero-mean Gaussian ‘‘mean-field’’ input with covariance

$$\langle \eta(t) \eta(s) \rangle = \sigma^2 C_y(t, s). \quad (299)$$

In frequency space, the power spectrum of  $y(t)$  reads

$$C_y(\omega) = \langle |y(\omega)|^2 \rangle = |\chi(\omega)|^2 (C_\eta(\omega) + D), \quad (300)$$

where  $\chi(\omega)$  is the linear response function and  $C_\eta(\omega)$  is the power spectrum of  $\eta(t)$ . DMF self-consistency enforces  $C_\eta(\omega) = \sigma^2 C_y(\omega)$ . Using the explicit response for the linear dynamics,  $\chi(\omega) = (1 - i\omega)^{-1}$ , one obtains

$$C_y(\omega) = \frac{D}{1 + \omega^2 - \sigma^2}. \quad (301)$$

In particular, the equal-time variance  $C_y(0)$  diverges as  $\sigma \rightarrow 1$  from below, indicating that the diagonal entries of the covariance matrix grow without bound as the system approaches the edge of chaos.

**Second moment of the correlations.** We now relate the second moment of the covariance matrix to the macroscopic four-point observable obtained in the beyond-DMF analysis. To this end, we introduce the empirical scalar order parameter for a given realization of the quenched disorder:

$$\hat{\mathcal{C}}(\omega) := \frac{1}{S} \sum_{i=1}^S y_i(\omega) y_i(-\omega), \quad (302)$$

so that its average is precisely the DMF self-covariance,

$$\langle \hat{\mathcal{C}}(\omega) \rangle = C_y(\omega). \quad (303)$$

Fluctuations of this order parameter are described by

$$\delta\hat{\mathcal{C}}(\omega) := \hat{\mathcal{C}}(\omega) - C_y(\omega). \quad (304)$$

The four-point object computed in the field-theoretic expansion is the precisely the variance of  $\hat{\mathcal{C}}(\omega)$ ,

$$\langle \delta\hat{\mathcal{C}}(\omega) \delta\hat{\mathcal{C}}(-\omega) \rangle = \langle \hat{\mathcal{C}}(\omega) \hat{\mathcal{C}}(-\omega) \rangle - |C_y(\omega)|^2. \quad (305)$$

Using the definition of  $\hat{\mathcal{C}}(\omega)$ , the first term can be written as

$$\begin{aligned} \langle \hat{\mathcal{C}}(\omega) \hat{\mathcal{C}}(-\omega) \rangle &= \left\langle \frac{1}{S} \sum_{i=1}^S y_i(\omega) y_i(-\omega) \frac{1}{S} \sum_{j=1}^S y_j(-\omega) y_j(\omega) \right\rangle \\ &= \frac{1}{S^2} \sum_{i,j=1}^S \langle y_i(\omega) y_i(-\omega) y_j(-\omega) y_j(\omega) \rangle. \end{aligned} \quad (306)$$

Since, to second order in  $S$ , dynamics are Gaussian, Wick's theorem gives, for each pair  $(i, j)$ ,

$$\begin{aligned} \langle y_i(\omega) y_i(-\omega) y_j(-\omega) y_j(\omega) \rangle &= \langle y_i(\omega) y_i(-\omega) \rangle \langle y_j(-\omega) y_j(\omega) \rangle \\ &\quad + \langle y_i(\omega) y_j(-\omega) \rangle \langle y_i(-\omega) y_j(\omega) \rangle \\ &\quad + \langle y_i(\omega) y_j(\omega) \rangle \langle y_i(-\omega) y_j(-\omega) \rangle. \end{aligned} \quad (307)$$

In a stationary real process, Fourier components of the same sign are uncorrelated for  $\omega \neq 0$ , so that  $\langle y_i(\omega) y_j(\omega) \rangle = 0$  and the last term vanishes. In terms of the microscopic covariances  $C_{ij}(\omega)$ , we obtain

$$\langle y_i(\omega) y_i(-\omega) y_j(-\omega) y_j(\omega) \rangle = C_{ii}(\omega) C_{jj}(\omega) + C_{ij}(\omega) C_{ij}(-\omega). \quad (308)$$

Substituting this into the expression for  $\langle \hat{\mathcal{C}}(\omega) \hat{\mathcal{C}}(-\omega) \rangle$  and using

$$|C_y(\omega)|^2 = \left( \frac{1}{S} \sum_i C_{ii}(\omega) \right)^2 = \frac{1}{S^2} \sum_{i,j} C_{ii}(\omega) C_{jj}(\omega), \quad (309)$$

(305) simplifies to

$$\begin{aligned} \langle \delta\hat{\mathcal{C}}(\omega) \delta\hat{\mathcal{C}}(-\omega) \rangle &= \frac{1}{S^2} \sum_{i,j} \left[ C_{ii}(\omega) C_{jj}(\omega) + C_{ij}(\omega) C_{ij}(-\omega) \right] - \frac{1}{S^2} \sum_{i,j} C_{ii}(\omega) C_{jj}(\omega) \\ &= \frac{1}{S^2} \sum_{i,j} C_{ij}(\omega) C_{ij}(-\omega). \end{aligned} \quad (310)$$

Therefore, the macroscopic four-point fluctuation of the DMF order parameter is directly related to the microscopic second moment of the covariance matrix:

$$\Psi_y(\omega) := S \langle \delta\hat{\mathcal{C}}(\omega) \delta\hat{\mathcal{C}}(-\omega) \rangle = \frac{1}{S} \sum_{i,j=1}^S C_{ij}(\omega) C_{ij}(-\omega). \quad (311)$$

**Normalized width and inference of the effective coupling.** The relation (311) provides the formal bridge between the DMF four-point function and the microscopic second moment of the covariance matrix. We now introduce the normalized width of the covariance distribution, which is the quantity that we use in practice to estimate the variance of interactions,  $\sigma^2$ .

We start by defining the second moment of the off-diagonal covariances as:

$$M_2(\omega) := \frac{1}{S(S-1)} \sum_{i \neq j} |C_{ij}(\omega)|^2. \quad (312)$$

The (dimensionless) normalized width of the covariance distribution is then defined by

$$\Delta^2(\omega) := \frac{M_2(\omega)}{C_y(\omega)^2}. \quad (313)$$

To relate  $\Delta^2(\omega)$  to  $\Psi_y(\omega)$ , we decompose the double sum into diagonal and off-diagonal contributions:

$$\sum_{i,j=1}^S C_{ij}(\omega) C_{ij}(-\omega) = \sum_{i=1}^S C_{ii}(\omega) C_{ii}(-\omega) + \sum_{i \neq j} C_{ij}(\omega) C_{ij}(-\omega). \quad (314)$$

Assuming exchangeability of units, the diagonal elements are all equal,  $C_{ii}(\omega) \approx C_y(\omega)$ , so that

$$\sum_{i=1}^S C_{ii}(\omega) C_{ii}(-\omega) \approx S |C_y(\omega)|^2, \quad (315)$$

and the off-diagonal part can be expressed in terms of  $M_2(\omega)$  as

$$\sum_{i \neq j} C_{ij}(\omega) C_{ij}(-\omega) = S(S-1) M_2(\omega). \quad (316)$$

Inserting these into the definition of  $\Psi_y(\omega)$  yields

$$\begin{aligned} \Psi_y(\omega) &= \frac{1}{S} [S |C_y(\omega)|^2 + S(S-1) M_2(\omega)] \\ &= |C_y(\omega)|^2 + (S-1) M_2(\omega). \end{aligned} \quad (317)$$

Solving for  $M_2(\omega)$  and using the definition (313), we obtain

$$M_2(\omega) = \frac{\Psi_y(\omega) - |C_y(\omega)|^2}{S-1}, \quad \Delta^2(\omega) = \frac{\Psi_y(\omega)/|C_y(\omega)|^2 - 1}{S-1}. \quad (318)$$

In the large- $S$  limit, this simplifies to

$$S \Delta^2(\omega) \simeq \frac{\Psi_y(\omega)}{|C_y(\omega)|^2} - 1. \quad (319)$$

On the other hand, plugging this expression into (295) gives:

$$\frac{\Psi_y(\omega)}{|C_y(\omega)|^2} = \frac{1}{(1 - \sigma_{\text{eff}}(\omega)^2)^2}, \quad (320)$$

where  $\sigma_{\text{eff}}(\omega)$  is the effective variance of the interactions at frequency  $\omega$ , inferred from the data. Inserting this into (319), we arrive at

$$S \Delta^2(\omega) = \frac{1}{(1 - \sigma_{\text{eff}}(\omega)^2)^2} - 1. \quad (321)$$

Solving for  $\sigma_{\text{eff}}(\omega)$  gives

$$\sigma_{\text{eff}}(\omega) = \sqrt{1 - \sqrt{\frac{1}{1 + S \Delta^2(\omega)}}}. \quad (322)$$

which allows us to estimate the effective variance of interactions  $\sigma_{\text{eff}}(\omega)$  just by means of the moments of the histogram of covariances.

## 4.11 Back to the original coordinates.

In the previous sections, the beyond-DMF four-point observable was related to the microscopic covariance matrix of the transverse variables  $y_i$  as

$$\Psi_y(\omega) = \frac{1}{S} \sum_{i,j=1}^S C_{ij}^{(y)}(\omega) C_{ij}^{(y)}(-\omega), \quad (323)$$

where

$$C_{ij}^{(y)}(\omega) := \langle y_i(\omega) y_j(-\omega) \rangle. \quad (324)$$

We now show that the same quantity, computed in the original coordinates  $\mathbf{x}(t)$ , is identical. This justifies computing the normalized width directly from the covariance of  $\mathbf{x}$ . Indeed, let  $U$  be the orthogonal matrix defining the change of basis,

$$\mathbf{X}(t) = U^\top \mathbf{x}(t), \quad \mathbf{x}(t) = U \mathbf{X}(t), \quad (325)$$

with  $\mathbf{X}(t) = (X_0(t), y_1(t), \dots, y_{S-1}(t))^\top$ . Denote by  $C^{(x)}(\omega)$  and  $C^{(y)}(\omega)$  the covariance matrices in the original and rotated bases, respectively,

$$C_{ij}^{(x)}(\omega) := \langle x_i(\omega) x_j(-\omega) \rangle, \quad C_{ab}^{(y)}(\omega) := \langle X_a(\omega) X_b(-\omega) \rangle. \quad (326)$$

By orthogonality of  $U$ , these are related by

$$C^{(x)}(\omega) = U C^{(y)}(\omega) U^\top. \quad (327)$$

We define the four-point observable in the original basis as

$$\Psi_x(\omega) := \frac{1}{S} \sum_{i,j=1}^S C_{ij}^{(x)}(\omega) C_{ij}^{(x)}(-\omega). \quad (328)$$

For a real stationary process one has  $C_{ij}^{(x)}(-\omega) = C_{ij}^{(x)}(\omega)^\dagger$  (where  $\dagger$  denotes the complex conjugate), so that

$$\sum_{i,j} C_{ij}^{(x)}(\omega) C_{ij}^{(x)}(-\omega) = \sum_{i,j} |C_{ij}^{(x)}(\omega)|^2 = \|C^{(x)}(\omega)\|_{\text{F}}^2, \quad (329)$$

where  $\|\cdot\|_{\text{F}}$  denotes the Frobenius norm,  $\|A\|_{\text{F}}^2 := \sum_{ij} |A_{ij}|^2 = \text{Tr}(AA^\dagger)$ . Similarly,

$$\sum_{i,j} C_{ij}^{(y)}(\omega) C_{ij}^{(y)}(-\omega) = \|C^{(y)}(\omega)\|_{\text{F}}^2. \quad (330)$$

Thus,

$$\Psi_x(\omega) = \frac{1}{S} \|C^{(x)}(\omega)\|_{\text{F}}^2, \quad \Psi_y(\omega) = \frac{1}{S} \|C^{(y)}(\omega)\|_{\text{F}}^2. \quad (331)$$

Using the relation (327) and the invariance of the Frobenius norm under orthogonal similarity transformations, we obtain

$$\|C^{(x)}(\omega)\|_{\text{F}}^2 = \|C^{(y)}(\omega)\|_{\text{F}}^2, \quad (332)$$

and hence

$$\Psi_x(\omega) = \Psi_y(\omega). \quad (333)$$

## 4.12 From long- to short-time window correlations

Throughout this whole section, we derived the relation between the normalized width of covariances and the diversity of interactions,  $\sigma$ . At  $\omega = 0$ , this corresponds to studying the dynamics at very long times. However, in most cases, the empirically available object is the short-time window covariance matrix. In

order to derive a similar expression for the short-time window covariance, we have to come back from the frequency domain to the time domain, exploiting the fact that, for a stationary process,

$$C_{ij}(\tau = 0) = \langle y_i(t)y_j(t+0) \rangle = \int_{\mathbb{R}} \frac{d\omega}{2\pi} C_{ij}(\omega) e^{-i\omega \cdot 0} = \int_{\mathbb{R}} \frac{d\omega}{2\pi} C_{ij}(\omega). \quad (334)$$

For example, the average self-covariance (diagonal terms in the short-time window covariance matrix) is given by

$$C_y^{\text{short}} = \int_{\mathbb{R}} \frac{D}{1 + \omega^2 - \sigma^2} \frac{d\omega}{2\pi} = \frac{D}{2\sqrt{1 - \sigma^2}}, \quad (335)$$

which describes the divergence of the self-covariance terms when the system approaches the edge of chaos.

On the other hand, in order to calculate the fluctuations in the correlations, we must Fourier-transform back the expression for the fourth-point moment in frequency space,

$$\Psi(\omega_1, \omega_2) = \frac{C(\omega_1)C(\omega_2)}{|1 - \sigma^2 \chi(\omega_1)\chi(\omega_2)|^2}, \quad (336)$$

where  $C(\omega) = D/(1 + \omega^2 - \sigma^2)$  and  $\chi(\omega) = 1/(1 - i\omega)$ . The short-time connected four-point function is then

$$\Psi^{\text{short}}(\tau_1 = 0, \tau_2 = 0) = \langle \delta C(\tau_1 = 0) \delta C(\tau_2 = 0) \rangle = \int \frac{d\omega_1}{2\pi} \frac{d\omega_2}{2\pi} \frac{C(\omega_1)C(\omega_2)}{|1 - \sigma^2 \chi(\omega_1)\chi(\omega_2)|^2}. \quad (337)$$

Directly working with the modulus in the complex plane is not convenient. Instead, we introduce the analytic function  $\tilde{\chi}(\omega) = 1/(1 + i\omega)$ , which coincides with  $\chi^*(\omega)$  on the real axis, and rewrite

$$|1 - \sigma^2 \chi(\omega_1)\chi(\omega_2)|^2 = (1 - \sigma^2 \chi(\omega_1)\chi(\omega_2))(1 - \sigma^2 \tilde{\chi}(\omega_1)\tilde{\chi}(\omega_2)). \quad (338)$$

A straightforward algebra then shows that, for real  $\omega_1, \omega_2$ ,

$$|1 - \sigma^2 \chi(\omega_1)\chi(\omega_2)|^2 = \frac{(\lambda - \omega_1\omega_2)^2 + (\omega_1 + \omega_2)^2}{(1 + \omega_1^2)(1 + \omega_2^2)}, \quad \lambda := 1 - \sigma^2. \quad (339)$$

Plugging this back into  $\Psi(\omega_1, \omega_2)$  yields the fully rational form

$$\Psi(\omega_1, \omega_2) = \frac{D^2}{(\omega_1^2 + \lambda)(\omega_2^2 + \lambda)} \frac{(1 + \omega_1^2)(1 + \omega_2^2)}{(\lambda - \omega_1\omega_2)^2 + (\omega_1 + \omega_2)^2}. \quad (340)$$

Therefore

$$\Psi^{\text{short}}(0, 0) = \frac{D^2}{(2\pi)^2} \int_{\mathbb{R}} d\omega_2 \frac{1 + \omega_2^2}{\omega_2^2 + \lambda} \int_{\mathbb{R}} d\omega_1 \frac{1 + \omega_1^2}{(\omega_1^2 + \lambda) [(\lambda - \omega_1\omega_2)^2 + (\omega_1 + \omega_2)^2]}. \quad (341)$$

We now perform the  $\omega_1$  integral by residues. For fixed real  $\omega_2$ , the integrand has poles at

$$\omega_1 = \pm i\sqrt{\lambda}, \quad \omega_1 = \frac{\lambda + i\omega_2}{\omega_2 - i}, \quad \omega_1 = \frac{\lambda - i\omega_2}{\omega_2 + i}. \quad (342)$$

Closing the contour in the upper half-plane, only two of these poles contribute:

$$\omega_1 = i\sqrt{\lambda}, \quad \omega_1 = \omega_+ := \frac{\lambda + i\omega_2}{\omega_2 - i}. \quad (343)$$

Evaluating the residues at these poles and summing them, one obtains the inner integral in closed form,

$$\int_{\mathbb{R}} d\omega_1 \frac{1 + \omega_1^2}{(\omega_1^2 + \lambda) [(\lambda - \omega_1\omega_2)^2 + (\omega_1 + \omega_2)^2]} = \pi \frac{\lambda + 1 - \sqrt{\lambda} + \frac{\omega_2^2}{\sqrt{\lambda}}}{(\lambda + \omega_2^2)^2} \equiv J(\omega_2). \quad (344)$$

Thus the short-time four-point amplitude reduces to a single real integral:

$$\Psi^{\text{short}}(0, 0) = \frac{D^2}{4\pi} \int_{\mathbb{R}} d\omega_2 \frac{(1 + \omega_2^2) (\lambda + 1 - \sqrt{\lambda} + \frac{\omega_2^2}{\sqrt{\lambda}})}{(\lambda + \omega_2^2)^3}. \quad (345)$$

This last integral can be evaluated again by residues or by using standard one-dimensional integrals of the form  $\int d\omega/(\omega^2 + \lambda)^n$ . After a straightforward but somewhat lengthy algebra one finds

$$\Psi^{\text{short}}(0, 0) = \frac{D^2}{32} \left( \frac{2}{\lambda} - \frac{2}{\lambda^2} + \frac{1}{\sqrt{\lambda}} + \frac{4}{\lambda^{3/2}} + \frac{3}{\lambda^{5/2}} \right). \quad (346)$$

Dividing by the squared short-time self-covariance,

$$(C_y^{\text{short}})^2 = \left( \frac{D}{2\sqrt{\lambda}} \right)^2 = \frac{D^2}{4\lambda}, \quad (347)$$

we obtain

$$\frac{\Psi^{\text{short}}}{(C_y^{\text{short}})^2} = \frac{1}{8} \left( 2 - \frac{2}{\lambda} + \sqrt{\lambda} + \frac{4}{\sqrt{\lambda}} + \frac{3}{\lambda^{3/2}} \right). \quad (348)$$

We now define the normalized variance of short-time correlations as

$$S\Delta_{\text{short}}^2 := \frac{\Psi^{\text{short}}}{(C_y^{\text{short}})^2} - 1 = \frac{1}{8} \left( -6 - \frac{2}{\lambda} + \sqrt{\lambda} + \frac{4}{\sqrt{\lambda}} + \frac{3}{\lambda^{3/2}} \right). \quad (349)$$

In terms of  $x = \sqrt{\lambda}$ , this relation can be written as a quartic equation,

$$8S\Delta_{\text{short}}^2 x^3 = -6x^3 - 2x + x^4 + 4x^2 + 3, \quad (350)$$

or equivalently

$$x^4 - (8S\Delta_{\text{short}}^2 + 6)x^3 + 4x^2 - 2x + 3 = 0, \quad x = \sqrt{\lambda}, \quad \lambda = 1 - \sigma^2. \quad (351)$$

This algebraic equation implicitly relates the interaction variance  $\sigma^2$  to the (normalized) fluctuations of short-time window correlations. Since we are interested in the regime close to the edge of chaos, it is convenient to consider the expansion for  $\lambda \simeq 1$  (small  $\sigma$ ). Writing  $\lambda = 1 - \varepsilon$  with  $\varepsilon \ll 1$ , we find

$$S\Delta_{\text{short}}^2 = \frac{\varepsilon}{2} + \frac{5}{8}\varepsilon^2 + \mathcal{O}(\varepsilon^3), \quad (352)$$

which can be inverted to obtain

$$\varepsilon \equiv 1 - \lambda \simeq 2S\Delta_{\text{short}}^2 - 5(S\Delta_{\text{short}}^2)^2 + \mathcal{O}((S\Delta_{\text{short}}^2)^3). \quad (353)$$

Using  $\lambda = 1 - \sigma^2$ , this finally yields the near-critical estimate

$$\sigma^2 \simeq 2S\Delta_{\text{short}}^2 - 5(S\Delta_{\text{short}}^2)^2 + \mathcal{O}((S\Delta_{\text{short}}^2)^3), \quad (354)$$

which can be used as a practical estimator relating the fluctuations of short-time window correlations to the diversity of interactions in the large- $S$  limit.

All of the calculations shown here are for a Gaussian matrix with connectivity  $C = 1$ . In the main text, we discuss the general case in which the connectivity  $C$  is fixed to a given value. In that case, the total variance of the interactions, let us denote it as  $g$ , is nothing but  $\sigma \cdot \sqrt{C}$  and it can be calculated by solving (349), where  $\lambda = 1 - g^2$  in that case.

## 5 The emergence of chaos

The idea that irregular fluctuations in ecological community abundances could be driven by deterministic chaotic dynamics has been debated—and often contested—in ecology for decades [8, 9]. Nonetheless, controlled experiments have reported clear signatures of chaos, including aperiodic trajectories and strange attractors, in insect populations [10, 11] and in simplified marine communities (barnacles, algae, and mussels) monitored in a marine reserve [12]. More recently, accumulating empirical and theoretical evidence suggests that chaotic dynamics may be more common in natural ecosystems than previously assumed [13].

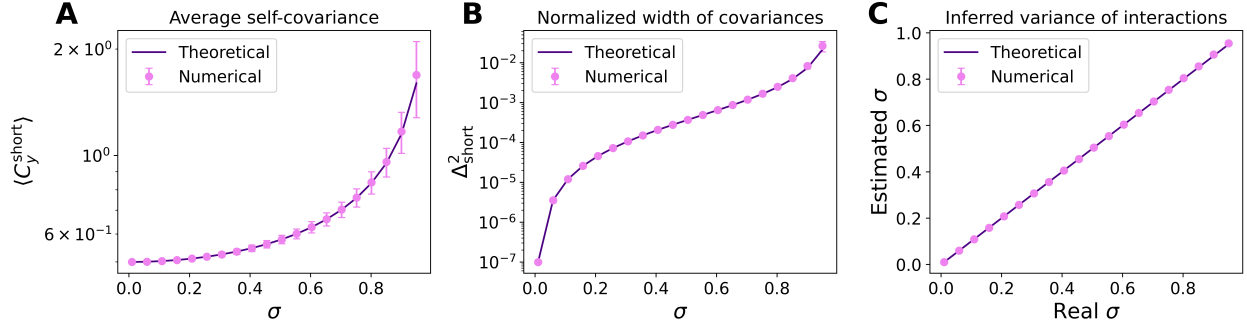


**Figure 1: Predictions from DMFT match numerical experiments from random networks of  $S = 500$  species, averaged over  $M = 10^3$  independent realizations.** **A.** The average self covariance scales with the  $\sigma$ , the fluctuations of the quenched disorder, as  $(1 - \sigma^2)^{-1/2}$ , when the system approaches the edge of instability. Numerical simulations, carried out by solving the Lyapunov equation numerically (in order to avoid possible finite-sampling effects) match theory perfectly. **B.** The normalized width of correlations,  $\Delta_{\text{short}}^2$  diverges as  $(1 - \sigma^2)^{-3/2}$  as  $\sigma$  approaches 1. **C.** Using DMFT,  $\sigma$  can be inferred just by measuring the normalized width of covariances. As observed, the estimator matches perfectly the real value of  $\sigma$ .

On the other hand, a growing body of theoretical and numerical work indicates that communities with random interactions can exhibit chaotic dynamics in generalized Lotka–Volterra models [14, 15, 16], as well as in more complex consumer–resource models [17].

In the main text, we argue that microbial communities operate in a fixed-point regime, close to the transition to chaos. This working hypothesis is attractive because it yields well-defined long-time mean abundances and maintains marginal statistics compatible with Grilli’s laws [18]. By contrast, in the chaotic regime the DMFT description contains a nonvanishing self-consistent noise term, which drives persistent fluctuations of species abundances. In Section 3.5, we show that these fluctuations generically spoil the marginal patterns predicted by Grilli’s laws. This motivates focusing on the fixed-point side of the transition.

This section provides a more detailed discussion of chaotic dynamics in the interacting stochastic logistic model introduced in the main text. We first analyze the deterministic (noise-free) limit, and then extend the discussion to the fully stochastic setting with environmental noise.

## 5.1 Chaos in the deterministic limit

**Chaos is fueled by immigration, and impossible with extinctions.** Whether a simple model with random interactions can sustain chaos is an interesting question in its own right, and it has motivated a substantial body of work in recent years. In generalized Lotka–Volterra models, chaotic dynamics typically entail large abundance fluctuations; in ecological settings, such fluctuations often drive some species to extinction [16, 14]. In a purely deterministic ODE formulation, however, extinction is not an absorbing event: species abundances remain strictly positive and can only approach zero asymptotically. This idealization is not biologically realistic: real communities are composed of a finite number of individuals, so sufficiently low abundances effectively imply extinction.

The only way to circumvent this issue within a deterministic ODE description is to modify the dynamics near vanishing abundances. A common choice is to include an infinitesimally small (but nonzero) immigration rate  $\lambda$ , which prevents abundances from collapsing to zero and thereby avoids effective extinctions [14].<sup>1</sup> From a modeling perspective, this corresponds to allowing individuals to enter the community from an external pool, i.e., to treating the system as open rather than isolated and thus able to exchange biomass

<sup>1</sup>A more rigorous alternative is to include demographic noise, which can drive populations to extinction and trap them at zero abundance through a genuine absorbing state [19, 20].

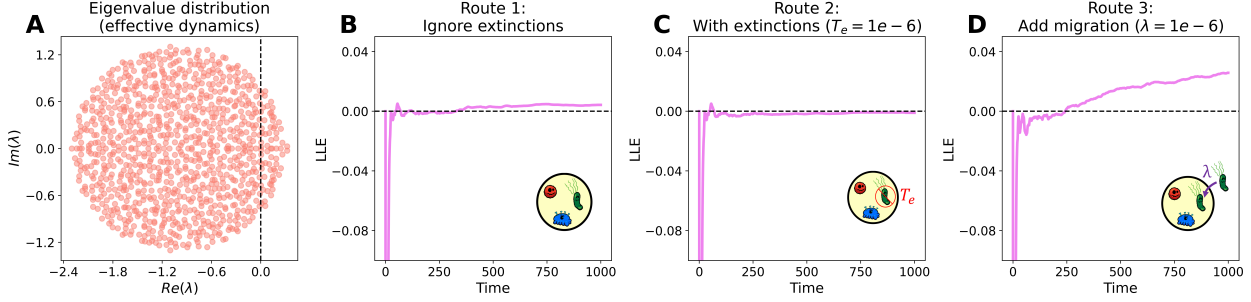


Figure 2: **Chaos in the generalized Lotka-Volterra model under different treatments of extinction in a system with  $S = 10^3$ , connectivity  $C = 1.0$ , and interaction strength  $\sigma = 1.3$ .** (A) Eigenvalue distribution of the linearized effective dynamics (dashed line marks  $\text{Re}(\lambda) = 0$ ). (B–D) Time evolution of the largest Lyapunov exponent (LLE) for three protocols: (B) Route 1 (no explicit extinction handling), (C) Route 2 (remove species once  $x_i < T_e$  with  $T_e = 10^{-6}$ ), and (D) Route 3 (add migration  $\lambda = 10^{-6}$ ). Routes 1 and 3 exhibit sustained positive LLE, indicating persistent chaos, whereas Route 2 displays only transient positivity before extinctions reduce the effective dimensionality and the dynamics relax to a stable state. Migration replenishes depleted species, effectively fueling the fluctuations that sustain chaotic dynamics.

with its surroundings [?, 21] The resulting dynamics can be written as

$$\dot{x}_i(t) = \frac{x_i(t)}{\tau} \left[ 1 + \sum_{j=1}^S A_{ij} x_j(t) \right] + \lambda. \quad (355)$$

We can therefore treat extinctions in three different ways:

- **Route 1:** Ignore extinctions altogether. Species can reach arbitrarily low abundances, which is mathematically consistent but biologically unrealistic.
- **Route 2:** Impose an extinction threshold  $T_e$  and remove species once  $x_i(t) < T_e$ . This approximates demographic discreteness (finite numbers of individuals).
- **Route 3:** Add a small immigration rate  $\lambda$  to prevent long-time collapse to zero, mimicking exchange with a surrounding environment.

Using these different approaches, we quantify sensitivity to initial conditions by computing the largest Lyapunov exponent (LLE), which measures the exponential divergence of nearby trajectories and is a standard diagnostic of chaos in deterministic dynamical systems [22].

In Figure 2, we present numerical estimates of the Lyapunov exponent [23, 24] obtained under the three extinction-handling protocols, for a system with  $S = 10^3$ , connectivity  $C = 1.0$ , and interaction strength  $\sigma = 1.3$ . Panel A shows the eigenvalue spectrum of the linearized dynamics, revealing that many modes are linearly unstable. Panels B–D report the time-dependent Lyapunov exponent for the three routes (ignoring extinctions, imposing an extinction threshold, and adding immigration). We observe that Routes 1 and 3 yield sustained chaotic dynamics, whereas Route 2 does not. Under Route 2, the Lyapunov exponent can transiently become positive: the dynamics initially display chaos, but as extinctions accumulate, the effective dimensionality of the system is reduced. The system then slowly relaxes toward a lower-dimensional attractor whose dynamics become stable again. By contrast, immigration enables chaos to persist by continually replenishing depleted species, effectively fueling the fluctuations that sustain the chaotic state.

From here on, we focus on the study of the system with a small immigration rate, that will be set to  $\lambda = 10^{-6}$ , unless otherwise stated. Figure 2 in the main text is reproduced following this choice.

**The boundary of chaos in the thermodynamic limit.** The DMFT description of the generalized Lotka–Volterra model used in this work suggests that the transition to chaos occurs at the marginal stability condition

$$\sigma\sqrt{C} = 1, \quad (356)$$

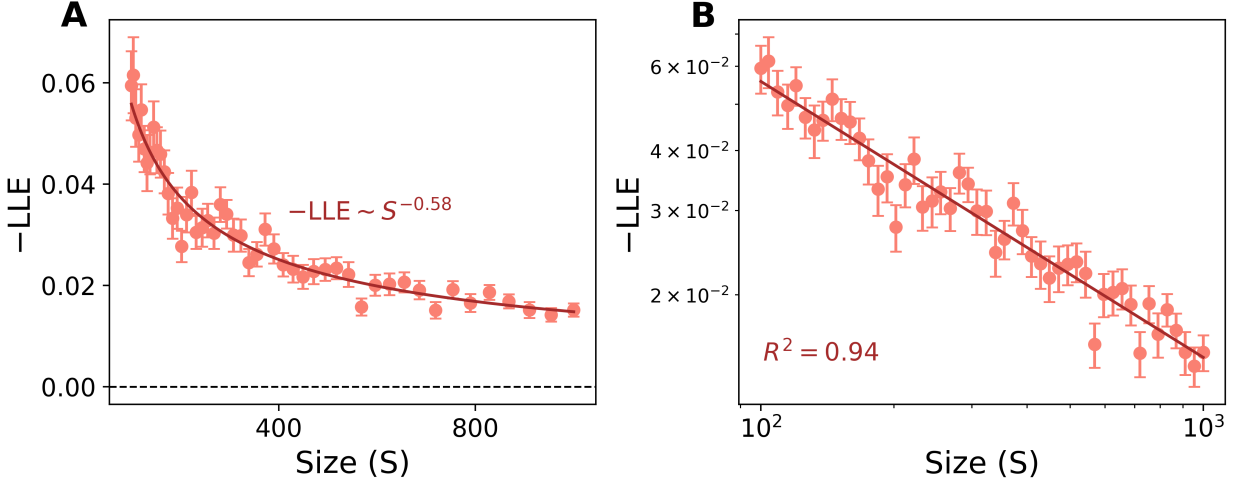


Figure 3: **Finite-size scaling of the largest Lyapunov exponent at the DMFT-predicted boundary.** Largest Lyapunov exponent (LLE) measured at  $(\sigma, C) = (1, 1)$  as a function of system size  $S$  (points represent mean values, while error bars stand for standard deviations over realizations -normalized by the square root of the number of measurements, which was  $M = 50$ ). **A:** linear axes; **B:** log-log representation. The solid line shows a power-law fit,  $-\text{LLE} \sim S^{-\alpha}$ , with  $R^2$  reported in the log-log panel. The observed decay of the (negative) LLE towards zero with increasing  $S$  indicates that the system approaches marginal stability as  $S \rightarrow \infty$ , consistent with the thermodynamic-limit transition occurring at  $\sigma\sqrt{C} = 1$ .

at least in the thermodynamic limit ( $S \rightarrow \infty$ ). For finite communities, finite-size effects can shift the apparent transition, effectively delaying the onset of chaotic dynamics. We test this prediction by measuring the largest Lyapunov exponent (LLE) at the putative critical point  $(\sigma, C) = (1, 1)$  for increasing system size. As shown in Fig. 3, the (negative) LLE decreases in magnitude with  $S$  and is consistent with approaching zero as  $S$  grows, indicating asymptotic marginal stability. This supports the DMFT conclusion that, in the thermodynamic limit, the onset of chaos is located precisely at  $\sigma\sqrt{C} = 1$ .

## 5.2 Noisy chaos

Let us now study chaos in the presence of stochastic fluctuations, which we model as a multiplicative noise term. Explicitly, we consider the ISLM analyzed in the main text:

$$\dot{x}_i(t) = \frac{x_i(t)}{\tau} \left[ 1 + \sum_{j=1}^S A_{ij} x_j(t) \right] + \lambda + \sigma_0 x_i(t) \xi_i(t). \quad (357)$$

The interplay between noise and chaos has been studied extensively [25, 26]. Depending on the context, noise can be stabilizing—for instance by suppressing chaotic dynamics [27]—or destabilizing, in the sense that it can induce chaotic-like behavior in systems that are non-chaotic in the deterministic limit [28, 29].

In the context of dynamical systems, the theory of random dynamical systems (RDS) [30] provides a natural generalization of chaos in the presence of noise. The stochastic dynamics generated by (357) defines a random flow  $\Phi(t, \omega, x)$  driven by the noise realization  $\omega$  (the collection of paths  $\{\xi_i(t)\}_i$ ). For each fixed realization  $\omega$ , the long-time behaviour is captured by a random attractor  $A(\omega)$  and an associated sample Lyapunov spectrum. In particular, the largest Lyapunov exponent (LLE)  $\lambda_1(\omega)$  quantifies the exponential divergence of nearby trajectories for that noise realization. Following standard practice [31], we characterize chaotic behaviour under noisy dynamics by the (disorder- and noise-averaged) LLE, i.e. by the expectation of  $\lambda_1(\omega)$  over realizations of the noise  $\xi_i(t)$  and the quenched disorder  $A_{ij}$ .

To quantify how noise modulates chaos, we computed the largest Lyapunov exponent (LLE) across the  $(\sigma, \sigma_0)$  plane for large systems. As we proved in section 1, there is a natural bound for how big the fluctuations

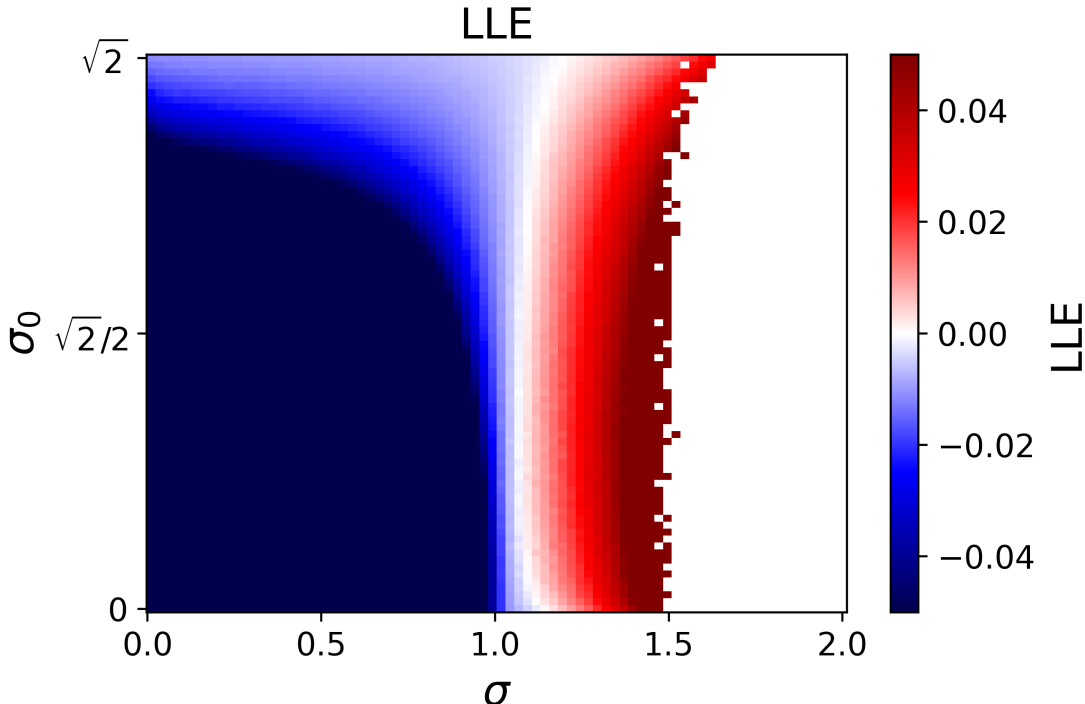


Figure 4: **Largest Lyapunov exponent (LLE) as a function of the interaction strength  $\sigma$  and noise amplitude  $\sigma_0$  for the noisy ISLM in (357).** The color map shows the disorder- and noise-averaged LLE over  $M = 50$  realizations of the interaction matrix and noise, for a system of size  $S = 10^3$  as a function of  $\sigma$  and  $\sigma_0$ . The white contour marks the locus where the LLE crosses zero, separating the chaotic regime ( $\text{LLE} > 0$ ) from the stable or marginally stable regime ( $\text{LLE} \leq 0$ ).

can be, i.e.,  $\sigma_0 < \sqrt{2/\tau}$  which, with this choice of parameters ( $\tau = 1$ ) translates to  $\sigma_0 < \sqrt{2}$ . Figure 4 shows the resulting phase diagram for  $S = 10^3$  species, averaged over  $M = 50$  realizations of the interaction matrix and the noisy drive. The white contour indicates the region where the LLE vanishes and thus separates a regime with robust noisy chaos ( $\text{LLE} > 0$ ) from a regime where the dynamics are stable or marginal ( $\text{LLE} \leq 0$ ). This confirms that the chaotic phase observed in the deterministic limit persists under stochastic fluctuations over a broad range of noise amplitudes.

## 6 Empirical analysis of gut microbiome cohorts

In the main text, we analyzed gut microbiome data across several disease cohorts and healthy controls (inflammatory bowel disease -IBD-, colorectal cancer -CRC-, *Clostridioides difficile* infection -CDI-, irritable bowel syndrome -IBS-, and their corresponding healthy controls), and compared their inferred distances to criticality (Figure 5). Because the IBD dataset contains the largest number of samples, it provides particularly reliable estimates of the distance to criticality and serves as a natural benchmark (see Table 1). In this section, we describe in detail the datasets and the subsampling-and-inference pipeline used to obtain the main-text results, and we systematically examine how these results depend on methodological choices. In particular, we report the specific subsampling parameters  $(r, p)$  used for each cohort, and we test the robustness of the inferred distances to criticality against variations in these parameters and in the number of samples.

## 6.1 Description of the data

For the disease analyses, we used the following datasets:

- IBD: Metagenomic data were obtained from the Inflammatory Bowel Disease Multi'omics Database (<https://ibdmdb.org/>) and [32].
- IBS: Metagenomic data were obtained from [33].
- CDI: Metagenomic data were obtained from [34].
- CRC: Metagenomic data were obtained from [35].
- Independent Healthy cohorts: Two independent healthy-control cohorts based on 16S rRNA sequencing were obtained from [36].

All these datasets were used in the pre-processed form curated by their original authors. We refer the reader to the corresponding publications for detailed descriptions of pre-processing pipelines. For our analyses, the only additional step was normalizing count data to obtain relative abundances for each sample. The resulting total number of samples and species is shown at Table 1.

Disease	Group	# Samples	# Taxa
IBD	CD	748	329
	UC	454	378
	Healthy	428	284
CRC	Healthy	251	517
	Stage_0	73	421
	Stage_I.II	111	479
	Stage_III.IV	74	436
CDI	Healthy	186	639
	Unhealthy	775	234
IBS	Healthy	152	1525
	IBS-C	148	1679
	IBS-D	176	1601
Healthy	Healthy 1	642	292 (Genus)
Healthy	Healthy 2	954	367 (Genus)

Table 1: Number of samples and taxa, generally species unless otherwise stated, per disease group.

## 6.2 Subsampling pipeline based on the species–samples ratios $r$ and $p$

For each disease cohort and diagnostic group (Table 1) we start from an abundance matrix

$$X \in \mathbb{R}^{S \times T},$$

where rows index taxa (species) and columns index samples. We then apply the following subsampling pipeline to estimate the distance to criticality from correlations.

**Definition of the control parameters  $p$  and  $r$ .** We control two dimensionless ratios:

1. A *subset fraction*  $p \in (0, 1]$ , which fixes the number of samples used in each subsample,

$$T_2 = \lfloor p T \rfloor, \tag{358}$$

where  $\lfloor x \rfloor$  denotes the floor function of  $x$ .

2. A *species–samples ratio*  $r > 0$ , defined at the subsample level as

$$r \equiv \frac{S_{\text{eff}}}{T_2}, \quad (359)$$

where  $S_{\text{eff}}$  is the number of taxa that remain in a given subsample after all filters (see below). In practice  $r$  is enforced as an upper bound on  $S_{\text{eff}}/T_2$  (we cannot create taxa if too few are present).

**Per-subsample procedure.** Given  $X$ , and fixed  $(r, p)$ , we generate  $M$  subsamples, indexed by  $m = 1, \dots, M$ . For each subsample we:

1. **Sample columns (samples).** We choose a set of columns  $J_m \subset \{1, \dots, T\}$  of size

$$|J_m| = T_2 = \lfloor p T \rfloor, \quad (360)$$

uniformly at random without replacement, and form the restricted abundance matrix

$$X_{\text{full}}^{(m)} = X[:, J_m] \in \mathbb{R}^{S \times T_2}, \quad (361)$$

where we used  $X[:, J_m]$  to indicate the submatrix formed by taking all the rows but only the columns in  $J_m$ .

2. **Presence filter within the subsample.** We define presence of taxon  $i$  in sample  $t$  within this subsample by

$$\text{present}_{it} = \begin{cases} 1, & X_{\text{full}}^{(m)}(i, t) \geq \tau, \\ 0, & \text{otherwise,} \end{cases} \quad (362)$$

with a small threshold  $\tau$  (we used  $\tau = 10^{-5}$ ). For each taxon we compute the number of presences,

$$k_i^{(m)} = \sum_{t=1}^{T_2} \text{present}_{it}. \quad (363)$$

We retain only taxa with at least `min_present` presences (we used `min_present = 3`):

$$\mathcal{I}_m = \{i \in \{1, \dots, S\} : k_i^{(m)} \geq \text{min\_present}\}. \quad (364)$$

If  $|\mathcal{I}_m| < \text{min\_rows}$  (with `min_rows = 3`), this subsample is discarded. Otherwise we define the restricted matrix

$$X^{(m)} = X_{\text{full}}^{(m)}[\mathcal{I}_m, :] \in \mathbb{R}^{S_{\text{raw}} \times T_2}, \quad (365)$$

where  $S_{\text{raw}} = |\mathcal{I}_m|$ .

3. **Enforcing the species–samples ratio.** The target ratio is  $r = S_{\text{eff}}/T_2$ ; internally we enforce a lower bound on the samples-per-species ratio

$$\rho_{\min} \equiv \frac{T_2}{S_{\text{eff}}} = \frac{1}{r}. \quad (366)$$

Given  $T_2$  and the current number of taxa  $S_{\text{raw}}$ , we compute a maximal allowed number of taxa

$$S_{\max} = \left\lfloor \frac{T_2}{\rho_{\min}} \right\rfloor = \lfloor r T_2 \rfloor. \quad (367)$$

If  $S_{\text{raw}} \leq S_{\max}$  we keep all taxa. If  $S_{\text{raw}} > S_{\max}$ , we rank taxa according to (i) their occupancy within the subsample,

$$\text{occ}_i^{(m)} = \frac{k_i^{(m)}}{T_2}, \quad (368)$$

and (ii) their total abundance,

$$A_i^{(m)} = \sum_{t=1}^{T_2} X^{(m)}(i, t), \quad (369)$$

and retain the  $S_{\max}$  taxa with highest  $\text{occ}_i^{(m)}$  (breaking ties by larger  $A_i^{(m)}$ ). This yields a final matrix

$$\tilde{X}^{(m)} \in \mathbb{R}^{S_{\text{eff}}^{(m)} \times T_2}, \quad (370)$$

with

$$S_{\text{eff}}^{(m)} \leq S_{\max} \quad \Rightarrow \quad \frac{S_{\text{eff}}^{(m)}}{T_2} \leq r. \quad (371)$$

The *effective* ratio in subsample  $m$  is then

$$r_{\text{eff}}^{(m)} = \frac{S_{\text{eff}}^{(m)}}{T_2}, \quad (372)$$

and we report its average  $\langle r_{\text{eff}} \rangle$  across subsamples.

4. **Standardization and removal of constant taxa.** For each taxon  $i$  in  $\tilde{X}^{(m)}$  we compute its mean and standard deviation across the  $T_2$  samples,

$$\mu_i^{(m)} = \frac{1}{T_2} \sum_{t=1}^{T_2} \tilde{X}^{(m)}(i, t), \quad \sigma_i^{(m)} = \sqrt{\frac{1}{T_2 - 1} \sum_{t=1}^{T_2} (\tilde{X}^{(m)}(i, t) - \mu_i^{(m)})^2}. \quad (373)$$

Taxa with vanishing variance ( $\sigma_i^{(m)} \leq \varepsilon$ , with a small numerical threshold  $\varepsilon$ ) are discarded. For the remaining taxa we construct  $z$ -scored abundances

$$Z^{(m)}(i, t) = \frac{\tilde{X}^{(m)}(i, t) - \mu_i^{(m)}}{\sigma_i^{(m)}}. \quad (374)$$

5. **Correlation matrix for the subsample.** From the standardized matrix  $Z^{(m)}$  we compute the empirical Pearson correlation matrix

$$C^{(m)} = \frac{1}{T_2 - 1} Z^{(m)} Z^{(m)\top}, \quad (375)$$

and explicitly set the diagonal to one,  $C_{ii}^{(m)} = 1$ .

6. **Distance-to-criticality estimator.** For each subsample, we feed  $C^{(m)}$  into the dynamical mean-field theory (DMFT)-based estimator of the distance to criticality,  $\hat{g}^{(m)}$ , derived in section 4.12.

**Aggregation across subsamples and cohorts.** For each diagnostic group and choice of  $(r, p)$  we thus obtain a collection of finite estimates  $\{\hat{g}^{(m)}\}_{m \in \mathcal{M}}$ , where  $\mathcal{M}$  is the set of successful subsamples. We characterize the distribution of  $\hat{g}$  by its empirical histogram  $\rho(\hat{g})$ , as well as its mean and spread, and compare these distributions across disease groups and across randomized controls (obtained by applying the same pipeline to suitably shuffled abundance matrices).

**Choice of the control parameters  $p$  and  $r$ .** Our subsampling scheme is controlled by two dimensionless parameters: the subset fraction  $p$  and the species–samples ratio  $r$ . The parameter  $p \in (0, 1]$  fixes the number of samples used in each subsample, meaning that a smaller value of  $p$  reduces  $T_2$ , so each subsample is built from fewer samples. This has two main consequences: (i) individual correlation matrices are more weakly sampled (noisier estimates), and (ii) the variability between different subsamples increases, because each subsample sees a more distinct subset of the cohort.

The parameter  $r > 0$  controls the species-to-samples ratio of each subsample. For fixed  $T_2$ , smaller values of  $r$  correspond to smaller  $S_{\text{eff}}$ , i.e. fewer rows in the abundance matrix. This improves the sampling quality of the correlation matrix (each entry is supported by relatively more samples per degree of freedom), but at the cost of reducing the dimensionality of the system and potentially discarding biologically relevant taxa.

In practice,  $p$  and  $r$  cannot both be chosen arbitrarily small: too small  $p$  yields very few samples per subsample, and too small  $r$  then forces  $S_{\text{eff}}$  to become very small as well, eventually leaving an insufficient number of species to define a meaningful correlation structure. Our choices of  $p$  and  $r$  therefore reflect a compromise between (i) having many, diverse subsamples (small  $p$ ), (ii) having well-sampled correlation matrices (small  $r$ ), and (iii) retaining a sufficiently large effective system size  $S_{\text{eff}}$ .

### 6.3 Assessing group separation via the area under the ROC curve

To quantify how well the inferred distances to criticality  $\hat{g}$  separate two groups of samples (e.g. Healthy vs. Diseased), we use the area under the receiver operating characteristic (ROC) curve, AUC [37, 38, 39]. Let  $X = \{\hat{g}_i^{(A)}\}_{i=1}^{n_A}$  and  $Y = \{\hat{g}_j^{(B)}\}_{j=1}^{n_B}$  denote the scores for two groups  $A$  and  $B$ . The AUC associated with using  $\hat{g}$  as a scalar classifier of group membership is defined as the probability that a randomly chosen sample from group  $A$  has a larger score than a randomly chosen sample from group  $B$ :

$$\text{AUC} \equiv \mathbb{P}(\hat{g}^{(A)} > \hat{g}^{(B)}) = \frac{1}{n_A n_B} \sum_{i=1}^{n_A} \sum_{j=1}^{n_B} \mathbb{I}[\hat{g}_i^{(A)} > \hat{g}_j^{(B)}], \quad (376)$$

where  $\mathbb{I}[\cdot]$  is the indicator function. An AUC of 0.5 corresponds to chance level (no separation between the two distributions of  $\hat{g}$ ), while  $\text{AUC} \rightarrow 1$  indicates that group  $A$  almost always has larger  $\hat{g}$  than group  $B$  (near-perfect separation in the chosen direction). Values  $\text{AUC} < 0.5$  simply mean that  $B$  tends to have larger  $\hat{g}$  than  $A$ , i.e. the direction of separation is reversed.

In practice, we estimate the AUC using the Mann–Whitney  $U$  statistic, which is known to be equivalent to the empirical probability  $\mathbb{P}(\hat{g}^{(A)} > \hat{g}^{(B)})$ . Writing  $U$  for the Mann–Whitney statistic comparing  $X$  and  $Y$ , with sample sizes  $n_A = |X|$  and  $n_B = |Y|$ , the empirical AUC is

$$\widehat{\text{AUC}} = \frac{U}{n_A n_B}. \quad (377)$$

This representation naturally yields a hypothesis test for separation between the two groups. Under the null hypothesis that both groups have the same underlying distribution of distances to criticality, the scores are exchangeable and the AUC equals 0.5:

$$H_0 : F_A(\hat{g}) = F_B(\hat{g}) \iff \mathbb{P}(\hat{g}^{(A)} > \hat{g}^{(B)}) = \frac{1}{2}, \quad (378)$$

where  $F_A$  and  $F_B$  are the cumulative distribution functions of  $\hat{g}$  in groups  $A$  and  $B$ . The alternative hypothesis of separation (in either direction) is

$$H_1 : F_A(\hat{g}) \neq F_B(\hat{g}) \iff \mathbb{P}(\hat{g}^{(A)} > \hat{g}^{(B)}) \neq \frac{1}{2}, \quad (379)$$

which corresponds to  $\text{AUC} \neq 0.5$ . The  $p$ -value associated with this contrast is obtained from the null distribution of the Mann–Whitney statistic  $U$  (or, equivalently, from the asymptotic normal approximation for large sample sizes). In our analysis, we report both the estimated AUC and its associated  $p$ -value. Large AUC values close to 1 together with very small  $p$ -values indicate that the inferred distances to criticality provide a strong and statistically significant separation between the two groups under comparison. To decide whether two groups are effectively separated by our methodology, we adopted the following criterion. Given two groups  $A$  and  $B$  with AUC

$$\text{AUC} = \mathbb{P}(\hat{g}^{(A)} > \hat{g}^{(B)}),$$

we define

$$\text{AUC}^* = \max(\text{AUC}, 1 - \text{AUC}),$$

so that  $\text{AUC}^*$  measures the distance from chance level (0.5) irrespective of which group has larger distances to criticality. We call two groups *separable* if  $\text{AUC}^* \geq 0.8$ , i.e. if at least 80% of cross-group pairs are ordered consistently in one direction. As we will see, all reported Mann–Whitney  $p$ -values are extremely small, so the main focus is on this criterion rather than on formal significance.

## 6.4 Values of $p$ and $r$ used for Figure 5 in the main text

In order to produce the figure shown in the main text (Figure 5), we used the values of  $p$  and  $r$  listed in Table 2. These parameters were chosen so as to balance three requirements: (i) obtain an effective number of taxa per subsample  $S_{\text{eff}}$  of order  $10^2$  whenever the cohort size allows it (and at least a few tens for smaller cohorts), thereby justifying the use of the DMFT estimator of  $g$ , which performs better at large  $S$ ; (ii) keep the species–samples ratio  $r = S_{\text{eff}}/T_2$  in a moderate range ( $r \sim 0.4\text{--}0.8$ ), ensuring that each retained taxon is reasonably well sampled; and (iii) use subset fractions  $p = T_2/T$  that are not too large (typically  $p \lesssim 0.7$ , with  $p = 0.5$  for IBS) so that many distinct subsamples can be drawn without repeatedly reusing the same samples. In the following subsections we explore how our conclusions are affected by systematic changes of  $r$  and  $p$ .

Disease	Group	$S_{\text{eff}}$	$T_2$	$r = S_{\text{eff}}/T_2$	$p = T_2/T$
IBD	Healthy	89	200	89/200 $\approx 0.445$	200/428 $\approx 0.467$
	CD	80	200	80/200 $\approx 0.400$	200/748 $\approx 0.267$
	UC	79	200	79/200 $\approx 0.395$	200/454 $\approx 0.441$
CRC	Healthy	123	176	123/176 $\approx 0.699$	176/251 $\approx 0.701$
	Stage 0	36	51	36/51 $\approx 0.706$	51/73 $\approx 0.699$
	Stage I–II	55	78	55/78 $\approx 0.705$	78/111 $\approx 0.703$
	Stage III–IV	36	52	36/52 $\approx 0.692$	52/74 $\approx 0.703$
CDI	Healthy	91	130	91/130 $\approx 0.700$	130/186 $\approx 0.699$
	Unhealthy	90	129	90/129 $\approx 0.698$	129/775 $\approx 0.166$
IBS	Healthy	61	76	61/76 $\approx 0.803$	76/152 $\approx 0.500$
	IBS-C	59	74	59/74 $\approx 0.797$	74/148 $\approx 0.500$
	IBS-D	70	88	70/88 $\approx 0.795$	88/176 $\approx 0.500$

Table 2: Subsampling parameters used for each cohort. Here  $S_{\text{eff}}$  is the typical effective number of taxa retained per subsample,  $T_2$  is the number of samples per subsample,  $r = S_{\text{eff}}/T_2$  is the species–samples ratio, and  $p = T_2/T$  is the subset fraction of samples used in each subsample.

## 6.5 Group separations for Figure 5 in the main text

The corresponding group separations in terms of the inferred distance to criticality are summarized in Table 3, which reports the pairwise AUCs between diagnostic subgroups for the same  $(r, p)$  choices used in Figure 5 (see 2), together with an indicator of whether each comparison satisfies our separability criterion  $\max(\text{AUC}, 1 - \text{AUC}) \geq 0.8$ . For all cohorts, the contrast between healthy and pooled non-healthy samples yields AUCs very close to 1 and is classified as “Separable”, indicating almost perfect discrimination based on  $\hat{g}$ . Within cohorts, several subgroup contrasts also show strong separation (e.g. healthy vs. individual tumor stages in CRC, or healthy vs. IBS-C/IBS-D in IBS), while a few comparisons display AUC values well below 0.5 (such as CD vs. UC or IBS-C vs. IBS-D), which are likewise marked as separable but correspond to a reversed ordering of the scores. Only in the comparison between Stage 0 and Stage I–II, we get a score that yields non separability between groups. Together, these results confirm that the qualitative patterns visible in Figure 5 reflect robust and statistically significant differences in distance to criticality between diagnostic groups.

## 6.6 Robustness of the distance-to-criticality estimates under varying sampling conditions

In this section, we revisit the same disease cohorts analyzed in the main text and systematically vary the sampling parameters used in our pipeline. For each group, we estimate the distance to criticality from abundance tables by repeatedly subsampling taxa and samples according to the  $(r, p)$ -scheme introduced in the previous section:  $p$  controls the fraction of samples used in each subsample, while  $r$  sets the effective species–samples ratio within that subsample. By exploring a range of  $(r, p)$  values around the choices used to

Disease	Pair	AUC	Separable?
IBD	Healthy vs CD	1.000	Yes
	Healthy vs UC	1.000	Yes
	CD vs UC	0.101	Yes
	Healthy vs pooled non-Healthy	1.000	Yes
CRC	Healthy vs Stage 0	0.999	Yes
	Healthy vs Stage I-II	1.000	Yes
	Healthy vs Stage III-IV	1.000	Yes
	Stage 0 vs Stage I-II	0.696	No
	Stage 0 vs Stage III-IV	0.952	Yes
	Stage I-II vs Stage III-IV	0.949	Yes
	Healthy vs pooled non-Healthy	1.000	Yes
CDI	Healthy vs Unhealthy	1.000	Yes
	Healthy vs pooled non-Healthy	1.000	Yes
IBS	Healthy vs IBS-C	0.995	Yes
	Healthy vs IBS-D	0.921	Yes
	IBS-C vs IBS-D	0.102	Yes
	Healthy vs pooled non-Healthy	0.958	Yes

Table 3: Pairwise areas under the ROC curve (AUC) between diagnostic groups within each disease cohort, computed from the distributions of inferred distance to criticality  $\hat{g}$  shown in the main-text Figure 5 (using the subsampling parameters in Table 2). “Pooled non-Healthy” denotes the union of all non-healthy subgroups within a cohort (e.g. CD and UC for IBD, all tumor stages for CRC). The “Separable?” column indicates whether the comparison meets the separability criterion  $\max(\text{AUC}, 1 - \text{AUC}) \geq 0.8$ , so that very small AUC values (e.g. CD vs UC or IBS-C vs IBS-D) correspond to strong separation with reversed ordering of the scores. In all cases, the corresponding Mann–Whitney  $U$ -test  $p$ -values are numerically extremely small (machine underflow to  $p \approx 0$ ).

generate Figure 5, we assess whether the qualitative separation between healthy and diseased microbiomes, and the relative ordering of cohorts, are robust to changes in sampling depth and effective dimensionality.

**Results for  $p = 0.5$**  We first investigated the effect of varying the effective species–samples ratio  $r$  at fixed subset fraction  $p = 0.5$ . For each disease cohort (IBD, CRC, CDI and IBS) and each target ratio  $r_{\text{target}} \in \{0.2, 0.7, 0.8\}$ , we drew repeated subsamples according to the  $(r, p)$ -scheme described above and estimated the distance to criticality  $\hat{g}$  for each subsample. We then quantified group separation using the AUC between the empirical distributions of  $\hat{g}$ , as detailed in the previous section.

Table 5 summarizes the AUC values for the comparison between healthy subjects and pooled non-healthy samples (all disease stages or subtypes combined) across different  $r_{\text{target}}$  at fixed  $p = 0.5$ . For IBD, CRC and CDI, the AUC between healthy and pooled non-healthy remains very high (typically  $\text{AUC} \gtrsim 0.96$ ) for all three values of  $r_{\text{target}}$ , indicating robust separation between healthy and diseased microbiomes that does not depend sensitively on the precise choice of species–samples ratio. For IBS, the separation is strong for  $r_{\text{target}} = 0.7$  and  $r_{\text{target}} = 0.8$  ( $\text{AUC} \geq 0.85$ ), but weaker for  $r_{\text{target}} = 0.2$  ( $\text{AUC} \approx 0.59$ ), suggesting that in this cohort a very aggressive reduction of the effective number of taxa degrades the ability to distinguish healthy from symptomatic subjects.

Tables 6–8 report the pairwise AUCs between different disease subgroups within each cohort. For IBD, healthy vs. CD and healthy vs. UC are always strongly separable for all  $r_{\text{target}}$ , while CD vs. UC displays strong separation only at  $r_{\text{target}} = 0.7$  and becomes less separated as  $r$  deviates from this value. In CRC, the healthy group is well separated from all tumor stages across all  $r_{\text{target}}$ , and some stage–stage comparisons (e.g. Stage I-II vs. Stage III-IV) also reach  $\text{AUC}^* \geq 0.8$  for certain values of  $r_{\text{target}}$ . In IBS, healthy vs. IBS-C and healthy vs. IBS-D are separable for the larger  $r_{\text{target}}$ , and the IBS-C vs. IBS-D comparison yields  $\text{AUC} \ll 0.5$  for  $r_{\text{target}} = 0.7$  and 0.8, indicating strong separation but with reversed ordering of the scores.

Figure 5 illustrates these results. Each row corresponds to a different target species–samples ratio  $r_{\text{target}}$  (with  $p = 0.5$  fixed), and each column to one disease cohort (IBD, CRC, CDI and IBS). In the main panels

we show the empirical distributions  $\rho(\hat{g})$  for the different diagnostic groups within each cohort, estimated from the original abundance tables. We observe a clear and systematic shift between healthy and diseased groups across a broad range of  $r_{\text{target}}$ , in line with the AUC values reported in Table 5. The insets display the same analysis applied to reshuffled abundance tables, in which the temporal/sample structure is destroyed by random permutation of the entries. In this null model, the distributions  $\rho(\hat{g})$  for the different groups largely collapse onto each other, and the strong between-group separations observed in the original data are no longer present. This confirms that the separation in distance to criticality is not a trivial consequence of sample size or marginal abundance distributions, but instead reflects genuine structure in the empirical microbiome data.

Table 4 summarizes, for each disease group, the nominal number of samples  $T_2$  and effective taxa  $S_{\text{eff}}$  used in each subsample when fixing  $p = 0.5$  and  $r_{\text{target}} \in \{0.2, 0.7, 0.8\}$ . These values are computed as  $T_2 = \lfloor pT \rfloor$  and  $S_{\text{eff}} \approx \lfloor r_{\text{target}} T_2 \rfloor$  from the total number of samples  $T$  in each group (Table 1), and thus represent upper bounds: the presence and variance filters in our pipeline can only reduce  $S_{\text{eff}}$  further.

For the IBD, CDI and IBS cohorts, the subsamples retain a reasonably large number of samples and taxa over most parameter choices. Typically,  $T_2 \gtrsim 70$  and  $S_{\text{eff}}$  lies in the tens to a few hundred for  $r_{\text{target}} = 0.7$  and 0.8. This is consistent with the robust separability we observe in the corresponding AUCs: healthy vs. pooled non-healthy comparisons for IBD, CRC and CDI yield  $\text{AUC}^* \gtrsim 0.96$  for all  $r_{\text{target}}$ , and IBS shows strong separation for  $r_{\text{target}} = 0.7$  and 0.8 (see Table 5). In contrast, for IBS at  $r_{\text{target}} = 0.2$ , the effective number of taxa is reduced to  $\sim 15\text{--}18$  per subsample, and the corresponding healthy vs. pooled IBS comparison shows only weak separation ( $\text{AUC} \approx 0.59$ ), indicating that an overly aggressive reduction of  $S_{\text{eff}}$  can degrade performance.

The CRC cohort is the most data-limited at the level of individual disease stages. While the healthy CRC group retains a moderate sampling depth ( $T_2 = 126$  and  $S_{\text{eff}} \approx 88\text{--}101$  depending on  $r_{\text{target}}$ ), the stage-specific groups have much smaller subsamples: for  $p = 0.5$  one typically has  $T_2 \approx 36\text{--}56$  and  $S_{\text{eff}} \approx 7\text{--}45$  for Stage 0, Stage I-II and Stage III-IV (Table 4). After applying occupancy and variance filters, the actual  $S_{\text{eff}}$  used in the correlation estimates may be even lower. This helps explain why, although healthy vs. pooled non-healthy CRC exhibits very high AUCs ( $\text{AUC}^* \gtrsim 0.96$  for all  $r_{\text{target}}$ ), some pairwise comparisons between individual stages show more variable behavior and should be interpreted with greater caution. In particular, the strong separations observed between certain stage pairs (e.g. Stage I-II vs. Stage III-IV at  $r_{\text{target}} = 0.7$  or 0.8) are based on subsamples with relatively few taxa and samples, and thus provide suggestive but less statistically robust evidence than the healthy vs. pooled CRC contrasts.

Disease	Group	$T$	$T_2 (p = 0.5)$	$S_{\text{eff}}(r = 0.2)$	$S_{\text{eff}}(r = 0.7)$	$S_{\text{eff}}(r = 0.8)$
IBD	Healthy (nonIBD)	428	214	43	150	171
	CD	748	374	75	262	299
	UC	454	227	45	159	182
CRC	Healthy	251	126	25	88	101
	Stage 0	73	36	7	25	29
	Stage I-II	111	56	11	39	45
	Stage III-IV	74	37	7	26	30
CDI	Healthy	186	93	19	65	74
	Unhealthy	234	117	23	82	94
IBS	Healthy	152	76	15	53	61
	IBS-C	148	74	15	52	59
	IBS-D	176	88	18	62	70

Table 4: Nominal number of samples  $T_2$  and effective taxa  $S_{\text{eff}}$  per subsample for  $p = 0.5$  and  $r_{\text{target}} \in \{0.2, 0.7, 0.8\}$ , computed as  $T_2 = \text{round}(pT)$  and  $S_{\text{eff}} \approx \text{round}(r_{\text{target}} T_2)$  from the total number of samples  $T$  in each group (see Table 1). In the actual pipeline, additional presence and variance filters can only reduce  $S_{\text{eff}}$ , so these values should be interpreted as upper bounds.

**Results for  $p = 0.7$**  Overall, the pattern at  $p = 0.7$  is very similar to that observed for  $p = 0.5$ . Healthy vs. pooled non-healthy comparisons (Table 9) show excellent separability for IBD, CRC and CDI across

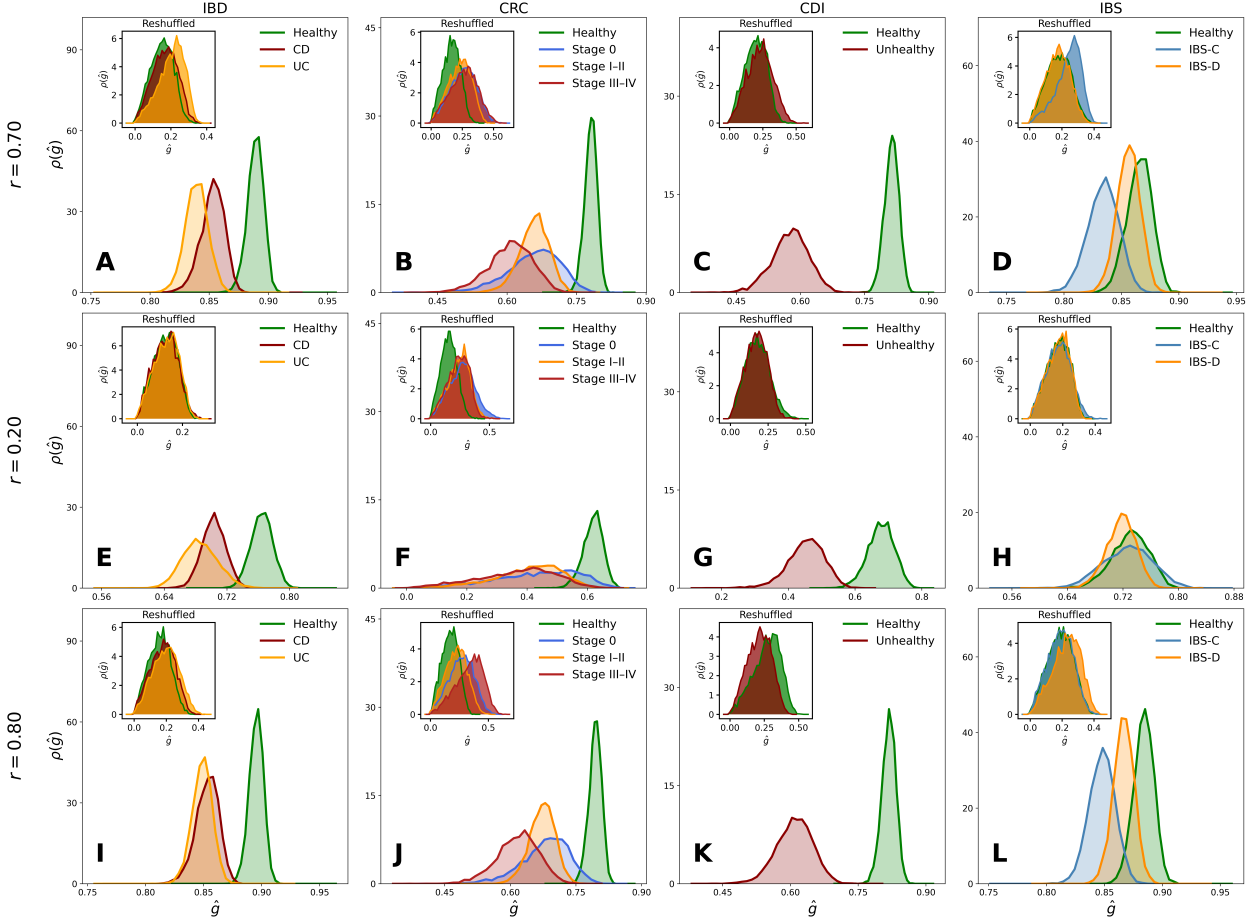


Figure 5: **Distributions of inferred distance to criticality for different disease cohorts at fixed subset fraction  $p = 0.5$  and varying target species-samples ratio  $r_{\text{target}} \in \{0.2, 0.7, 0.8\}$ .** Rows correspond to different values of  $r_{\text{target}}$ , and columns to IBD, CRC, CDI and IBS, respectively. Within each panel, we show  $\rho(\hat{g})$  for healthy and diseased subgroups estimated from the original abundance tables. Insets display the corresponding distributions obtained after reshuffling the abundance data (random permutation of entries), which largely collapses the group-specific curves and eliminates the strong separations observed in the original data. Together with the AUC values reported in Tables 5–8, this figure demonstrates that the separation in distance to criticality between healthy and diseased microbiomes is robust to changes in  $(r, p)$  and is not reproduced by simple reshuffling controls.

$r_{\text{target}}$	IBD	CRC	CDI	IBS
0.7	AUC = 1.000 (Yes)	AUC = 0.998 (Yes)	AUC = 1.000 (Yes)	AUC = 0.852 (Yes)
0.2	AUC = 0.998 (Yes)	AUC = 0.964 (Yes)	AUC = 1.000 (Yes)	AUC = 0.591 (No)
0.8	AUC = 1.000 (Yes)	AUC = 0.997 (Yes)	AUC = 1.000 (Yes)	AUC = 0.957 (Yes)

Table 5: Area under the ROC curve (AUC) for the comparison between healthy and pooled non-healthy samples, for different target species-samples ratios  $r_{\text{target}}$  (with  $p = 0.5$  fixed). “Yes” indicates successful separation, defined as  $\text{AUC} \geq 0.8$ . In all cases the corresponding Mann–Whitney  $p$ -values are  $p \ll 10^{-5}$ .

all  $r_{\text{target}}$ , with  $\text{AUC} \approx 1.0$  in every case. For IBS, the separation is again strong at  $r_{\text{target}} = 0.7$  and  $0.8$  ( $\text{AUC} \approx 0.99$  and  $0.98$ , respectively), but essentially lost at  $r_{\text{target}} = 0.2$  ( $\text{AUC} \approx 0.39$ ), consistent with the degradation observed for  $p = 0.5$  when  $r_{\text{target}}$  is very small.

The pairwise subgroup AUCs in Tables 10–12 further refine this picture. In IBD, healthy vs. CD and

Pair	$r_{\text{target}} = 0.7$	$r_{\text{target}} = 0.2$	$r_{\text{target}} = 0.8$
Healthy vs CD	0.999 (Yes)	0.999 (Yes)	1.000 (Yes)
Healthy vs UC	1.000 (Yes)	0.998 (Yes)	1.000 (Yes)
CD vs UC	0.838 (Yes)	0.734 (No)	0.634 (No)

Table 6: Pairwise AUCs between IBD subgroups for different target ratios  $r_{\text{target}}$  (with  $p = 0.5$ ). “Yes” indicates strong separation, defined as  $\max(\text{AUC}, 1 - \text{AUC}) \geq 0.8$ .

Pair	$r_{\text{target}} = 0.7$	$r_{\text{target}} = 0.2$	$r_{\text{target}} = 0.8$
Healthy vs Stage 0	0.994 (Yes)	0.919 (Yes)	0.990 (Yes)
Healthy vs Stage I-II	1.000 (Yes)	0.988 (Yes)	1.000 (Yes)
Healthy vs Stage III-IV	1.000 (Yes)	0.986 (Yes)	1.000 (Yes)
Stage 0 vs Stage I-II	0.530 (No)	0.577 (No)	0.595 (No)
Stage 0 vs Stage III-IV	0.762 (No)	0.638 (No)	0.818 (Yes)
Stage I-II vs Stage III-IV	0.812 (Yes)	0.581 (No)	0.835 (Yes)

Table 7: Pairwise AUCs between CRC subgroups for different target ratios  $r_{\text{target}}$  (with  $p = 0.5$ ). “Yes” indicates strong separation, defined as  $\max(\text{AUC}, 1 - \text{AUC}) \geq 0.8$ .

Pair	$r_{\text{target}} = 0.7$	$r_{\text{target}} = 0.2$	$r_{\text{target}} = 0.8$
Healthy vs IBS-C	0.966 (Yes)	0.525 (No)	0.995 (Yes)
Healthy vs IBS-D	0.739 (No)	0.658 (No)	0.919 (Yes)
IBS-C vs IBS-D	0.095 (Yes)	0.602 (No)	0.099 (Yes)

Table 8: Pairwise AUCs between IBS subgroups for different target ratios  $r_{\text{target}}$  (with  $p = 0.5$ ). “Yes” indicates strong separation, defined as  $\max(\text{AUC}, 1 - \text{AUC}) \geq 0.8$ . Note that AUC values far below 0.5 (e.g. 0.095) also correspond to strong separation but with the ordering of the groups reversed.

healthy vs. UC remain perfectly separated for all  $r_{\text{target}}$ , whereas the CD vs. UC contrast does not reach the separability threshold and is only moderate at best. In CRC, the healthy group is cleanly separated from all tumor stages for all  $r_{\text{target}}$ , while stage–stage comparisons involving Stage III–IV typically show strong separation, in line with the  $p = 0.5$  analysis, despite the limited effective sample size for individual stages. For IBS, both healthy vs. IBS-C and healthy vs. IBS-D display very strong separation at  $r_{\text{target}} = 0.7$  and 0.8, and the IBS-C vs. IBS-D comparison yields AUCs very close to zero in these settings, indicating a clear but reversed ordering of the scores between subtypes. By contrast, at  $r_{\text{target}} = 0.2$  all IBS contrasts fall in the non-separable range, reinforcing the conclusion that too aggressive a reduction in effective taxa ( $r$  too small) compromises the ability of our methodology to distinguish IBS groups.

These conclusions are visually supported by Fig. 6. As in the  $p = 0.5$  case, each row corresponds to a different  $r_{\text{target}}$  and each column to a disease cohort. For IBD, CRC and CDI, the healthy and diseased distributions  $\rho(\hat{g})$  in the main panels remain well separated across all  $r_{\text{target}}$ , consistent with the near-perfect AUCs in Table 9. In IBS, the separation is clear for  $r_{\text{target}} = 0.7$  and 0.8, while at  $r_{\text{target}} = 0.2$  the curves for healthy and pooled IBS groups strongly overlap, matching the poor AUC observed in that regime. In all cohorts, the reshuffled insets show markedly reduced or absent separation between groups, confirming that the observed differences in  $\hat{g}$  rely on the genuine correlation structure of the data rather than on marginal abundance distributions or sample size alone.

## 6.7 Negative-control analysis with pooled healthy cohorts

As a negative control, we pooled all healthy subjects from the two independent cohorts (Healthy 1 and Healthy 2 in 1) into a single abundance table. From this pooled dataset we then constructed two pseudo-cohorts, denoted “Healthy 1” and “Healthy 2”, by repeatedly drawing random subsamples of samples without replacement so that both groups contained the same number of individuals and were statistically equivalent by construction. For each pseudo-cohort, we applied exactly the same subsampling and DMFT-based estimation pipeline used in the main text: given a choice of  $(r, p)$  we drew  $M = 5 \times 10^3$  subsamples, computed the

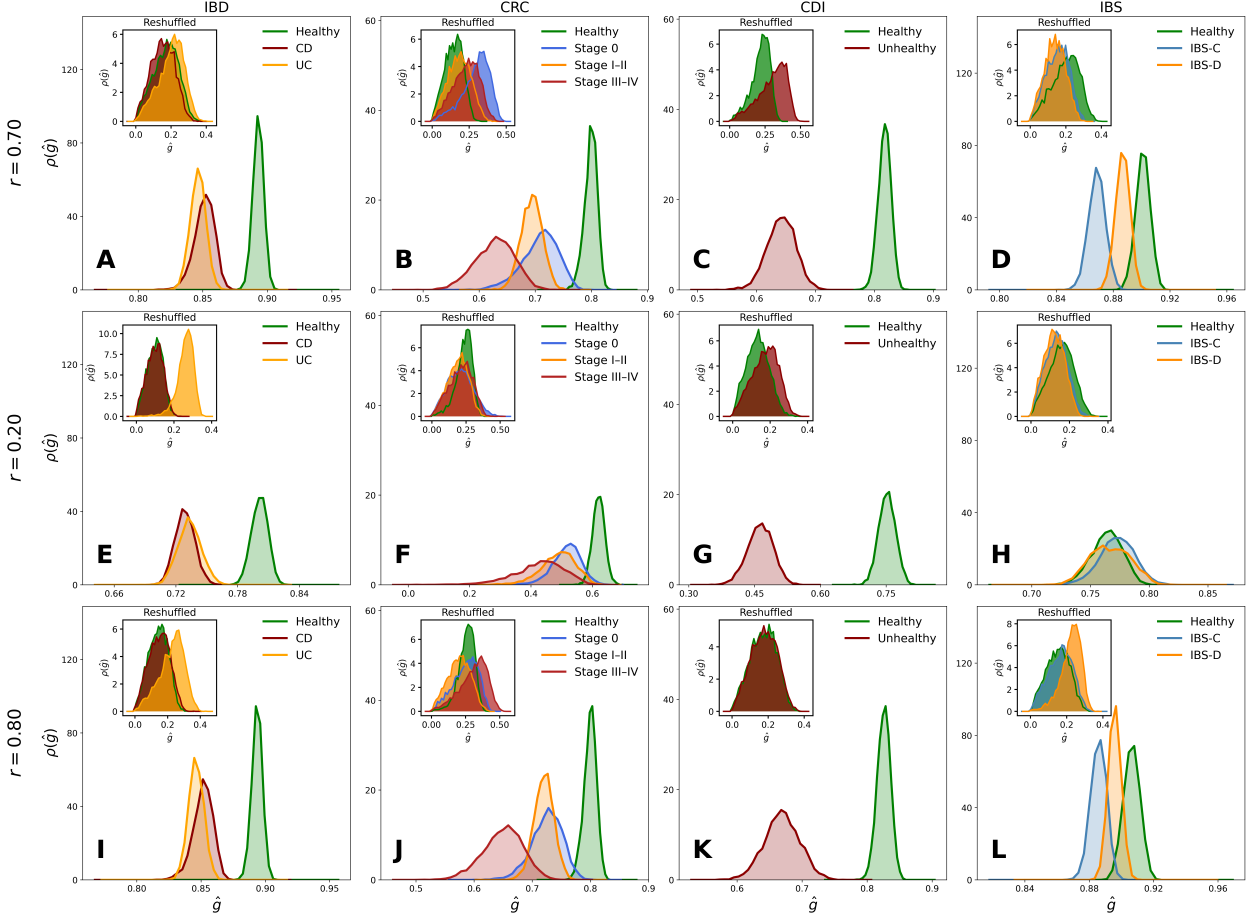


Figure 6: **Distributions of inferred distance to criticality for different disease cohorts at fixed subset fraction  $p = 0.7$  and varying target species-samples ratio  $r_{\text{target}} \in \{0.2, 0.7, 0.8\}$ .** Rows correspond to different values of  $r_{\text{target}}$ , and columns to IBD, CRC, CDI and IBS, respectively. Within each main panel, we show  $\rho(\hat{g})$  for healthy and diseased subgroups estimated from the original abundance tables, using the  $(r, p)$  subsampling scheme. Insets display the corresponding distributions obtained after reshuffling the abundance data (random permutation of entries), which largely collapses the group-specific curves and removes the strong separations observed in the original data. Together with the AUC values reported in Tables 9–12, this figure shows that the separation in distance to criticality between healthy and diseased microbiomes is robust for  $p = 0.7$  across a broad range of  $r_{\text{target}}$ , and is not reproduced by simple reshuffling controls.

$r_{\text{target}}$	IBD	CRC	CDI	IBS
0.7	AUC = 1.000 (Yes)	AUC = 1.000 (Yes)	AUC = 1.000 (Yes)	AUC = 0.989 (Yes)
0.2	AUC = 1.000 (Yes)	AUC = 0.992 (Yes)	AUC = 1.000 (Yes)	AUC = 0.392 (No)
0.8	AUC = 1.000 (Yes)	AUC = 0.999 (Yes)	AUC = 1.000 (Yes)	AUC = 0.975 (Yes)

Table 9: Area under the ROC curve (AUC) for the comparison between healthy and pooled non-healthy samples, for different target species-samples ratios  $r_{\text{target}}$  (with  $p = 0.7$  fixed). “Yes” indicates successful separation according to the same criterion used for  $p = 0.5$ . For IBS at  $r_{\text{target}} = 0.2$ , the separation is weak (AUC close to 0.5 and opposite ordering).

corresponding distance-to-criticality estimates  $\hat{g}$ , and then quantified the separation between the resulting  $\hat{g}$ -distributions via the AUC of the Mann–Whitney–Wilcoxon statistic.

Table 13 reports the AUC values obtained when comparing “Healthy 1” and “Healthy 2” for a grid

Pair	$r_{\text{target}} = 0.7$	$r_{\text{target}} = 0.2$	$r_{\text{target}} = 0.8$
Healthy vs CD	1.000 (Yes)	1.000 (Yes)	1.000 (Yes)
Healthy vs UC	1.000 (Yes)	1.000 (Yes)	1.000 (Yes)
CD vs UC	0.711 (No)	0.374 (No)	0.721 (No)

Table 10: Pairwise AUCs between IBD subgroups for  $p = 0.7$  and different target ratios  $r_{\text{target}}$ . “Yes” indicates strong separation according to the same criterion as in Table 6.

Pair	$r_{\text{target}} = 0.7$	$r_{\text{target}} = 0.2$	$r_{\text{target}} = 0.8$
Healthy vs Stage 0	0.999 (Yes)	0.984 (Yes)	0.998 (Yes)
Healthy vs Stage I-II	1.000 (Yes)	0.993 (Yes)	1.000 (Yes)
Healthy vs Stage III-IV	1.000 (Yes)	0.998 (Yes)	1.000 (Yes)
Stage 0 vs Stage I-II	0.692 (No)	0.647 (No)	0.594 (No)
Stage 0 vs Stage III-IV	0.953 (Yes)	0.825 (Yes)	0.960 (Yes)
Stage I-II vs Stage III-IV	0.954 (Yes)	0.720 (No)	0.972 (Yes)

Table 11: Pairwise AUCs between CRC subgroups for  $p = 0.7$  and different target ratios  $r_{\text{target}}$ . As before, “Yes” indicates strong separation. Note that stage–stage separations are most robust for comparisons involving Stage III–IV.

Pair	$r_{\text{target}} = 0.7$	$r_{\text{target}} = 0.2$	$r_{\text{target}} = 0.8$
Healthy vs IBS-C	1.000 (Yes)	0.329 (No)	0.999 (Yes)
Healthy vs IBS-D	0.979 (Yes)	0.454 (No)	0.952 (Yes)
IBS-C vs IBS-D	0.009 (Yes)	0.606 (No)	0.050 (Yes)

Table 12: Pairwise AUCs between IBS subgroups for  $p = 0.7$  and different target ratios  $r_{\text{target}}$ . AUC values far below 0.5 (e.g. 0.009 or 0.050) indicate strong separation with reversed ordering of the scores.

of species–samples ratios  $r \in \{0.4, 0.6, 0.8\}$  and subset fractions  $p \in \{0.1, 0.3, 0.5\}$ . Across all parameter combinations, the AUC remains in the range  $\text{AUC} \approx 0.60\text{--}0.73$ . According to the separability criterion used in this work, none of these comparisons qualify as strongly separable: the two pseudo-cohorts are only mildly shifted relative to each other, as expected when splitting a single homogeneous healthy population into two arbitrary halves. The associated  $p$ -values are extremely small due to the very large number of subsamples ( $M = 5000$ ), but the effect sizes (AUC values close to 0.5) are modest.

$r$	$p$	$\langle r_{\text{eff}} \rangle$	AUC( $H_1$ vs $H_2$ )	$p$ -value	Separable?
0.40	0.10	0.400	0.660	$2.2 \times 10^{-168}$	No
0.40	0.30	0.397	0.700	$1.4 \times 10^{-262}$	No
0.40	0.50	0.398	0.689	$6.2 \times 10^{-234}$	No
0.60	0.10	0.600	0.725	$< 10^{-300}$	No
0.60	0.30	0.598	0.688	$2.9 \times 10^{-233}$	No
0.60	0.50	0.599	0.669	$4.8 \times 10^{-189}$	No
0.80	0.10	0.800	0.704	$1.1 \times 10^{-273}$	No
0.80	0.30	0.799	0.673	$6.3 \times 10^{-197}$	No
0.80	0.50	0.799	0.606	$6.4 \times 10^{-75}$	No

Table 13: Negative-control test for the distance-to-criticality estimator using pooled healthy cohorts. We first pooled all healthy samples from the two independent control datasets into a single abundance matrix, and then constructed two disjoint pseudo-cohorts  $H_1$  and  $H_2$  by randomly splitting the columns of said abundance table into two equally sized subsets. For each choice of  $(r, p)$  we then ran the same subsampling pipeline used in Figure 5 of the main text on  $H_1$  and  $H_2$ , obtaining distributions of  $\hat{g}$  and computing the AUC for the contrast  $H_1$  vs.  $H_2$ . The column  $\langle r_{\text{eff}} \rangle$  reports the mean effective species–samples ratio over subsamples, and “Separable?” follows the same criterion used elsewhere in the manuscript,  $\max(\text{AUC}, 1 - \text{AUC}) \geq 0.8$ .

Figure 7 provides a visual representation of the numerical results shown in Table 13. For each combination of species–samples ratio  $r \in \{0.4, 0.6, 0.8\}$  and subset fraction  $p \in \{0.1, 0.3, 0.5\}$ , the main panels display the empirical distributions  $\rho(\hat{g})$  obtained for the two pseudo-cohorts “Healthy 1” and “Healthy 2” constructed by randomly splitting the pooled healthy dataset. Across all  $(r, p)$  pairs, the two curves largely overlap, with only modest shifts in their central tendency and shape, consistent with the moderate AUC values ( $AUC \approx 0.60\text{--}0.73$ ) reported in Table 13. In particular, none of the panels shows the kind of pronounced, systematic displacement between distributions that we observe when comparing healthy and diseased groups in the main text.

The insets show the same analysis applied to reshuffled versions of the data, where the entries of the abundance table are randomly permuted so as to destroy the empirical correlation structure while preserving marginal distributions. In this null model, the  $\rho(\hat{g})$  curves for “Healthy 1” and “Healthy 2” almost perfectly collapse for all  $(r, p)$ , indicating that any residual differences seen in the main panels arise from finite-sample fluctuations rather than systematic biases in the estimator or the subsampling scheme. Taken together, Table 13 and Figure 7 confirm that our pipeline does not spuriously produce strong between-group separations when comparing two statistically equivalent healthy cohorts, and therefore has a low propensity for false positives.

## References

- [1] Crispin Gardiner. *Stochastic Methods: A Handbook for the Natural and Social Sciences*. Springer, 2009.
- [2] Rubén Calvo, Carles Martorell, Adrián Roig, and Miguel A Muñoz. Robust scaling in human brain dynamics despite latent variables and limited sampling distortions. *arXiv preprint arXiv:2506.03640*, 2025.
- [3] Terence Tao, Van Vu, and Manjunath Krishnapur. Random Matrices: Universality of ESDs and the Circular Law. *Annals of Probability*, 38(5):2023–2065, 2010.
- [4] Stefano Allesina and Si Tang. Stability criteria for complex ecosystems. *Nature*, 483(7388):205–208, 2012.
- [5] David Dahmen, Sonja Grün, Markus Diesmann, and Moritz Helias. Second type of criticality in the brain uncovers rich multiple-neuron dynamics. *Proceedings of the National Academy of Sciences*, 116(26):13051–13060, June 2019. Number: 26.
- [6] G. E. Uhlenbeck and L. S. Ornstein. On the Theory of the Brownian Motion. *Physical Review*, 36(5):823–841, 1930.
- [7] Moritz Helias and David Dahmen. *Statistical Field Theory for Neural Networks*, volume 970 of *Lecture Notes in Physics*. Springer International Publishing, Cham, 2020.
- [8] Robert M May. Simple mathematical models with very complicated dynamics. *Nature*, 261:459–467, 1976.
- [9] Ottar N. Bjørnstad. Nonlinearity and chaos in ecological dynamics revisited. *Proceedings of the National Academy of Sciences*, 112(20):6252–6253, May 2015.
- [10] R. F. Costantino, J. M. Cushing, Brian Dennis, and Robert A. Desharnais. Experimentally induced transitions in the dynamic behaviour of insect populations. *Nature*, 375(6528):227–230, May 1995.
- [11] R. F. Costantino, R. A. Desharnais, J. M. Cushing, and Brian Dennis. Chaotic Dynamics in an Insect Population. *Science*, 275(5298):389–391, January 1997.
- [12] Elisa Benincà, Bill Ballantine, Stephen P. Ellner, and Jef Huisman. Species fluctuations sustained by a cyclic succession at the edge of chaos. *Proceedings of the National Academy of Sciences*, 112(20):6389–6394, May 2015.

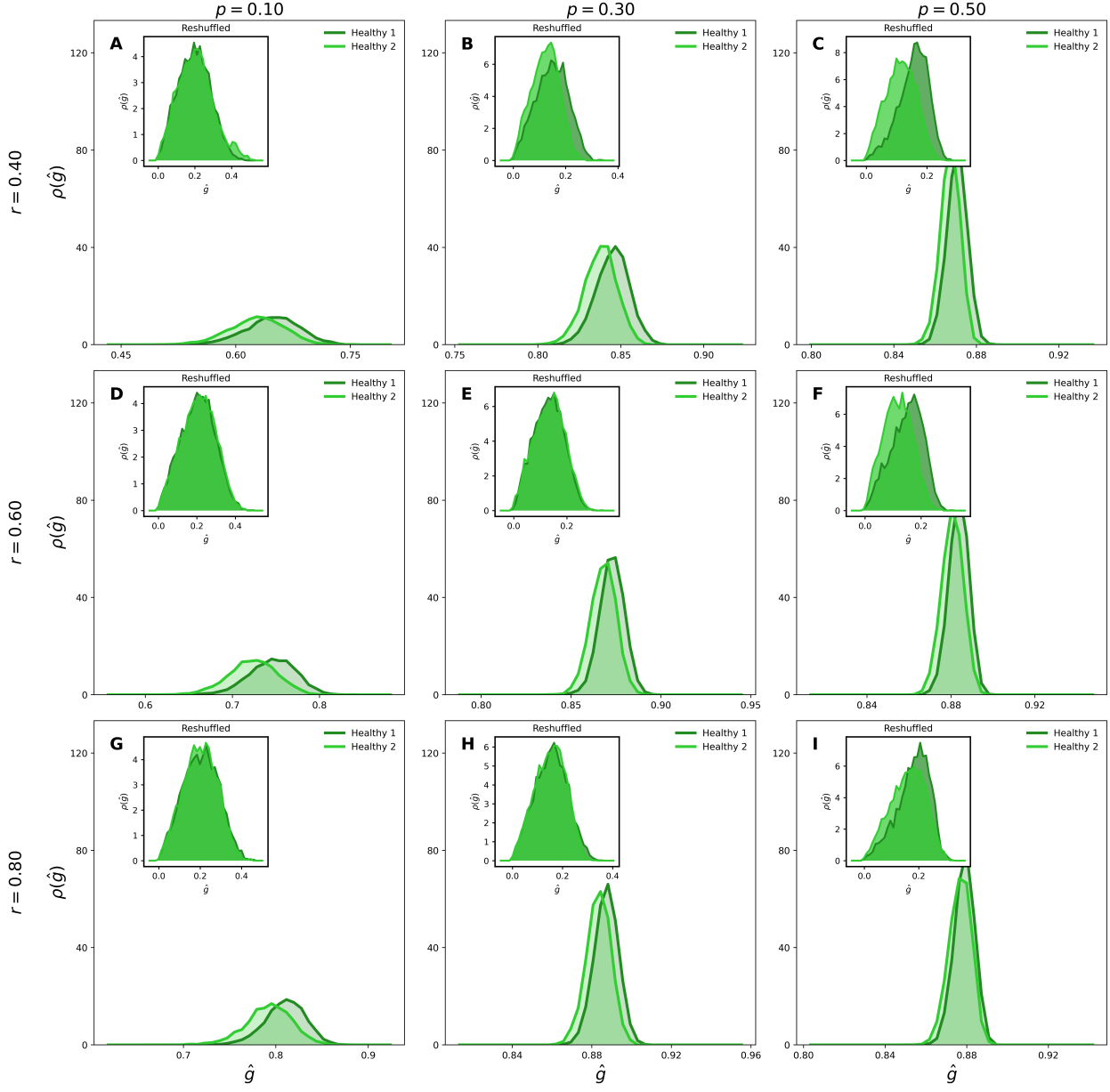


Figure 7: **Negative-control comparison between two pseudo-cohorts of healthy subjects.** All healthy samples from the two independent healthy cohorts are pooled into a single dataset and then randomly split into two pseudo-cohorts, denoted “Healthy 1” and “Healthy 2”, of equal size. For each combination of species-samples ratio  $r \in \{0.4, 0.6, 0.8\}$  (rows) and subset fraction  $p \in \{0.1, 0.3, 0.5\}$  (columns), we draw  $M = 5 \times 10^3$  subsamples using the  $(r, p)$  scheme and compute the corresponding distance-to-criticality estimates  $\hat{g}$ . The main panels show the empirical distributions  $\rho(\hat{g})$  for “Healthy 1” and “Healthy 2”; in all cases, the two curves overlap strongly and exhibit only mild shifts, in agreement with the moderate AUC values reported in Table 13. Insets display the same analysis applied to reshuffled abundance tables, in which the entries are randomly permuted within each taxon. In this null model, the two distributions collapse almost perfectly for all  $(r, p)$ , indicating that our estimator and subsampling pipeline do not spuriously generate strong separations when comparing two statistically equivalent healthy cohorts.

[13] Tanya L Rogers, Bethany J Johnson, and Stephan B Munch. Chaos is not rare in natural ecosystems. *Nature ecology & evolution*, 6(8):1105–1111, 2022.

[14] Thibaut Arnoux de Pirey and Guy Bunin. Many-species ecological fluctuations as a jump process from the brink of extinction. *Physical Review X*, 14(1):011037, 2024.

[15] Felix Roy, Matthieu Barbier, Giulio Biroli, and Guy Bunin. Complex interactions can create persistent fluctuations in high-diversity ecosystems. *PLOS Computational Biology*, 16(5):e1007827, May 2020.

[16] Emil Mallmin, Arne Traulsen, and Silvia De Monte. Chaotic turnover of rare and abundant species in a strongly interacting model community. *Proceedings of the National Academy of Sciences*, 121(11):e2312822121, March 2024.

[17] Emmy Blumenthal, Jason W. Rocks, and Pankaj Mehta. Phase Transition to Chaos in Complex Ecosystems with Nonreciprocal Species-Resource Interactions. *Physical Review Letters*, 132(12):127401, March 2024.

[18] Jacopo Grilli. Macroecological laws describe variation and diversity in microbial communities. *Nature Comm.*, 11(1):1–11, 2020.

[19] Miguel A Munoz. Nature of different types of absorbing states. *Physical Review E*, 57(2):1377, 1998.

[20] Ivan Dornic, Hugues Chaté, and Miguel A Munoz. Integration of langevin equations with multiplicative noise and the viability of field theories for absorbing phase transitions. *Physical review letters*, 94(10):100601, 2005.

[21] Aditya Mahadevan, Michael T Pearce, and Daniel S Fisher. Spatiotemporal ecological chaos enables gradual evolutionary diversification without niches or tradeoffs. *Elife*, 12:e82734, 2023.

[22] J. P. Eckmann and D. Ruelle. Ergodic theory of chaos and strange attractors. *Reviews of Modern Physics*, 57(3):617–656, July 1985.

[23] Giancarlo Benettin, Luigi Galgani, Antonio Giorgilli, and Jean-Marie Strelcyn. Lyapunov Characteristic Exponents for smooth dynamical systems and for hamiltonian systems; A method for computing all of them. Part 2: Numerical application. *Meccanica*, 15(1):21–30, March 1980.

[24] Arkadij Pikovskij and A. Politi. *Lyapunov exponents: a tool to explore complex dynamics*. Cambridge University Press, Cambridge, 2016.

[25] Jianhai Bao, Xuerong Mao, Geroge Yin, and Chenggui Yuan. Competitive Lotka–Volterra population dynamics with jumps. *Nonlinear Analysis: Theory, Methods & Applications*, 74(17):6601–6616, December 2011.

[26] A. Fiasconaro, D. Valenti, and B. Spagnolo. Noise in ecosystems: A short review. *Mathematical Biosciences and Engineering*, 1(1):185–211, March 2004.

[27] Jannis Schuecker, Sven Goedeke, and Moritz Helias. Optimal Sequence Memory in Driven Random Networks. *Physical Review X*, 8(4):041029, November 2018.

[28] István Scheuring and Gábor Domokos. Only noise can induce chaos in discrete populations. *Oikos*, 116(3):361–366, March 2007.

[29] Bernat Bassols-Cornudella and Jeroen S. W. Lamb. Noise-induced chaos: A conditioned random dynamics perspective. *Chaos: An Interdisciplinary Journal of Nonlinear Science*, 33(12):121102, December 2023.

[30] Ludwig Arnold. *Random Dynamical Systems*. Springer Monographs in Mathematics. Springer Berlin Heidelberg, Berlin, Heidelberg, 1998.

[31] Guillaume Lajoie, Kevin K. Lin, and Eric Shea-Brown. Chaos and reliability in balanced spiking networks with temporal drive. *Physical Review E*, 87(5):052901, May 2013.

[32] Jason Lloyd-Price, Cesar Arze, Ashwin N. Ananthakrishnan, Melanie Schirmer, Julian Avila-Pacheco, Tiffany W. Poon, Elizabeth Andrews, Nadim J. Ajami, Kevin S. Bonham, Colin J. Brislawn, David Casero, Holly Courtney, Antonio Gonzalez, Thomas G. Graeber, A. Brantley Hall, Kathleen Lake, Carol J. Landers, Himel Mallick, Damian R. Plichta, Mahadev Prasad, Gholamali Rahnavard, Jenny Sauk, Dmitry Shungin, Yoshiki Vázquez-Baeza, Richard A. White, Jonathan Braun, Lee A. Denson, Janet K. Jansson, Rob Knight, Subra Kugathasan, Dermot P. B. McGovern, Joseph F. Petrosino, Thaddeus S. Stappenbeck, Harland S. Winter, Clary B. Clish, Eric A. Franzosa, Hera Vlamakis, Ramnik J. Xavier, and Curtis Huttenhower. Multi-omics of the gut microbial ecosystem in inflammatory bowel diseases. *Nature*, 569(7758):655–662, May 2019.

[33] Ruben A.T. Mars, Yi Yang, Tonya Ward, Mo Houtti, Sambhawa Priya, Heather R. Lekatz, Xiaojia Tang, Zhifu Sun, Krishna R. Kalari, Tal Korem, Yogesh Bhattarai, Tenghao Zheng, Noam Bar, Gary Frost, Abigail J. Johnson, Will van Treuren, Shuo Han, Tamas Ordog, Madhusudan Grover, Justin Sonnenburg, Mauro D’Amato, Michael Camilleri, Eran Elinav, Eran Segal, Ran Blekhman, Gianrico Farrugia, Jonathan R. Swann, Dan Knights, and Purna C. Kashyap. Longitudinal multi-omics reveals subset-specific mechanisms underlying irritable bowel syndrome. *Cell*, 182(6):1460–1473.e17, September 2020.

[34] Pamela Ferretti, Jakob Wirbel, Oleksandr M Maistrenko, Thea Van Rossum, Renato Alves, Anthony Fullam, Wasiu Akanni, Christian Schudoma, Anna Schwarz, Roman Thielemann, Leonie Thomas, Stefanie Kandels, Rajna Hercog, Anja Telzerow, Ivica Letunic, Michael Kuhn, Georg Zeller, Thomas SB Schmidt, and Peer Bork. *C. difficile* may be overdiagnosed in adults and is a prevalent commensal in infants. *eLife*, September 2023.

[35] Shinichi Yachida, Sayaka Mizutani, Hirotsugu Shiroma, Satoshi Shiba, Takeshi Nakajima, Taku Sakamoto, Hikaru Watanabe, Keigo Masuda, Yuichiro Nishimoto, Masaru Kubo, Fumie Hosoda, Hirofumi Rokutan, Minoru Matsumoto, Hiroyuki Takamaru, Masayoshi Yamada, Takahisa Matsuda, Motoki Iwasaki, Taiki Yamaji, Tatsuo Yachida, Tomoyoshi Soga, Ken Kurokawa, Atsushi Toyoda, Yoshitoshi Ogura, Tetsuya Hayashi, Masanori Hatakeyama, Hitoshi Nakagama, Yutaka Saito, Shinji Fukuda, Tatsuhiko Shibata, and Takuji Yamada. Metagenomic and metabolomic analyses reveal distinct stage-specific phenotypes of the gut microbiota in colorectal cancer. *Nature Medicine*, 25(6):968–976, June 2019.

[36] Jonguk Park, Kumiko Kato, Haruka Murakami, Koji Hosomi, Kumpei Tanisawa, Takashi Nakagata, Harumi Ohno, Kana Konishi, Hitoshi Kawashima, Yi-An Chen, Attayeb Mohsen, Jin-zhong Xiao, Toshitaka Odamaki, Jun Kunisawa, Kenji Mizuguchi, and Motohiko Miyachi. Comprehensive analysis of gut microbiota of a healthy population and covariates affecting microbial variation in two large Japanese cohorts. *BMC Microbiology*, 21(1), May 2021.

[37] Henry B. Mann and Donald R. Whitney. On a test of whether one of two random variables is stochastically larger than the other. *Annals of Mathematical Statistics*, 18(1):50–60, 1947.

[38] James A. Hanley and Barbara J. McNeil. The meaning and use of the area under a receiver operating characteristic (roc) curve. *Radiology*, 143(1):29–36, 1982.

[39] Tom Fawcett. An introduction to ROC analysis. *Pattern Recognition Letters*, 27(8):861–874, 2006.